



Article

<https://doi.org/10.1038/s44220-025-00560-x>

Multi-organ AI endophenotypes chart the heterogeneity of brain, eye and heart pan-disease

Received: 24 February 2025

Accepted: 5 November 2025

Published online: 06 January 2026

Check for updates

The MULTI Consortium*, Aleix Boquet-Pujadas ^{1,14}, Filippos Anagnostakis ^{1,14}, Zhijian Yang ², Ye Ella Tian ³, Michael R. Duggan ⁴, Guray Erus ⁵, Dhivya Srinivasan ⁵, Cassandra M. Joynes ⁴, Wenjia Bai ⁶, Praveen J. Patel ⁷, Keenan A. Walker ⁴, Andrew Zalesky ³, Christos Davatzikos ⁵ & Junhao Wen ^{1,8,9,10}

Disease heterogeneity and commonality pose critical challenges to precision medicine, as traditional approaches frequently focus on single disease entities and overlook shared mechanisms across conditions. Here, inspired by pan-cancer and multi-organ research, we introduce the concept of 'pan-disease' to investigate the heterogeneity and shared etiology in brain, eye and heart diseases. Leveraging individual-level data from 129,340 participants and summary-level data, curated from the MULTI consortium, we applied a weakly supervised deep learning model (Surreal-GAN) to multi-organ imaging, genetic and proteomic data, identifying 11 artificial intelligence (AI)-derived biomarkers, called multi-organ AI endophenotypes, for the brain (Brain 1–6), eye (Eye 1–3) and heart (Heart 1–2). We found Brain 3 to be a risk factor for Alzheimer's disease progression and mortality, whereas Brain 5 was protective against Alzheimer's disease progression. In data from an anti-amyloid Alzheimer's disease drug (solanezumab), heterogeneity in cognitive decline trajectories was observed across treatment groups. At week 240, patients with lower Brain 1–3 expression had slower cognitive decline, whereas patients with higher expression had faster cognitive decline. A multilayer causal pathway pinpointed Brain 1 as a mediational endophenotype linking the FLRT2 protein to migraine, exemplifying new therapeutic targets and pathways. In addition, genes associated with Eye 1 and Eye 3 were enriched in cancer drug-related gene sets with causal links to specific cancer types and proteins. Finally, Heart 1 and Heart 2 had the highest mortality risk and unique medication history profiles, with Heart 1 showing favorable responses to antihypertensive medications and Heart 2 to digoxin treatment. The 11 multi-organ AI endophenotypes provide new AI dimensional representations for precision medicine and highlight the potential of AI-driven patient stratification for disease risk monitoring, clinical trials and drug discovery.

A full list of affiliations appears at the end of the paper. e-mail: junhao.wen89@gmail.com

Disease heterogeneity within single disease entities, cross-disease commonalities and etiologic overlap present critical challenges for precision medicine¹. In the case of single disease entities, artificial intelligence (AI) has been applied to brain magnetic resonance imaging (MRI) data, which revealed distinct disease subtypes or dimensions, highlighting the neuroanatomical heterogeneity of brain disorders, such as Alzheimer's disease (AD)^{2,3}. Also, recent findings from genetics and transcriptomics have unraveled overlapping molecular and neuropathological signatures across brain disorders, highlighting their shared biological underpinnings^{4,5}. We argue that AI holds great potential to jointly model human aging and disease concurrently from the two abovementioned perspectives to advance precision medicine.

Addressing disease heterogeneity and transcending traditional classifications, such as those based on International Classification of Diseases (ICD) codes, may reveal new insights into aging and disease. Recent initiatives have focused on identifying transdiagnostic disease subtypes and dimensions, particularly within brain disorders such as psychiatric (depression and psychosis⁶) and developmental conditions⁷. This has provided new avenues for understanding polygenic and etiologically multifaceted diseases. In our recent study, by leveraging a weakly supervised learning framework⁸ (for example, Surreal-GAN^{9,10}), we derived nine AI-derived endophenotypes to capture the within-disease heterogeneity and cross-disease similarities in four brain diseases¹¹, including autism spectrum disorder, schizophrenia, late-life depression and AD, and aging¹⁰. Critically, the nine AI-derived phenotypes were generated within a specific disease entity, such as AD. The observed neuroanatomical overlap underscores the need for new approaches that derive disease subtypes or dimensions that transcend traditional disease boundaries, enabling a more integrated understanding of disease mechanisms.

Modeling human aging and disease necessitates a comprehensive, multiscale approach spanning both spatial and temporal granularities¹². Recent advances in multi-organ research^{13–18} have opened up new possibilities for holistic modeling of human aging and disease. For example, a study¹⁹ used machine learning to calculate the biological age gap (BAG) in nine organ systems, linking these biomarkers to lifestyle and mortality in the UK Biobank (UKBB). Subsequent analyses^{17,20} further investigated the genetic architecture of these multi-organ BAGs. Similarly, multi-omics approaches, such as combining brain MRI data with genetics and proteomics, offer enhanced diagnostic precision and granularity. For instance, recent studies^{2,21} showed that incorporating genetic data into imaging-based models (for example, Gene-SGAN²¹) enhances disease subtyping accuracy and outperforms approaches developed solely on imaging data (for example, Smile-GAN⁷). In another study¹⁶, we established the brain–heart–eye axis using imaging-derived phenotypes (IDPs) from *in vivo* imaging, genetic and proteomic data of these three organs, showing that no organ system is an island²². Taken together, this evidence underscores the importance of integrating multi-organ, multi-omics data across multiple human organ systems and omics data types to model disease heterogeneity.

Dissecting disease heterogeneity and commonality using AI in combination with *in vivo* imaging techniques (for example, MRI for the brain²³ and heart²⁴, and optical coherence tomography (OCT)^{25–27} for the eye) also aligns with the endophenotype hypothesis²⁸. Originally proposed in psychiatric genetics, this hypothesis suggests that intermediate phenotypes—such as those identified through imaging—bridge the causal pathway from genetic variants to disease endpoints (DEs) and clinical symptoms. Two potential models of endophenotypes have been proposed: (1) the liability-index model, wherein genetics simultaneously influences both DEs and endophenotypes (that is, horizontal pleiotropy); and (2) the mediational model, in which genetic effects on DEs are (exclusively) mediated through intermediate phenotypes (that is, vertical pleiotropy). While the former phenomenon is ubiquitous in population genetics, the latter holds potential for identifying causal and actionable target genes for therapeutic development

and intervention. In previous work²⁹, we showed that AI-derived subtypes of schizophrenia showed lower polygenicity and weaker negative purifying selection compared with traditional case–control diagnoses of schizophrenia, providing proof-of-concept evidence to support one assumption of this hypothesis. That is, the endophenotype is less polygenic than the DE itself, thereby being closer to the underlying genetic etiology of the disease²⁸.

Here we introduced six, three and two multi-organ AI endophenotypes (MAEs) to digitize individual-level morphological heterogeneity in brain, eye and heart diseases to address the outlined challenges. Intuitively, each organ-specific MAE captures a distinctive imaging pattern, reflecting diverse disease spectrums within each organ system. This was achieved by applying three separate Surreal-GAN^{9,10} models to organ-specific imaging data of the brain, eye and heart consolidated via the ongoing MULTI consortium (see 'The MULTI consortium' in Methods and Supplementary Table 1). Subsequently, we linked the 11 MAEs to other omic data, including genetics and proteomics data, both at individual and summary levels. The scientific advancements are threefold. First, drawing inspiration from pan-cancer research³⁰, which explores shared mechanisms across different cancer types, we introduce the concept of 'pan-disease' to address the complexity of disease heterogeneity and commonalities across conditions or diseases in each organ. Second, recognizing that no organ system functions in isolation²², we leverage large-scale, multi-organ and multi-omics biomedical data to capture the morphological heterogeneity of the pan-disease of the three organs. Third, we present putative evidence to support the endophenotype hypothesis²⁸. In particular, we show how the mediational model of the endophenotype hypothesis can be validated in certain cases, offering new insights that could inform drug discovery and personalized therapeutic strategies.

We present the definition of pan-disease, our analytic approaches, the network architecture of Surreal-GAN, the datasets used and the selection of the optimal number of MAEs (k) in Fig. 1. Our analytic workflow is the following: We first derived the 11 MAEs ('Multi-organ imaging features used to derive the MAEs via Surreal-GAN' in Methods) via Surreal-GAN^{9,10} ('Surreal-GAN methodological considerations' in Methods) using specific imaging features from each organ, and evaluated the expression of the identified imaging patterns in test datasets from the same study and other independent studies. We then performed a phenoome-wide association study (PWAS; 'Phenotypic analysis' in Methods) to establish cross-organ phenotypic landscapes between the 11 MAEs and other clinical traits. A proteome-wide association study (ProWAS; 'Proteomic analyses' in Methods) was conducted to link the 11 MAEs to 2,923 plasma proteins (Olink) from UKBB and generate their expression profiles using organ- and/or tissue-specific RNA-seq and protein data³¹. We conducted genome-wide association studies (GWAS) to link the 11 MAEs with common single-nucleotide polymorphisms (SNPs). Subsequently, we performed several post-GWAS analyses to partially validate the genetic signals, such as genetic correlation and Mendelian randomization ('Genetic analyses' in Methods). Lastly, we evaluated the clinical relevance of the 11 MAEs in a set of prediction tasks, including mortality, AD progression, incidence of DEs, medication status and preclinical AD drug (that is, solanezumab) outcome ('Prediction and association analyses for the risk of DEs, AD progression, mortality, history of medication use and preclinical AD drug effects' in Methods). All the results and code, including the GWAS summary statistics, are publicly accessible through the MEDICINE knowledge portal: <https://labs-laboratory.com/medicine/>.

Results

Reproducible imaging patterns of the 11 MAEs of pan-disease in the brain, eye and heart

By applying multi-organ imaging features ('Multi-organ imaging features used to derive the MAEs via Surreal-GAN' in Methods) to the methodologically enhanced Surreal-GAN model in the UKBB training set

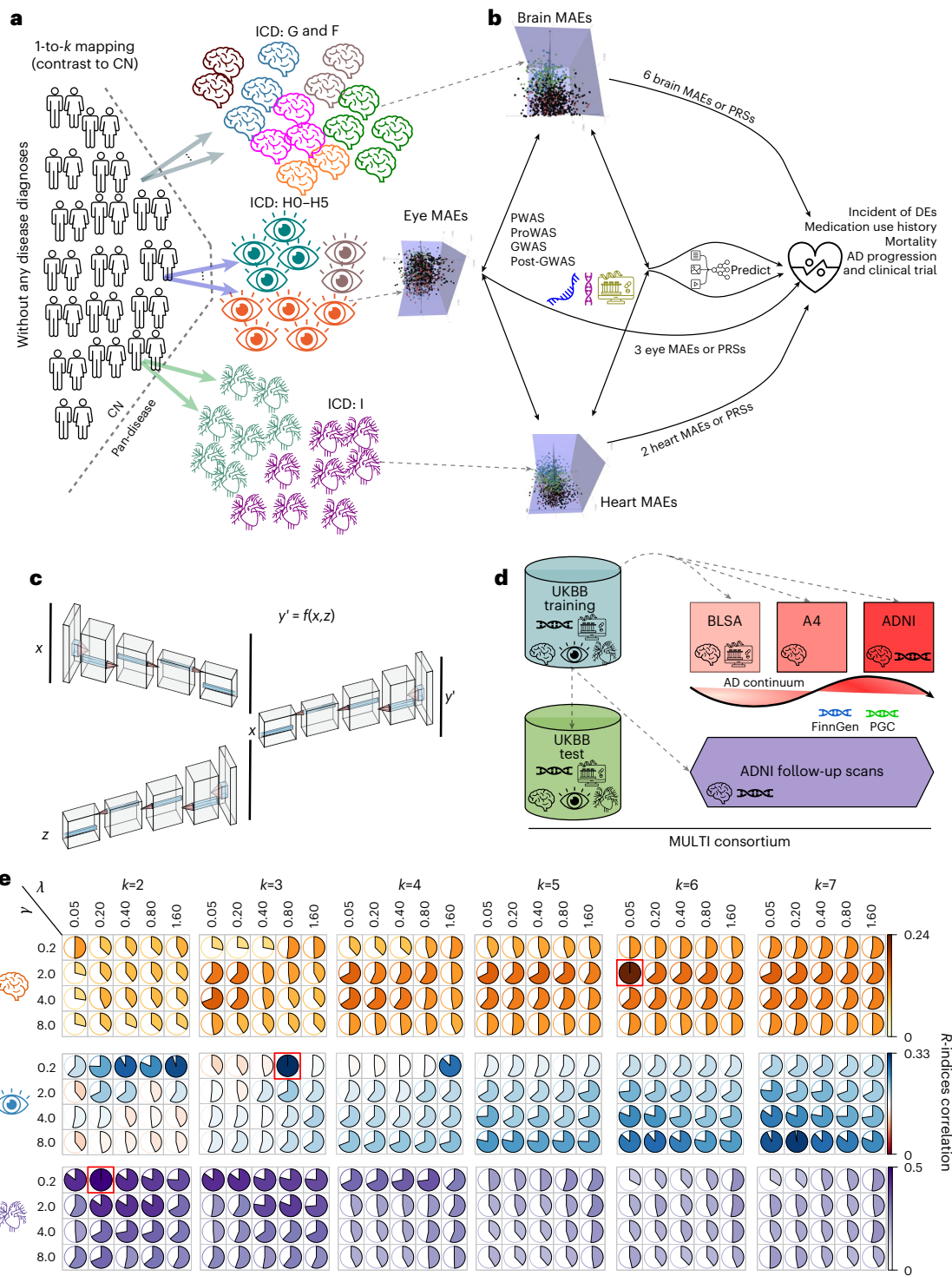


Fig. 1 | Schematic diagram of the definition of pan-disease, method of analysis, network architecture underlying Surreal-GAN, datasets and model selection procedure. **a**, Using a weakly supervised representation deep model called Surreal-GAN, we introduce an approach to conceptualizing pan-disease in the brain, eye and heart. In this framework, the reference domain consists of a healthy control (CN) population, and the target domain consists of a pan-disease patient population. Surreal-GAN, separately applied to the brain, eye and heart pan-disease populations, seeks a 1-to- k mapping to model distinct disease dimensions identified as MAEs. CN participants are defined as those with no diagnosed diseases across multiple sources in the UKBB, while the pan-disease group for each organ includes patients with any organ-specific disease identified using ICD-10 codes. **b**, The 11 MAEs for the brain, eye and heart served as phenotypes for an extensive array of downstream analyses, including PWAS, ProWAS, GWAS, post-GWAS and prediction modeling tasks. **c**, The network

architecture for the key mapping function of the Surreal-GAN model. It learns a function f , which maps the CN data x to synthesized pan-disease data $y' = f(x, z)$, where z is the latent variable indicating the transformation directions. **d**, Using data from the MULTI consortium, we trained Surreal-GAN on UKBB training data and then applied it to UKBB test data, and independent datasets representing the AD continuum. These included BLSA for aging, A4 for preclinical AD, ADNI for MCI and AD stages, longitudinal follow-up brain MRI from ADNI, and GWAS summary data from FinnGen and PGC. **e**, We performed a grid search to select three optimal parameters (k , λ and γ). The reproducibility index (R -index correlation) was used to select the three models. The red rectangle for each organ obtained the highest R -index correlation and was chosen for the optimal model in the subsequent analyses. The color and the size of the pie reflect the effect size of the R -index correlation.

(Fig. 1 and Supplementary Table 1), we derived 11 MAEs of pan-disease: 6 for the brain (Brain 1–6), 3 for the eye (Eye 1–3) and 2 for the heart (Heart 1–2). Refer to ‘Surreal-GAN methodological considerations’ in Methods and Fig. 1 for defining the healthy controls (participants without any disease diagnosis from various resources (CN)) and pan-disease patients (patients with any ICD-based disease diagnosis from each organ system (PT)). We performed a grid search to choose three hyperparameters to define the optimal number of dimensions (k) in each organ pan-disease (Fig. 1e).

In the case–control (CN–PT) setting, pan-disease of the brain showed brain atrophy in the frontal, temporal and occipital lobes (Fig. 2a). Brain 1 showed a pattern of global atrophy, characterized by pronounced volume loss in the temporal lobe and inferior cerebellum (for example, https://labs-laboratory.com/bridgeport/music/C128_9), accompanied by a concomitant enlarged brain volume in the superior cerebellum. Brain 2 showed brain atrophy in the parietal lobe and enlarged brain volume in the frontal lobe (for example, https://labs-laboratory.com/bridgeport/music/C128_84). Brain 3 showed global atrophy over the entire brain (for example, https://labs-laboratory.com/bridgeport/music/C128_31) and enlarged brain volume in the cerebellum. Brain 4 showed enlarged brain volume, mainly in the frontal and occipital lobes (for example, https://labs-laboratory.com/bridgeport/music/C128_13), but without affecting the temporal poles and deep subcortical structures. Brain 5 showed enlarged brain volume in the frontal and temporal lobes (for example, https://labs-laboratory.com/bridgeport/music/C128_10). Brain 6 showed frontal lobe atrophy and enlarged brain volume in deep subcortical structures (for example, https://labs-laboratory.com/bridgeport/music/C128_1). Both similarities and differences were observed across the six brain MAEs, echoing the underlying modeling considerations of Surreal-GAN (‘Methodological advances in Surreal-GAN’ in Methods). For example, Brains 1, 2 and 3 showed a common feature of atrophy in deep subcortical structures (C128_1, indicating the first structural network derived from our data-driven non-negative matrix factorization method, where C represents the scale or dimensionality of the brain parcellation). In contrast, Brain 6 showed a distinct pattern characterized by increased volume (Fig. 2a). These imaging patterns manifested in the UKBB test dataset (Supplementary Figs. 1a and 2). Previous studies have primarily highlighted disease heterogeneity in brain disorders within individual conditions, such as AD³², late-life depression³³ and schizophrenia^{34,35}, and across transdiagnostic phenotypes⁶. The imaging patterns from these previous studies offer data-driven evidence supporting neuro-anatomical similarities across these disease entities.

The CN–PT analyses showed global retinal morphological thinning for pan-disease of the eye. For the three eye MAEs, Eye 1 showed the most pronounced thinning of the retina between the external limiting membrane to the inner and outer photoreceptor segments (for example, https://labs-laboratory.com/medicine/elmisos_thickness_of_inner_subfield_right_f28517_0_0). Eye 2 showed a globally

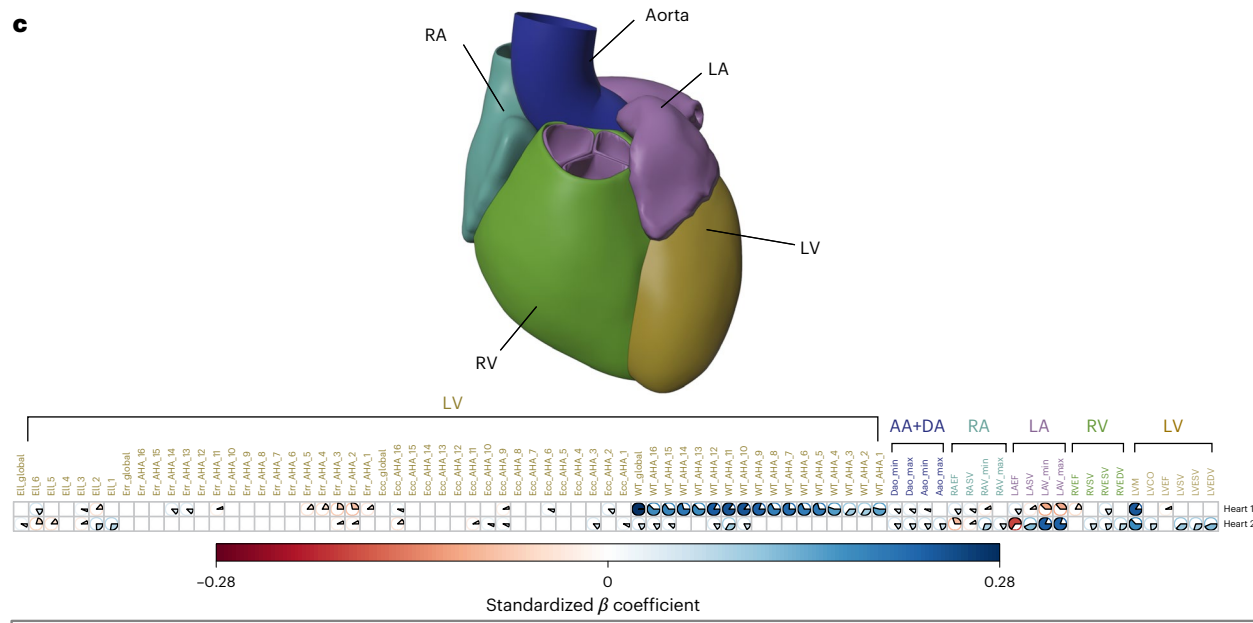
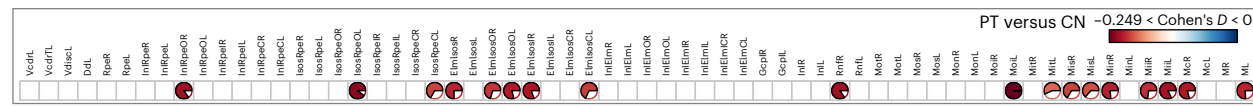
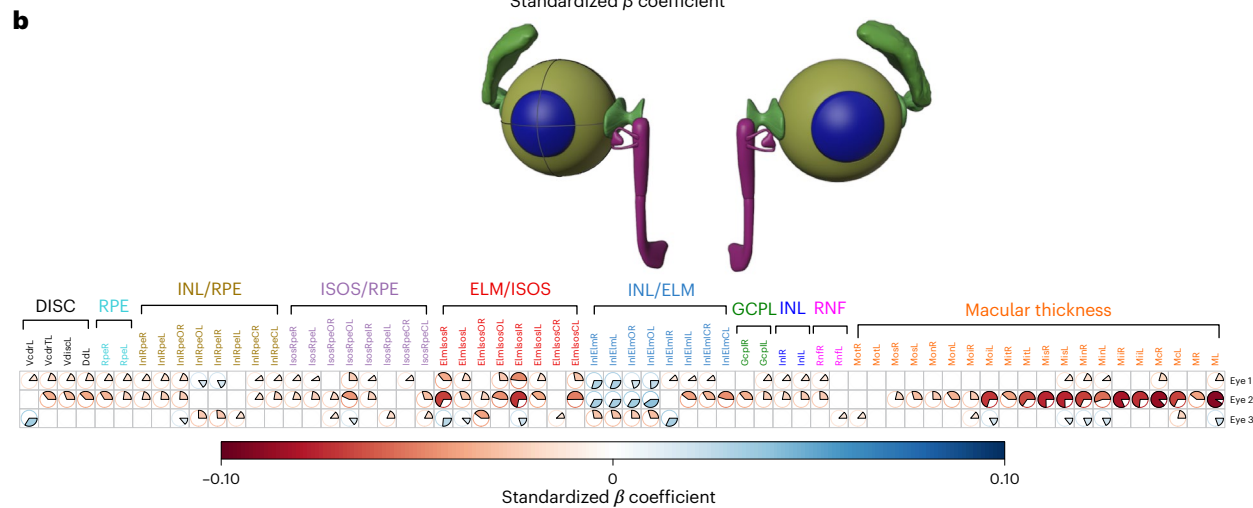
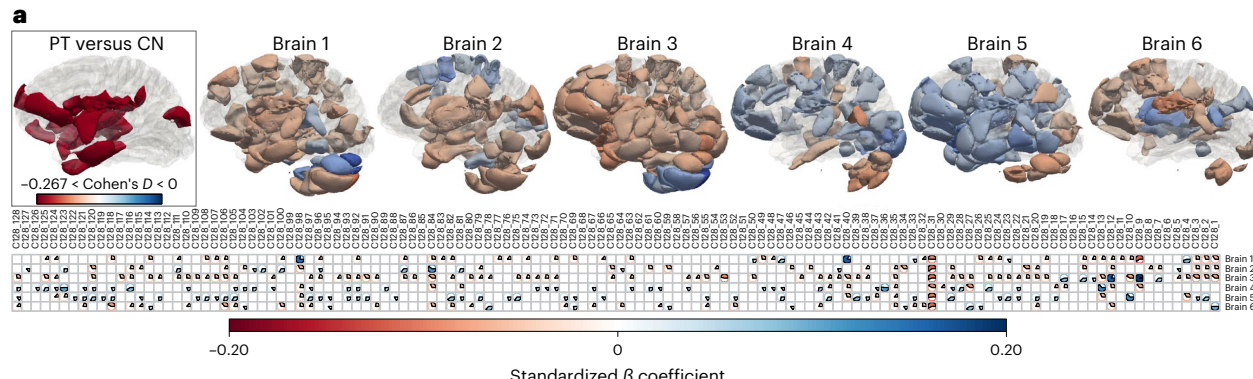
thinner retina, especially for overall macular thickness (for example, https://labs-laboratory.com/medicine/overall_macular_thickness_left_f27800_0_0) and a thicker outer nuclear and outer plexiform layer (between the inner nuclear layer and the external limiting membrane) (for example, https://labs-laboratory.com/medicine/inlelm_thickness_of_the_outer_subfield_left_f28510_0_0). Eye 3 showed a greater macular thickness, vertical cup-to-disc ratio (for example, https://labs-laboratory.com/medicine/vertical_cup_to_disc_ratio_vcdr_left_f27857_0_0) and other macular thickness measures (Fig. 2b). These imaging patterns manifested in the UKBB test dataset (Supplementary Fig. 1b). Ocular disorders, such as age-related macular degeneration and glaucoma, show pronounced phenotypic heterogeneity^{36,37}, and our study elucidates the complex morphological alterations underlying these diseases through three eye dimensions with distinct imaging patterns.

For pan-disease of the heart, the CN–PT analyses showed globally increased measures regarding cardiac and aortic function, except for the left atrium (LA) ejection fraction (https://labs-laboratory.com/medicine/la_ejection_fraction_f24113_2_0) and the left ventricle (LV) radial strain AHA (American Heart Association) 3 (Err_AHA_3) and Err_AHA_3. Heart 1 showed the most profound increase in measures of the LV mean myocardial wall thickness (for example, https://labs-laboratory.com/medicine/lv_mean_myocardial_wall_thickness_aha_9_f24132_2_0). Heart 2 showed a global increase in cardiac and aortic function, but with a decrease in LA ejection fraction and right atrium ejection fraction (Fig. 2c). These imaging patterns manifested in the UKBB test dataset (Supplementary Fig. 1c). Cardiovascular diseases show widespread heterogeneity across conditions and ethnic populations³⁸, and we present a comprehensive, data-driven framework elucidating the morphological heterogeneity underlying various heart disease pathophysiology. Supplementary Files 1–3 present the detailed results for the three organs.

We applied the pre-trained AI models of the six brain MAEs to three independent brain MRI datasets covering the entire AD continuum, including aging (Baltimore Longitudinal Study of Aging (BLSA)^{39,40}), preclinical AD (Anti-Amyloid Treatment in Asymptomatic Alzheimer’s (A4)^{41,42}) and mild cognitive impairment (MCI) or AD (Alzheimer’s Disease Neuroimaging Initiative (ADNI)⁴³) cohorts, which were systematically consolidated and statistically harmonized (‘The MULTI consortium’ in Methods and Supplementary Table 1). The imaging patterns of these six brain MAEs were consistently expressed throughout the AD continuum (Extended Data Fig. 1a–c), and their longitudinal follow-ups from ADNI⁴³ (Extended Data Fig. 1d). Brain 1 and Brain 3 showed positive associations with cerebrospinal fluid (CSF) levels of total tau (t-tau_{181p}) (Brain 1, $P = 3.90 \times 10^{-4}$, $r = 0.17$; Brain 3, $P = 3.06 \times 10^{-5}$, $r = 0.17$) and phosphorylated-tau181 (p-tau_{181p}) (Brain 1, $P = 6.80 \times 10^{-4}$, $r = 0.16$; Brain 3, $P = 1.25 \times 10^{-4}$, $r = 0.15$), while Brain 5 was positively linked to CSF levels of Aβ_{1–42} in ADNI (Extended Data Fig. 1e; $P = 9.11 \times 10^{-6}$, $r = 0.17$). A weak negative correlation was

Fig. 2 | The morphological patterns of the 11 MAEs for pan-disease of the brain, eye and heart. We used a weakly supervised representation learning method (Surreal-GAN¹⁰) to dissect the morphological heterogeneity of pan-disease of the brain, eye and heart. Surreal-GAN generates multiple MAEs, capturing multiple distinctive yet co-occurring imaging patterns within the same patient, taking into account disease severity. We used the standardized β coefficients from linear regression models as effect sizes to represent significant associations (two-sided P value), applying Bonferroni correction based on the total number of imaging features and MAEs. **a**, The imaging patterns of the six MAEs of the brain pan-disease. The ICD-10 codes G (diseases of the nervous system) and F (mental and behavioral disorders) were used to define the brain PT population. We identified the CN population by excluding all individuals with an ICD diagnosis recorded at any inpatient session. **b**, The imaging patterns of the three MAEs of the eye pan-disease. The ICD-10 codes H0–H5 (diseases of the eye and adnexa) were used to define the eye PT population. **c**, The imaging patterns of the two MAEs of the

heart pan-disease. We used the ICD-10 code I (diseases of the circulatory system) to define the heart PT population. We also showed the imaging patterns of the three pan-diseases in a case–control logistic regression analysis (PT versus CN). Readers can visualize the brain imaging MRI features used to compute the brain MAEs via the BRIDGEPORT knowledge portal: <https://labs-laboratory.com//bridgeport>. The eye and heart imaging features are publicly available at <https://labs-laboratory.com/medicine/eye> and <https://labs-laboratory.com/medicine/cardiovascular>. The ICD-10 code is documented at: <https://biobank.ndph.ox.ac.uk/ukb/field.cgi?id=41270>. The feature labels above the pie chart represent high-level categories of organ imaging patterns. AA, ascending aorta; DA, descending aorta; ELM, external limiting membrane; ILM, internal limiting membrane; ISOS, inner and outer photoreceptor segments; RA, right atrium; RV, right ventricle; DISC: vertical cup-to-disc ratio; GCPL: ganglion cell-inner plexiform layer; RNF: retinal nerve fibre; RPE: retinal pigment epithelium.



detected between Brain 6 and CSF p-tau_{181p} in ADNI ($P = 5.40 \times 10^{-4}$, $r = -0.01$), which was then confirmed using plasma p-tau_{181p} in UKBB ($P = 0.01$, $r = -0.06$). These findings align with previous studies connecting AD with these CSF neuropathological biomarkers⁴⁴. In addition, Brain 2 was most strongly associated with fluid intelligence ($P = 6.94 \times 10^{-21}$, $r = -0.05$) and numerical memory ($P = 1.56 \times 10^{-16}$, $r = -0.05$) in UKBB, among other significant associations with cognition (Extended Data Fig. 1f). Supplementary File 4 and Supplementary Tables 2–3 present the detailed results. Supplementary Note 1 discusses our strategies and considerations for harmonizing multisite brain MRI data.

The phenotypic landscape between the 11 MAEs and 9 multi-organ BAGs and 2,101 DEs

We then associated the 11 MAEs with 9 multi-organ BAGs from our previous study¹⁷ and 2,101 ICD-10-defined DEs from UKBB. We hypothesized that the PWAS ('Phenotypic analysis' in Methods) results showed both within-organ specificity (brain MAEs linked to brain-related phenotypes or traits) and cross-organ interactions (brain MAEs linked to other organ systems).

We observed stronger (standardized β coefficient from the regression model) MAE–BAG associations for within-organ than for cross-organ MAE–BAG pairs. For example, the strongest association was observed between Eye 2 and eye BAG ($\beta = 0.059 \pm 0.0016$), higher than the association between Eye 2 and brain BAG ($\beta = 0.026 \pm 0.0053$) and between Eye 3 and pulmonary BAG ($\beta = 0.011 \pm 0.0025$). When comparing the effect sizes across the three organs, the eye MAEs showed the strongest correlations between organ-specific MAE–BAG pairs, followed by the heart and brain MAEs. Several factors can contribute to this observation. For example, the eye's structure and function are highly conserved across species⁴⁵, making it more susceptible to age-related changes. Furthermore, the eye has a high metabolic rate, leading to increased oxidative stress and cellular damage⁴⁶. In contrast, the brain's compensatory mechanisms, such as neuroplasticity and functional redundancy⁴⁷, may help to mitigate age-related declines; the brain comprises diverse cell types, each with unique aging profiles, which might contribute to its relative resilience⁴⁸ (Fig. 3a and Supplementary Table 4). Extended Data Fig. 2a–c showcases the scatterplot of representative MAE–BAG associations of the three organs.

We then associated the 11 MAEs with ICD-10-based DEs (at least >20 patients) using UKBB data. Among the 11 MAEs and 2,101 DEs, we identified 3 significant MAE–DE associations ($P < 0.05/2,101/11$) for the brain, 127 for the eye and 66 for the heart MAEs (Fig. 3b). For example, Brain 6 was positively linked to cerebral infarction (ICD-10 code I639; $\beta = 0.40 \pm 0.08$, $P = 2.16 \times 10^{-6}$). The eye MAEs were not only associated with DEs of the eye but also with those of other organ systems. For example, primary open-angle glaucoma (ICD-10 H401) was positively associated with both Eye 1 ($\beta = 0.44 \pm 0.09$, $P = 3.74 \times 10^{-7}$) and Eye 3 ($\beta = 0.33 \pm 0.07$, $P = 6.02 \times 10^{-9}$). Multiple sclerosis was positively linked to all 3 eye MAEs ($P < 4.97 \times 10^{-9}$, $\beta > 0.35$). Heart diseases such as hypertension (ICD-10 I10) were also positively linked to all MAEs ($P < 6.02 \times 10^{-9}$, $\beta > 0.11$). The 2 heart MAEs were associated

with heart-related diseases, including angina pectoris (I209 versus Heart 2, $\beta = 0.42 \pm 0.04$, $P = 9.49 \times 10^{-24}$), acute subendocardial myocardial infarction (I214 versus Heart 2, $\beta = 0.41 \pm 0.07$, $P = 2.47 \times 10^{-8}$) and atherosclerotic heart disease (I251 versus Heart 1, $\beta = 0.21 \pm 0.04$, $P = 1.22 \times 10^{-7}$). Diseases of other organs were also linked to the 2 heart MAEs, such as cataracts (H269 versus Heart 2, $\beta = 0.20 \pm 0.03$, $P = 4.88 \times 10^{-8}$), non-insulin-dependent diabetes mellitus (H269 versus Heart 1 and Heart 2, $\beta > 0.25$, $P < 4.41 \times 10^{-10}$) and obesity (H669 versus Heart 2, $\beta = 0.25 \pm 0.04$, $P = 1.64 \times 10^{-7}$). Finally, we also found that different types of cancer were also linked to the MAEs, such as malignant neoplasm of bronchus and lung (C349; Eye 2), malignant neoplasm of corpus uteri (C541; Eye 1) and submucous leiomyoma of the uterus (D250; Brain 2 and Brain 4). Increasing evidence pinpoints potential connections between cancer and certain brain and eye diseases, although these relationships are intricate and not yet fully understood. For example, it has been proposed that AD progresses through mechanisms and pathways similar to certain cancers. Intriguingly, the two have a noted negative association⁴⁹ (Supplementary Note 2).

In our secondary PWAS ('Secondary PWAS' in Methods), we also linked the 11 MAEs to all other clinical variables not directly related to the 3 organs, exemplified by the strong association between Heart 2 and 'alcohol drinker status' (Field ID = 20117) ($\beta = -0.01 \pm 0.001$, $P = 4.00 \times 10^{-31}$). The potential beneficial effect of alcohol consumption on cardiovascular diseases, as suggested by observational studies, has been a continued debate in the community because Mendelian randomization studies⁵⁰ challenge this notion. The detailed results are discussed in Supplementary Fig. 3, Supplementary File 6 and Supplementary Note 2. Extended Data Fig. 2d–f showcases the box plot of representative MAE–DE associations of the three organs.

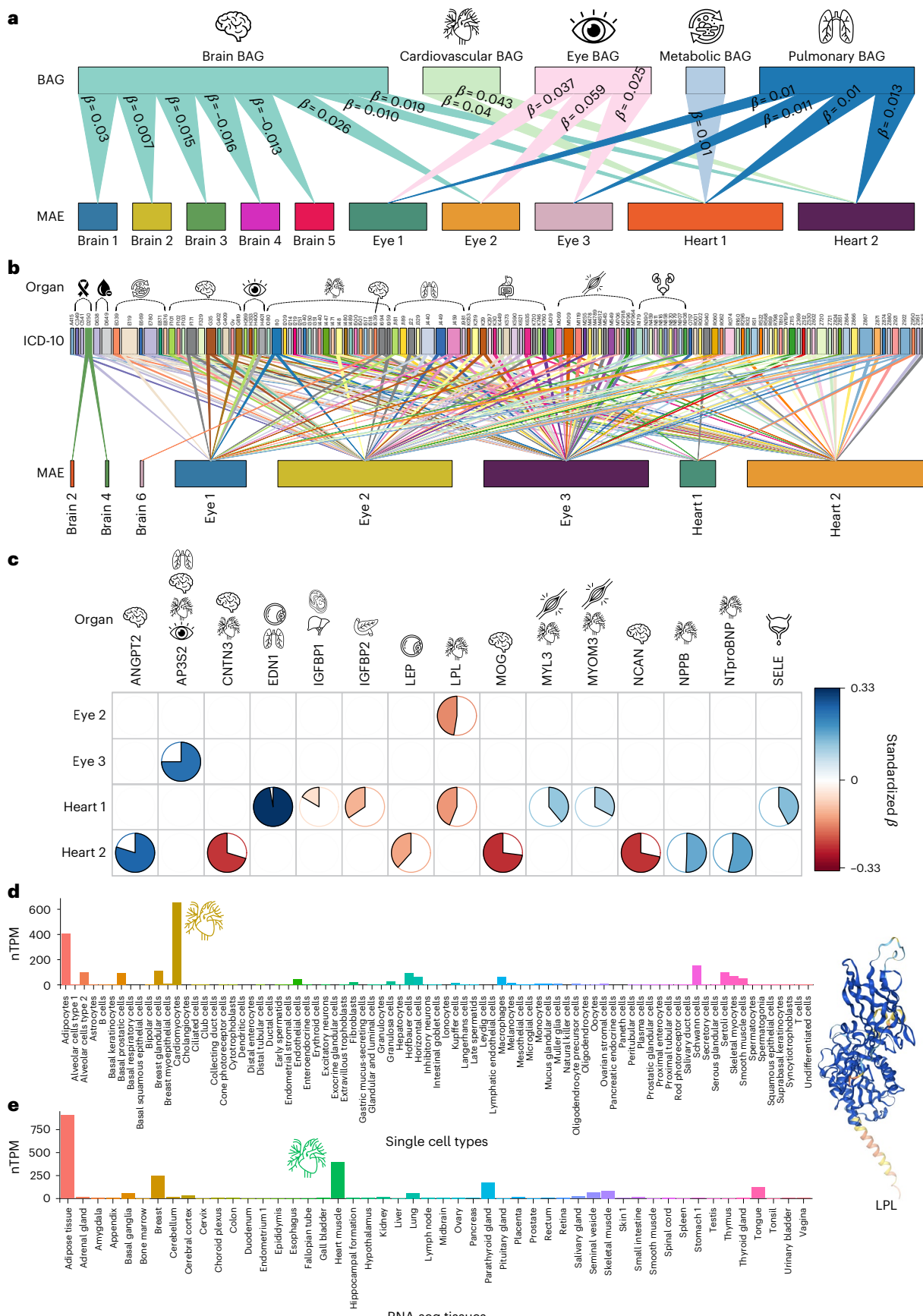
The proteomic profile between the 11 MAEs and 2,923 plasma proteins

Our ProWAS analyses ('ProWAS' in Methods) linked the 11 MAEs to 2,923 plasma proteins using the Olink platform and evaluated the expression profile (with-organ or cross-organ) of significant proteins using organ- and/or tissue-specific (single-cell) RNA-seq data ('Tissue- or organ-specific map of the expression of the human proteome' in Methods).

After correcting for multiple comparisons ($P < 0.05/2,923/11$), we found 16 significant associations. For example, Heart 1 ($\beta = -0.14 \pm 0.03$, $P = 9.98 \times 10^{-7}$, $N = 3,130$) and Eye 2 ($\beta = -0.15 \pm 0.03$, $P = 1.46 \times 10^{-6}$, $N = 3,352$) were negatively associated with the LPL protein (Fig. 3c). LPL plays a pivotal role in triglyceride metabolism by catalyzing the hydrolysis of triglycerides from circulating chylomicrons and VLDL, thereby facilitating lipid clearance from the bloodstream and regulating lipid utilization and storage. We showed an organ-specific expression pattern for LPL by showing it exhibited the highest expression level (655.2 normalized transcripts per million (nTPM)) in cardiomyocytes among 81 single-cell types (Fig. 3d). At the tissue level, LPL expression was prominently elevated in the heart muscle (394.5 nTPM) compared with other tissues, further supporting its cardiac-enriched expression profile (Fig. 3e). Detailed statistics of our ProWAS are presented in Supplementary File 7a. Another significant signal was observed between

Fig. 3 | The phenotypic landscape and proteomic profile of the 11 MAEs of the brain, eye and heart. **a**, Phenotypic associations (PWAS) between the 11 MAEs and 9 AI-derived BAGs from our previous study¹⁷. A linear regression model was constructed to predict the MAEs using the BAGs, adjusting for various covariates (for example, age and sex) and organ-specific covariates (for example, blood pressure for heart MAEs and scanner positions for brain MAEs). The β values were standardized. Significant associations were determined by applying Bonferroni correction based on the 9 BAGs and the 11 MAEs (two-sided $P < 0.05/9/11$). **b**, PWAS between the 11 MAEs and DEs defined by the ICD-10 code (>20 patients) were evaluated by constructing a logistic regression model to predict the DE of interest using the BAGs and related covariates. Significant associations were determined by applying Bonferroni correction based on the 11 MAEs and the

2,101 DEs (two-sided $P < 0.05/2,101/11$). **c**, ProWAS between the 11 MAEs and 2,923 plasma proteins via a linear regression model. Using RNA-seq and single-cell data, we also annotated the primary organ systems linked to each significant protein based on their data-type-specific expression levels. Significant associations were determined by applying Bonferroni correction based on the 11 MAEs and the 2,923 proteins (two-sided $P < 0.05/2,923/11$). **d**, The single-cell-type expression (that is, nTPM) for the LPL protein using single-cell transcriptomics data from the HPA. **e**, The tissue-specific RNA expression overview for the LPL protein using data from HPA and the GTEx project. We present the LPL protein structure as predicted by the AlphaFold model (Monomer v.2.0 (ref. 156)). The exact P values are presented in Supplementary Files 6–7.



Eye 3 and the AP3S2 protein, which showed high RNA expression in the tissues of the brain, eye and heart (Supplementary Fig. 4). Extended Data Fig. 2g–j showcases the scatterplot of representative MAE–protein associations of the eye and heart, the protein–protein interaction (PPI) network ('PPI network analysis' in Methods) for the LPL protein and the volcano plot for Heart 2 ProWAS results. Heart 1 and Heart 2 showed more significant plasma protein associations than brain and eye MAEs. Biologically, this may be due to several factors. First, the heart's proximity to circulation allows direct interaction with many plasma proteins, often produced by or related to cardiovascular function and disease^{51,52}. Furthermore, heart-related diseases typically cause systemic changes that can be easily detected in the blood, whereas brain diseases often involve localized molecular changes relatively confined behind the blood–brain barrier⁵³.

The results of ProWAS of brain MAE using UKBB's Olink and the comparison with BLSA SomaScan proteomics data are discussed in Supplementary Note 3, Supplementary File 7b and Supplementary Fig. 12. Importantly, we observed that SomaScan proteins showed stronger associations with the 6 brain MAEs than Olink proteins, despite BLSA SomaScan having a much smaller sample size ($N = 924$). The β coefficients of the 44 common significant MAE–protein pairs showed moderate correlation (Pearson's $r = 0.26$), which agrees with a previous investigation⁵⁴. This observation may be attributed to SomaScan's greater sensitivity and broader protein coverage, which likely enhances its ability to detect significant associations.

The genetic architecture of the 11 MAEs

We first conducted GWASs to identify common genomic loci and regions shared among the 11 MAEs across the 3 organs. Next, we estimated three key genetic parameters: (1) SNP-based heritability (h^2_{SNP}), (2) natural selection signatures (S), and (3) polygenicity (π). Finally, we performed gene set enrichment analyses to determine whether MAE-associated genes were enriched in any drug categories, providing insights for potential drug repurposing and cell- and tissue-specific partitioned heritability estimates ('Genetic analyses' in Methods).

For the 11 primary GWASs ('GWAS' in Methods) using European ancestry populations, we identified 42 ($P < 5 \times 10^{-8}/11$), 56 and 7 genomic locus–MAE associations for the 6 brain, 3 heart and 2 heart MAEs, respectively. We denoted the genomic loci using their top lead SNPs (Supplementary Method 1) defined by FUMA, fully considering linkage disequilibrium (LD); the genomic loci are presented in Supplementary File 8. To visually present the shared genomic region among the 11 MAEs, we showed that only 5, 1 and 1 common cytogenetic regions (based on the GRCh37 cytoband) were jointly linked to the brain, eye and heart MAE pairs, respectively (Fig. 4a). In general, the 11 MAEs showed limited genetic overlap based on their physical locations in the genome, which was subsequently supported by the weak pairwise genetic and phenotypic correlations observed (Fig. 5a). We performed several quality checks to scrutinize the robustness of the primary GWAS, and a detailed discussion is presented in Supplementary Note 4. We also performed a genome-wide association look-up analysis (PheWAS) using the GWAS Atlas⁵⁵ platform ('PheWAS' in Methods) to link the top lead SNPs of each locus with previous literature (Supplementary Note 5 and Supplementary Fig. 5). Manhattan and Q–Q plots of the 11 primary GWASs are presented in our MEDICINE portal (for example, eye MAEs, <https://labb.laboratory.com/medicine/eye>) and Supplementary Fig. 6. Extended Data Fig. 3 presents the trumpet plots of the effective allele frequency versus the β coefficient of the 11 primary MAE GWASs.

We estimated the h^2_{SNP} to quantify the proportion of phenotypic variance attributable to common genetic variants across the genome and organs ('SNP-based heritability' in Methods). The GCTA⁵⁶ software revealed significant h^2_{SNP} in all 6 brain MAEs ($0.26 < h^2_{\text{SNP}} < 0.53$, $P < 1 \times 10^{-20}$) using individual-level genotype data, followed by the 3 eye

MAEs ($0.30 < h^2_{\text{SNP}} < 0.40$, $P < 1 \times 10^{-20}$) and the 2 heart MAEs ($0.28 < h^2_{\text{SNP}} < 0.39$, $P < 1 \times 10^{-20}$) (Fig. 4b). The results generated by linkage disequilibrium score regression (LDSC)⁵⁷ ($h^2_{\text{SNP}} = 0.20 \pm 0.05$) and SbayesS⁵⁸ ($h^2_{\text{SNP}} = 0.19 \pm 0.05$), which use GWAS summary data and a reference panel for LD information, showed a lower estimate than GCTA ($h^2_{\text{SNP}} = 0.37 \pm 0.09$, t value > 5.49 , $P < 2.24 \times 10^{-5}$); the 3 sets of estimates were significantly correlated with each other ($P < 1.42 \times 10^{-6}$, $r > 0.97$). Detailed statistics are presented in Supplementary Table 5.

Next, we explored the evolutionary processes of pan-diseases across the 3 organs, particularly how these traits evolve and adapt through natural (for example, negative or purifying) selection and genetic variation; we applied the SBayesS⁵⁸ method to calculate S and π for the 11 MAEs ('Selection signature and polygenicity estimate' in Methods). Eye 3 showed the most prominent negative S (-0.88 ± 0.10) (Fig. 4c), echoing its lowest π estimate (0.002 ± 0.0004). Eye 1–3 showed the lowest π estimates (Fig. 4d and Supplementary Table 6). The observed cross-organ trends in negative S and π estimates can be attributed to multiple factors. First, the evolutionary conservation of the retina's structure and function across species⁴⁵ suggests it is subject to strong evolutionary pressure to maintain stability. Even minor genetic changes affecting retinal function may have detrimental effects, resulting in stronger purifying (negative) selection against harmful variants. In contrast, organs such as the brain and heart may display greater evolutionary flexibility or redundancy (that is, more complicated compensatory pathways) in their genetic architecture, allowing for a higher tolerance of mutations. In addition, brain disorders are often more polygenic than eye and heart diseases due to the brain's complexity and the large number of genes involved in its development, function and maintenance^{59,60}.

We performed a gene–drug–disease enrichment analysis ('Gene–drug–disease network' in Methods) using positionally and functionally mapped genes linked to the 11 MAEs within drug–target gene sets from the DrugBank database⁶¹. This analysis generated a gene–drug–disease network to identify drugs with repurposing potential, a strategy shown to enhance the success rate of drug development according to existing literature^{62,63}. For the Brain 3-mapped genes (that is, microtubule-associated protein tau (*MAPT*), *FGFR2* and *IGF1*), we found five significant interactions with five drugs for treating neoplasms of uncertain or unknown behavior. For example, docetaxel is a chemotherapy drug used to treat various types of cancer, including lung cancer (for example, NCT code NCT04303780) and breast cancer, often combined with other medications. The mapped *MAPT* gene is a targeted gene for several drugs, including neurodegenerative conditions such as AD. Another example is BIIB080, also known as IONIS-MAPTRx (NCT code NCT03186989), an investigational drug targeting the *MAPT* gene to treat AD⁶⁴. We also found abundant cancer-related interactions (for example, docetaxel) for Eye 1 and Eye 3. For instance, prostaglandin F2- α (PGF2 α ; mapped gene *PTGDR2*) is a naturally occurring prostaglandin with several pharmaceutical uses, primarily related to its role in reproductive health and for treating glaucoma (for example, latanoprost⁶⁵). NSC8895 (mapped gene *RHO*) is a small-molecule drug investigated for its potential as an anti-cancer agent or for other therapeutic uses. Finally, Heart 1-mapped genes were linked to drugs or molecules treating several organ-specific diseases. For example, RG-7010 was initially developed by Roche to treat several motor neuron diseases, including amyotrophic lateral sclerosis (Fig. 4e). Detailed statistics are presented in Supplementary File 9.

We also provided evidence for the significant enrichment of cancer-related drugs in our gene–drug–disease network using RNA-seq data in 17 cancer types from the TCGA database. This was exemplified by the *MAPT* protein linked to Brain 2, Eye 1, Eye 2 and Heart 2 (Fig. 4e). Enhanced cancer specificity was observed in breast cancer (6.7 fragments per kilobase of transcript per million mapped reads (FPKM)) and glioma (12.2 FPKM) (Supplementary Fig. 7a). Correspondingly, the *MAPT* protein showed high single-cell-type-specific expression

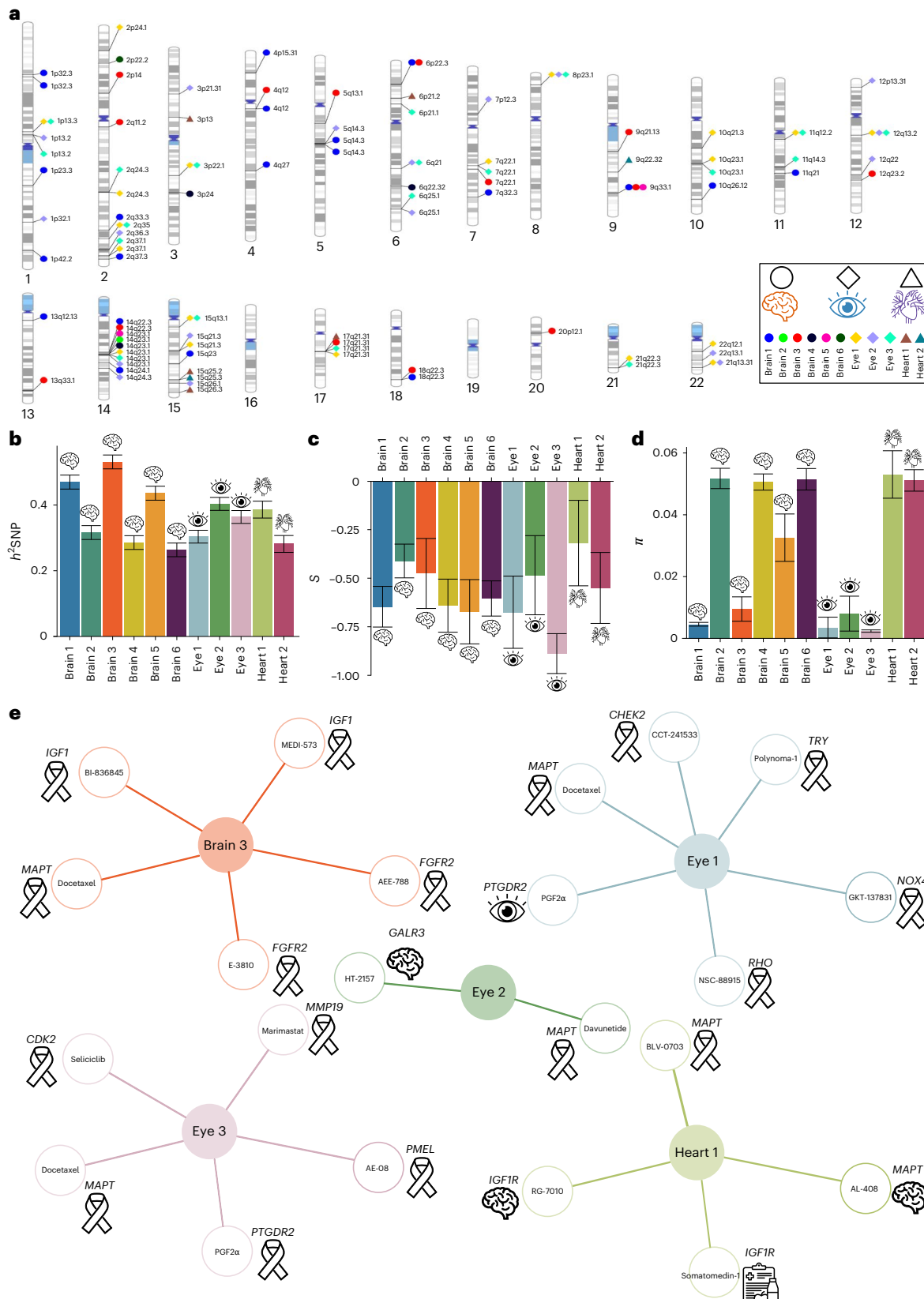


Fig. 4 | The genetic architecture of the 11 MAEs of the brain, eye and heart.

a, Cytogenetic regions where the genomic region was jointly linked to the three organ-specific MAEs. Bonferroni correction was applied to denote significant genomic loci associated with the brain PSCs (two-sided $P < 5 \times 10^{-8}/11$; Supplementary File 8). **b**, h^2_{SNP} was estimated using the GCTA software for the 11 MAEs ($25,776 < N < 35,445$). **c**, S was estimated using the SBayesS software for

the 11 MAEs ($25,776 < N < 35,445$). **d**, The π was estimated using the SBayesS software for the 11 MAEs ($25,776 < N < 35,445$). The mean and s.e. of each inferred statistic are shown. **e**, A gene–drug–disease network quantifies an enrichment of the MAE-related gene sets in the target of clinical indication categories and captures potentially repositionable drugs targeting the gene set using the DrugBank database.

profiles in the brain (Supplementary Fig. 7b) and breast tissues (Supplementary Fig. 7c). Research has shown that breast cancer tissues and glioma show increased levels of tau protein, which may contribute to tumor progression by promoting key processes, including enhanced cell proliferation and migration, increased invasiveness, modulation of signaling pathways and facilitation of metastasis⁶⁶. Finally, we also performed cell- and tissue-specific partitioned heritability estimates⁶⁷ using data from three cell types, multitissue gene expression and chromatin interactions ('Cell- and tissue-specific partitioned heritability estimate' in Methods) to further support the organ-specific patterns of our GWAS signals (Supplementary File 10). Significant heritability enrichment ($P < 0.05/697/11$) was found for Brain 5 in ganglion eminence-derived primary cultured neurospheres ($P = 3.39 \times 10^{-6}$) and fetal brain tissues ($P = 1.79 \times 10^{-10}$) in histone H3 lysine 4 methylation.

The genetic correlation between the 11 MAEs and other clinical traits

We estimated the genetic correlation between the 11 MAEs for 3 biomarker sets: (1) between the 11 MAEs, (2) with the 9 BAGs, and (3) with 525 DEs ('Genetic correlation' in Methods).

We estimated the pairwise phenotypic correlation (p_c via Pearson's r) and genetic correlation (g_c) for the 11 MAEs. First, our results revealed a pronounced within-organ correlation structure. In contrast, cross-organ correlations were much weaker, reflecting the scarcity of the shared genomic regions among the three organs (Fig. 4a). An exception emerged between Brain 1 and Heart 1, which showed a positive g_c (0.20 ± 0.06 , $P = 8.0 \times 10^{-4}$) (Fig. 5a). Furthermore, our analysis revealed a strong concordance between the genetic correlations and phenotypic correlations across the 11 MAEs, providing empirical support for the long-standing Cheverud conjecture⁶⁸. One exception was observed between Brain 1 and Brain 3, where a negative g_c and a weak positive p_c were obtained. This phenomenon is likely influenced by multiple factors, including gene–environment interactions⁶⁹, epistasis⁷⁰, pleiotropy, LD and genetic heterogeneity. Detailed statistics are presented in Supplementary Table 7.

We then observed strong within-organ associations between the MAEs and their respective organ BAGs (Fig. 5b) and DEs (Fig. 5c). For example, we found that Eye 1 ($g_c = 0.31 \pm 0.08$, $P = 1.0 \times 10^{-4} < 0.05/11/9$) and Eye 2 ($g_c = 0.38 \pm 0.06$, $P = 1.0 \times 10^{-10}$) were positively associated with eye BAG, and Heart 1 ($g_c = 0.18 \pm 0.05$, $P = 5.0 \times 10^{-4}$) and Heart 2 ($g_c = 0.28 \pm 0.07$, $P = 8.0 \times 10^{-5}$) with cardiovascular BAG. Detailed statistics are presented in Supplementary Table 8. Among 525 unique DEs from FinnGen and the Psychiatric Genomics Consortium (PGC), we found 8 significant MAE–DE associations, highlighting prominent genetic associations between Heart 2 and various heart and vascular diseases, such as cardiovascular disease (FinnGen code FG_CVD, $g_c = 0.34 \pm 0.05$, $P < 1.0 \times 10^{-10}$), hypertension (I9_HYPHTENS, $g_c = 0.33 \pm 0.06$, $P < 1.0 \times 10^{-10}$) and heart failure (I9_I9_HEARTFAIL_EXMORE, $g_c = 0.37 \pm 0.08$, $P < 1.0 \times 10^{-10}$). Detailed statistics are presented in Supplementary File 11.

Multilayer causal networks support the endophenotype hypothesis by showing MAE functions as a causal intermediate phenotype

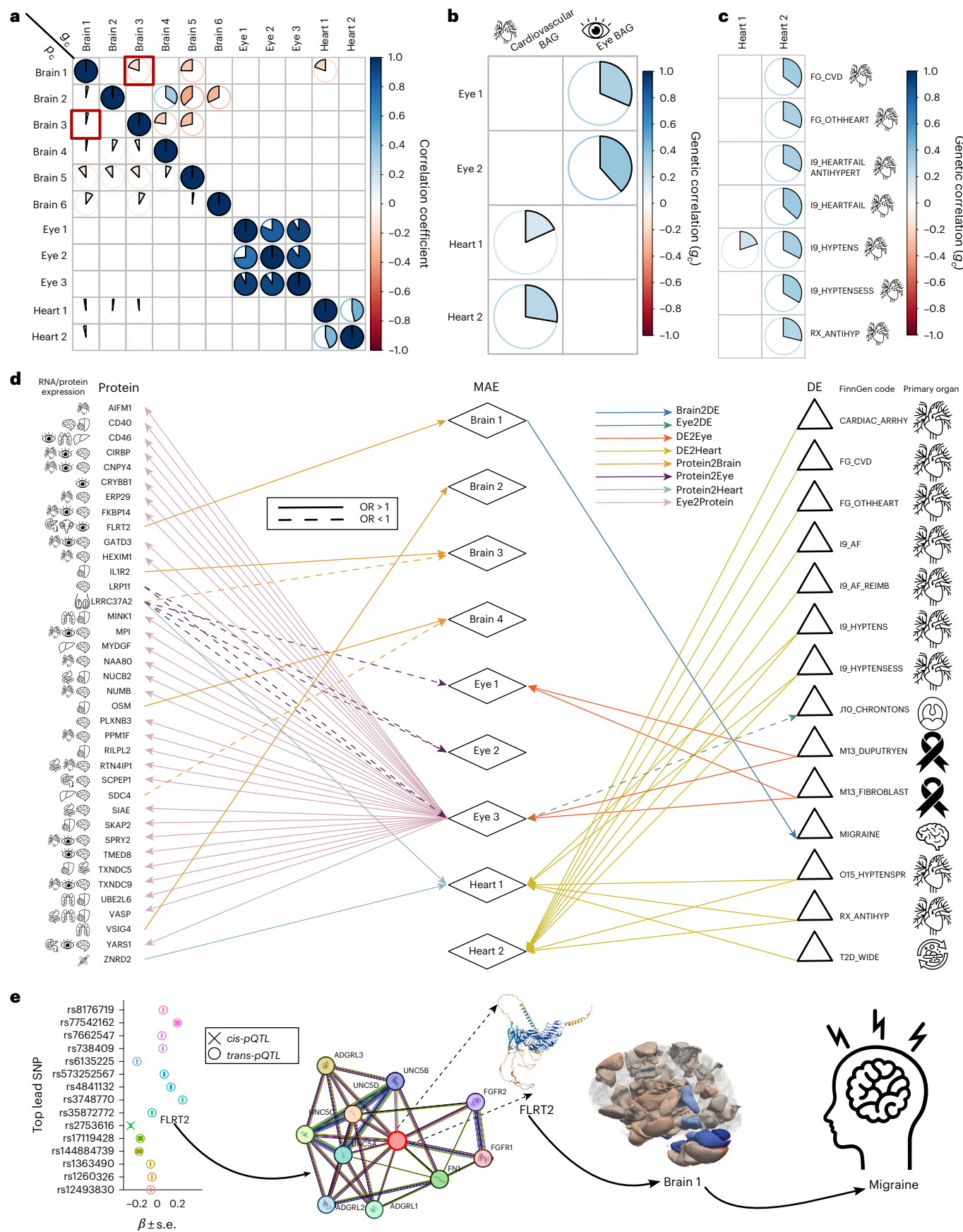
We further deciphered the genetic associations by building a detailed causal network, spanning underlying genetics, proteomics, MAEs and DEs. Supplementary Fig. 8 illustrates a causal pathway inspired by the endophenotype hypothesis²⁸. This was accomplished using two-sample, bidirectional Mendelian randomization⁷¹, which combined large-scale GWAS summary data from UKBB, FinnGen and PGC. We ensured the robustness of our results by performing systematic quality checks and sensitivity analyses ('Two-sample bidirectional Mendelian randomization' in Methods).

We performed Mendelian randomization analyses among the 2,923 plasma proteins, 11 MAEs and 525 DEs, resulting in 12 directional causal networks (for example, Brain2DE and Protein2Eye) depending on the exposure and outcome variables. After a quality check procedure for instrumental variable (IV) selection (>8 IVs) and Bonferroni correction, we identified 44 significant protein–MAE associations ($P < 0.05/\text{number of proteins}$) and 24 MAE–DE associations ($P < 0.05/\text{number of DEs}$) (Fig. 5d). For the Protein2Brain network, we identified six significant causal relationships from six proteins to four brain MAEs. For example, a potential causal relationship was established from the LRRC37A2 protein to Brain 3 ($P = 7.64 \times 10^{-8}$; odds ratio (OR) = 0.95, 95% confidence interval (CI) = (0.93, 0.96); number of IVs = 9). Within the Protein2Eye network, we found five significant signals from two proteins to three eye MAEs. For instance, the LRP11 protein showed a potential causal effect on Eye 2 ($P = 1.57 \times 10^{-13}$; OR = 0.93, 95% CI = (0.91, 0.96); number of IVs = 13). For the Protein2Heart network, two potential causal relationships were found from two proteins to Heart 1. For example, LRRC37A2 was positively linked to Heart 1 ($P = 5.03 \times 10^{-10}$; OR = 1.07, 95% CI = (1.04, 1.09); number of IVs = 9). For the Eye2Protein network, we found 31 causal relationships from Eye 3 to 30 proteins. For example, Eye 3 was causally linked to the TXNDC9 protein ($P = 1.61 \times 10^{-6}$; OR = 1.17, 95% CI = (1.10, 1.24); number of IVs = 21), with prominent expression levels in the brain, eye and heart.

For the Brain2DE network, we found that Brain 1 was causally linked to migraine disorder (FinnGen code MIGRAINE_TRIPTAN, $P = 8.77 \times 10^{-5}$; OR = 1.16, 95% CI = (1.08, 1.26); number of IVs = 24). For the Eye2DE network, Eye 3 was negatively linked to chronic diseases of tonsils and adenoids (J10_CHRONTONSADEN, $P = 2.0 \times 10^{-5}$; OR = 0.87, 95% CI = (0.81, 0.93); number of IVs = 20). We did not find any significant signals for the Heart2DE and Heart2Protein networks due to the limited power of the heart MAE GWASs (<8 IVs), nor for the DE2Brain network, which did not survive the multiple comparisons. For the DE2Eye network, we found five causal links from two DEs to Eye 1 and Eye 3. For instance, fibroma was positively linked to Eye 1 (M13_FIBROBLASTIC, $P = 2.23 \times 10^{-6}$; OR = 1.07, 95% CI = (1.04, 1.10); number of IVs = 18). For the DE2Heart network, we found 19 causal links from 10 DEs to Heart 1 and Heart 2. For example, type 2 diabetes was positively linked to Heart 1 (T2D_WIDE, $P = 1.225 \times 10^{-3}$; OR = 1.08, 95% CI = (1.03, 1.12);

Fig. 5 | Deciphering multilayer causal networks from genetic correlation to causality. **a**, Phenotypic association (p_c) and genetic association (g_c) between each pair of the 11 MAEs. Genetic correlations largely mirror phenotypic correlations⁶⁸ of the MAE pairs except for the pair between Brain 1 and Brain 3 (red-colored squares). **b**, Genetic correlation between the 11 MAEs and the 9 BAGs from our previous multi-organ BAG study¹⁷. **c**, Genetic correlation between the 11 MAEs and the 525 DEs using GWAS summary statistics from FinnGen and PGC. For **a–c**, we used the Bonferroni correction to account for multiple comparisons using stringent two-sided P value thresholds adjusted based on the total number of MAEs and phenotypes or DEs examined. **d**, We constructed a three-layer protein–MAE–DE causal network by using bidirectional two-sample Mendelian randomization, following a rigorous quality control procedure to select exposure and IVs (number of IVs >8), correct for multiple comparisons (based on either the number of exposure or outcome variables) and perform

sensitivity analyses (for example, horizontal pleiotropy and removing overlap populations) to scrutinize the robustness of our results. The Heart2DE and Heart2Protein networks were not included due to insufficient IVs after a quality check (<8). The DE2Brain and Heart2Protein networks are not shown because the results did not survive the correction for multiple comparisons. **e**, A representative causal pathway example shows how pQTLs (both *cis* and *trans*) influence the FLRT2 protein, affecting Brain 1 and increasing the risk of migraine disorder. We present the FLRT2 protein structure as predicted by the AlphaFold model (Monomer v.2.0 (ref. 156)), along with a PPI network. This network emphasizes its interaction with UNC5D and other members of the UNC5 family, which are all crucial for processes such as cell–cell adhesion, axon guidance and cell migration at the cellular level, and the development of cortical neurons and cardiac morphogenesis at the pathway level.



number of IVs = 62) (Fig. 5d). Detailed statistics are presented in Supplementary File 12. The results for sensitivity analyses are presented in Supplementary Dataset 1.

We constructed a multilayer causal network and showcased an example to support the endophenotype hypothesis, especially through the mediational model. Our causal analysis revealed a causal path whereby the FLRT2 protein exerted a causal influence on Brain 1 ($P = 3.83 \times 10^{-5}$; OR = 1.07, 95% CI = (1.04, 1.11); number of IVs = 16), which then subsequently increased the risk of migraine disorder (MIGRAINE_TRIPTAN, $P = 8.76 \times 10^{-5}$; OR = 1.17, 95% CI = (1.08, 1.25); number of IVs = 24), suggesting a sequential causal relationship between FLRT2, AI-derived brain structure and migraine susceptibility. To further confirm the vertical pleiotropy (that is, mediational model) in this pathway, we first defined protein quantitative trait loci (pQTLs) of the FLRT2 protein and found that these pQTLs were not directly associated with migraine disorder. In addition, we performed an additional causal analysis using FLRT2 as the exposure and migraine as the outcome, excluding a direct causal link between the two (Fig. 5e). Extended Data Fig. 4 shows sensitivity checks for the two causal signals, confirming that the results are robust to potential violations of Mendelian randomization assumptions. Supplementary Note 6 details the sensitivity check analyses. In addition, we compared the proteome- and genome-wide association study (ProGWAS) findings of the FLRT2 protein with the *cis*- and *trans*-pQTLs identified by ref. 72, showing a strong agreement despite differences in sample sizes, the controlled covariates and the GWAS models used. A detailed discussion is presented in Supplementary Note 7 and Supplementary Fig. 9. To further elucidate the biological relevance of this pQTL, we conducted SNP-to-gene mapping using expression quantitative trait locus (eQTL) data from Genotype-Tissue Expression (GTEx) v.8, focusing on brain gene expression. This analysis identified 40 eQTL-linked SNPs associated with the *FLRT2* gene, with the strongest association showing a *P* value of 2.68×10^{-6} , particularly in the putamen, basal ganglia and spinal cord regions. SNPs or genes that are both an eQTL and pQTL are likely to have a critical role in gene regulation and protein expression, making them a valuable target for understanding disease mechanisms and developing therapies.

We also validated this causal pathway's potential cellular and molecular mechanisms using single-cell RNA-seq and proteomics data. We first performed a PPI network analysis ('PPI network analysis' in Methods). Our PPI analysis identified FLRT2 as associated with other 10 proteins, with a PPI enrichment *P* value of 8.62×10^{-8} , providing strong

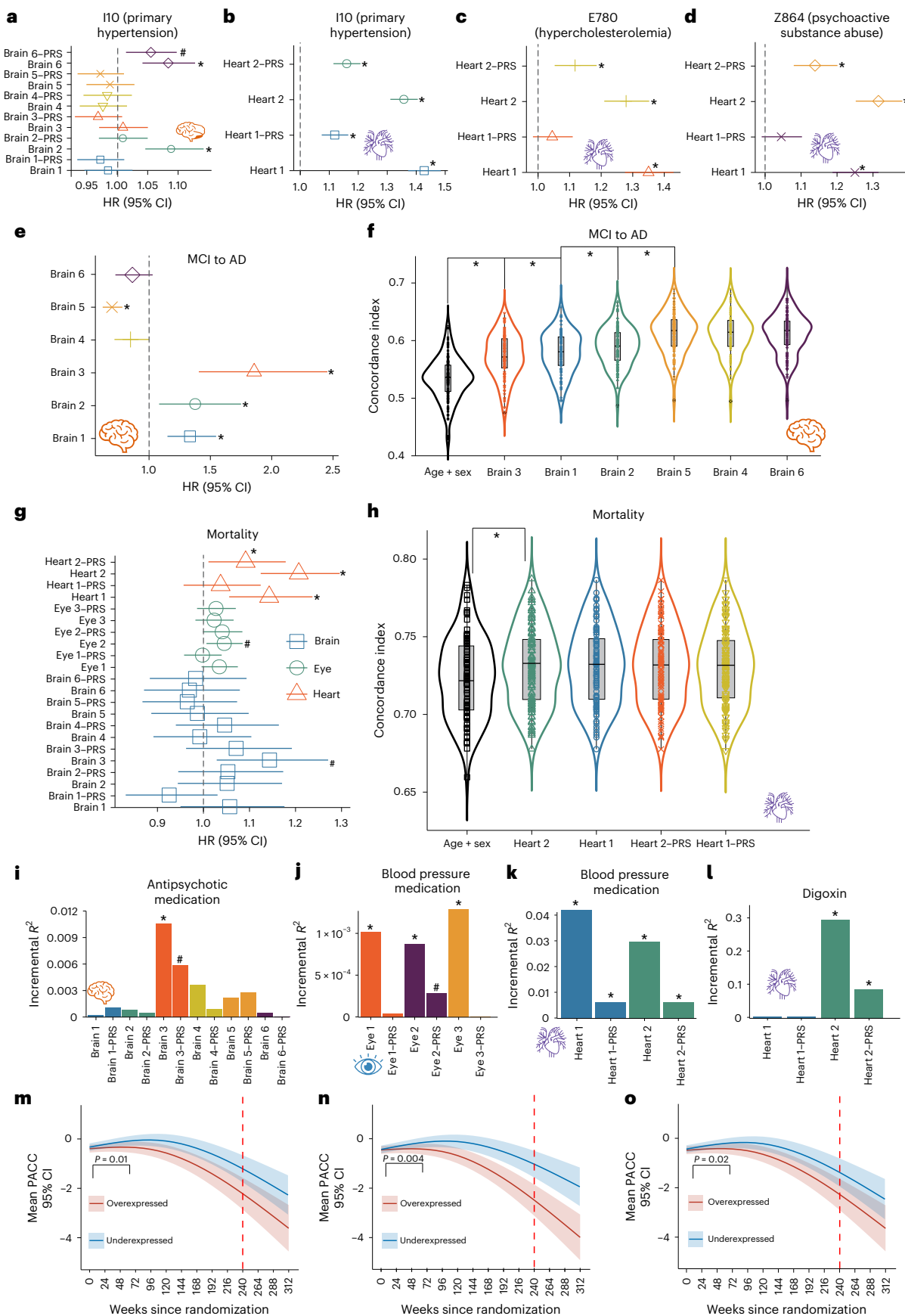
evidence that the proteins are partially biologically connected as a group. The associated proteins, including ADGRL3 and UNC5 family members, are functionally linked to FLRT2. Biologically, FLRT2 plays a crucial role in cell–cell adhesion, migration and axon guidance. It facilitates cell adhesion through interactions with ADGRL3 and potentially other latrophilins on adjacent cell surfaces. FLRT2 is involved in migrating cortical neurons during brain development by interacting with UNC5D, and mediates axon growth cone collapse, acting as a repellent in neuron guidance, likely in conjunction with other UNC5 family members. Further functional enrichment analyses reinforced the involvement of relevant biological pathways, including biological processes such as anterior–posterior axon guidance (Gene Ontology (GO) term GO:0033564; false discovery rate-corrected $P = 4.86 \times 10^{-5}$), molecular function like netrin receptor activity (GO:0005042; false discovery rate-corrected $P = 5.43 \times 10^{-8}$) and cellular components like neuron projection (GO:0043005; false discovery rate-corrected $P = 0.017$).

Previous studies on patients with migraine have shown atrophy in cortical brain areas⁷³ involved in pain processing, likely as a result of chronic stimulation in those areas. To support these morphological changes, we observed that the cerebral cortex showed the highest RNA expression score compared with other brain regions in the human brain (nTPM = 5.6), pig brain (nTPM = 36.7) and mouse brain (nTPM = 26.0) (Supplementary Fig. 10a). Additional animal experiments by ref. 74 using rodent models showed that cortical spreading depression can trigger changes in the CSF proteome, leading to an increased expression of proteins capable of activating the trigeminal nerve, thus ultimately triggering headache. Single-cell tissue enrichment analyses in the brain showed higher expression values in neuronal cells (for example, nTPM = 902.4 for excitatory neurons affected by a mutation in the C9orf72 gene) than in glial cells (Supplementary Fig. 10b) ('Tissue- or organ-specific map of the expression of the human proteome' in Methods). In addition, migraines are linked to an increased risk of cardiovascular disease, including stroke, heart attack and other serious health problems⁷⁵. FLRT2 participates in fibroblast growth factor signaling pathways at the cellular and biological pathway levels. It is essential for proper cardiac basement membrane organization and epicardium and heart morphogenesis during embryonic development. Similarly, we found single-cell tissue enrichment in the vascular tissue, highlighting the prominent enrichment of mesenchymal cells (for example, fibroblasts c-7, nTPM = 114.5) and endothelial cells (for example, endothelial cells c-19, nTPM = 129.4) (Supplementary Fig. 10c).

Fig. 6 | Prediction of and association with DEs, AD progression, mortality risk, medication use history and preclinical AD cognitive decline trajectories.

a, Brain 2 and Brain 6 show significant associations with an elevated risk of hypertension, as indicated by the corresponding HRs. Cox proportional hazard models were used to test associations and were adjusted for age and sex. **b**, Heart 1 and Heart 2 and their respective PRSs show significant associations with an increased risk of hypertension. **c**, Heart 1, Heart 2 and Heart 2-PRS show significant associations with an increased risk of hypercholesterolemia. **d**, Heart 1, Heart 2 and Heart 2-PRS show significant associations with an increased risk of psychoactive substance abuse. **e**, Brains 1, 2 and 3 are significantly linked to an increased risk of progressing from MCI to AD, while Brain 5 is associated with a reduced risk. **f**, On the basis of the significance of the brain MAEs shown in **e**, we progressively incorporated additional brain MAEs as features when fitting the Cox proportional hazard model. For each combination of features, 100 iterations of 20% holdout cross-validation were performed to derive concordance indices. **g**, Heart 1, Heart 2 and Heart 2-PRS are significantly linked to an increased mortality risk. **h**, On the basis of the significance of the brain MAEs shown in **g**, we progressively incorporated additional heart MAEs as features when fitting the Cox proportional hazard model. **i**, Brain 3 and its PRS offer additional predictive power for antipsychotic medication status on top of age and sex. **j**, Eye MAEs offer additional predictive power for blood pressure medication status on top of age and sex. **k**, Heart MAEs offer additional predictive power for blood pressure medication status on top of age and sex. **l**, Heart MAEs offer additional predictive power for the medication status of

digoxin on top of age and sex. **m**, The heterogeneity of the cognitive decline trajectories was assessed on the primary outcome, the PACC, by comparing two groups based on the expression levels of Brain 1 within the drug group. Participants were stratified into low- and high-expression groups by the median Brain 1 value (that is, underexpressed versus overexpressed Brain 1 patients). The red dashed line indicates the timeline for evaluating the drug's effects at week 240. **n**, The heterogeneity of the cognitive decline trajectories on Brain 2. **o**, The heterogeneity of the cognitive decline trajectories on Brain 3. The symbol * indicates statistical significance after the Bonferroni correction, and the symbol # shows the signals that passed the nominal significance threshold (two-sided $P < 0.05$) but did not survive the correction. The exact sample sizes and *P* values of all analyses are included in Supplementary Files 13–15. In **m–o**, the shaded regions represent the 95% CI for the estimated PACC score. It is worth noting that this heterogeneity cannot be attributed to the drug itself, and the initial trials did not show that the drug had a significant benefit in delaying cognitive decline. For **a–e** and **g**, each shape represents the estimated HR for a given disease or mortality. The line extending from the dots or shapes shows the 95% CI for each HR. In the violin and box plots shown, the violin plot illustrates the full distribution of the data using kernel density estimation, with the width indicating data density at each value. Overlaid box plots display summary statistics. The center line represents the median; the bounds of the box correspond to the first and third quartiles; and whiskers extend to the most extreme values within 1.5× the interquartile range from the box.



Fibroblasts are directly involved in heart tissue maintenance and repair and may contribute indirectly to the inflammation and vascular changes associated with migraines. Endothelial cells are specialized cells that form the inner lining of blood vessels and lymphatic vessels, potentially supporting the endothelial hypothesis in migraine⁷⁶.

The clinical promise of the 11 MAEs for precision medicine

We show the clinical promise of the 11 MAEs in predicting various clinical outcomes through survival analysis and logistic regression: (1) the incident of DEs, (2) AD progression (CN to MCI to AD), (3) the risk of mortality, and (4) medication use status ('Prediction and association analyses for the risk of DEs, AD progression, mortality, history of medication use and preclinical AD drug effects' in Methods).

Using ICD-10-based DEs from UKBB, we showed that MAEs and their corresponding polygenic risk scores (PRSs) ('PRS calculation' in Methods) were significantly linked to the incident of chronic diseases, both specific to their respective organs and across different organ systems ('Survival analysis for the incidence of DEs' in Methods). For the brain MAE analyses (306 DEs tested), Brain 2 (hazard ratio (HR) = 1.09, 95% CI = (1.04, 1.13); $P = 3.37 \times 10^{-3}$), Brain 6 (HR = 1.08, 95% CI = (1.04, 1.12); $P = 8.97 \times 10^{-5}$) and the PRS derived from Brain 6 (Brain 6-PRS) (HR = 1.05, 95% CI = (1.01, 1.10); $P = 8.44 \times 10^{-3}$) were significantly associated with primary hypertension (ICD-10 code I10) (Fig. 6a). The 3 eye MAEs showed limited predictive power for the onset of the 415 DEs analyzed. Notably, the only eye-related disease examined was glaucoma (ICD-10 code H409), but the analysis had extremely imbalanced data, with only 12 cases compared with 674 non-cases. Finally, Heart 1 and Heart 2 were significantly linked to the incident of hypertension (I10; Fig. 6b), hypercholesterolemia (E780; Fig. 6c) and psychoactive substance abuse (Z864; Fig. 6d). Detailed statistics, including HRs, P values and sample sizes, are presented in Supplementary File 13.

Using the ADNI data, we showed the prediction power of the six brain MAEs for AD progression: CN to MCI to AD (Supplementary Table 9 and 'Survival analysis for AD progression' in Methods). We found that Brain 1 (HR = 1.33, 95% CI = (1.15, 1.54); $P = 1.40 \times 10^{-4}$), Brain 2 (HR = 1.38, 95% CI = (1.08, 1.75); $P = 9.35 \times 10^{-3}$) and Brain 3 (HR = 1.86, 95% CI = (1.41, 2.45); $P = 1.00 \times 10^{-5}$) were positively associated with the risk of MCI to AD progression, whereas Brain 5 showed a negative association (HR = 0.69, 95% CI = (0.62, 0.78); $P = 8.48 \times 10^{-10}$) (Fig. 6e). We then cumulatively added the most significant predictors on top of age and sex to evaluate their incremental power for MCI-AD progression, resulting in the highest concordance index (0.61 ± 0.03 in a 100 repeated holdout cross-validation) when combining age, sex, Brain 3, Brain 1, Brain 2 and Brain 5 (Fig. 6f).

We also used the 11 MAEs and their PRSs to predict mortality risk using UKBB data ('Survival analysis for mortality risk' in Methods). Our analysis revealed that Heart 1 (HR = 1.14, 95% CI = (1.06, 1.23); $P = 9.04 \times 10^{-4}$), Heart 2 (HR = 1.20, 95% CI = (1.12, 1.30); $P = 2.01 \times 10^{-7}$) and Heart 2-PRS (HR = 1.09, 95% CI = (1.01, 1.17); $P = 2.53 \times 10^{-2}$) showed a significant association with mortality risk; Brain 3 and Eye 2 showed a nominally significant relationship ($P < 0.05$) (Fig. 6g). Given the considerable associations from the heart MAEs, we performed a cumulative prediction analysis. However, only Heart 2 added additional power on top of age and sex, achieving an average concordance index of 0.73 ± 0.032 (Fig. 6h). Detailed statistics, including HRs, P values and sample sizes, are presented in Supplementary Table 10.

We predicted the medication status for the 4 drug categories (that is, antipsychotic medications, blood pressure medications, cholesterol-lowering medication and insulin) using the 11 MAEs and their PRSs from UKBB data, quantified by the incremental R^2 for additional variance explained by the respective MAE or PRS for the binary medication status ('Logistic regression for the pseudo incremental R^2 ' in Methods). We showed that Brain 3 was most predictive of antipsychotic medications (incremental $R^2 = 1.08\%$, $P = 4.87 \times 10^{-3}$, $N = 1,243$) (Fig. 6i). Eye 1, Eye 2 and Eye 3 were significant predictors of blood

pressure medication status (Fig. 6j). However, their contribution to the predictive model was relatively small, as indicated by a smaller incremental R^2 value (incremental $R^2 < 0.13\%$, $P < 2.2 \times 10^{-7}$; $N = 19,925$) compared with the more substantial impact of the heart MAEs (Fig. 6k). Detailed statistics, including P values and sample sizes, are presented in Supplementary File 14. For the 164 individual-level medication predictions, we found that the most significantly associated drug for the brain MAEs was achieved between Brain 6 and amlodipine (incremental $R^2 = 0.31\%$, $P \leq 9.03 \times 10^{-9}$, $N = 8,763$), used for blood pressure and cardiovascular disease treatment. The most significant drug association for the heart MAEs was identified with Heart 2 (incremental $R^2 = 30\%$, $P \leq 2.05 \times 10^{-19}$, $N = 4,811$), along with the Heart 2-PRS, but not Heart 1, and digoxin, a drug primarily used to treat heart failure (Fig. 6l and Supplementary Fig. 11). Finally, the most significant drug for MAEs of the eye was obtained between Eye 2 and tramadol to treat chronic pain. Detailed statistics, including P values and sample sizes, are presented in Supplementary File 15.

Given the elevated risks of progression from MCI to AD associated with Brain 1–3, we further explored their potential for patient stratification to improve clinical outcomes in an AD drug trial ('Natural cubic splines for modeling drug effects on the underexpressed, overexpressed patient groups in Brain 1–3 and the placebo group' in Methods). As illustrated in Fig. 6m–o, participants with underexpression levels (MAE below the median) of Brain 1–3 showed better cognitive performance than those with higher expression levels in each respective brain MAE. For example, Brain 2 showed the strongest differences on preclinical Alzheimer's cognitive composite (PACC) score between the underexpressed and overexpressed patient groups (t statistic = 3.519, $P = 0.004$). Detailed statistics are presented in Supplementary Table 11.

Discussion

In this study, we introduce 11 AI-derived biomarkers to understand disease heterogeneity through the concept of pan-disease, which bridges transdiagnostic insights⁷⁷ across multiple organ systems. Integrating AI with multi-omics and multi-organ biomedical data provides a holistic framework to model disease heterogeneity, further supporting the endophenotype hypothesis². The 11 MAEs complement traditional disease classification systems and offer a data-driven representation for stratifying individuals at higher risk for specific dimensions of neurobiological and etiologic factors. These MAEs enhance our understanding of disease biology by uncovering their distinct phenotypic, genetic and proteomic architectures. Importantly, they show differential predictive power for chronic disease incidents, mortality, AD progression and medication status, offering a dimensional tool for advancing personalized medicine and drug development strategies. Extended Data Fig. 5 summarizes the characteristics of the 11 MAEs.

Eleven MAEs capture reproducible and distinctive morphological changes for pan-disease of the brain, eye and heart

We identified 11 MAEs characterized by reproducible and distinct imaging patterns that complement and challenge traditional disease classification frameworks. These imaging patterns effectively differentiate individuals with morphological changes from those without pathologies.

The six brain MAEs encapsulate various neuroanatomical changes, with Brain 1–3 displaying distinct patterns of brain atrophy, while Brain 4–6 are associated with conserved brain structures, marked by larger brain volumes. Many neurodegenerative diseases were associated with brain atrophy, which could be attributable to the atrophy patterns observed in Brain 1–3. For example, AD was widely known for global atrophy with a focal hub in the medial temporal lobe⁷⁸ and hippocampus⁷⁹. Heterogeneity analysis has unraveled multiple disease subtypes, showing different atrophy patterns. For example, a study³ applied the SUSTAIN model and found three distinct subtypes and

trajectories of AD, which were termed typical, cortical and subcortical atrophy subtypes. Another study² applied a different AI method called Smile-GAN and identified four distinct AD subtypes: (1) preserved brain volume, shows no significant atrophy across the brain compared with healthy controls; (2) mild diffuse atrophy, with widespread mild cortical atrophy without pronounced medial temporal lobe atrophy; (3) focal medial temporal lobe atrophy, showing localized atrophy in the hippocampus and the anterior-medial temporal cortex with relative sparing elsewhere; and (4) global atrophy pattern. Beyond the neuroanatomical heterogeneity, ref. 32 also defined four distinct tau subtypes in AD, including limbic-predominant and medial temporal lobe-sparing patterns.

Global brain atrophy is less prominent in psychiatric disorders than in neurodegenerative diseases, although some conditions do show brain volume loss, particularly in severe or chronic cases. In a case-control setting, schizophrenia shows widespread atrophy, mainly in the prefrontal cortex, temporal lobes and hippocampus⁸⁰. Disease subtypes identified by AI further showed that a subset of patients with schizophrenia showed conserved brain volume. For example, ref. 35 applied the HYDRA model to define two subtypes of schizophrenia, with subtype 2 showing increased volume in the basal ganglia and internal capsule. This conserved brain volume subtype was corroborated by ref. 34 using an independent dataset, which identified a similar pattern of increased striatal volume in their defined subtype 1. The relatively conserved brain volume patterns observed in several psychiatric disorders, including late-life depression³³ and autism⁸¹, may be attributable to the imaging patterns observed in Brain 4–6. In addition, the ‘medicinal compensation effect’ concept with conserved brain volume in brain diseases may compensate for disease-induced damage through neuroplasticity or other adaptive mechanisms. This could be observed in specific subtypes or dimensions of brain diseases where, despite widespread atrophy, some brain regions (such as the striatum or hippocampus) maintain or increase their volume. For example, a recent study⁸² showed that AI-derived dimension 1 of major depressive disorder, characterized by preserved gray and white matter, showed a significant improvement in depressive symptoms following treatment with selective serotonin reuptake inhibitor medication (51.1%) but limited changes following placebo (28.6%).

The impact of normal aging on global brain atrophy, particularly in brain subtypes 1–3, is evident from the strong association with brain BAG (Fig. 3a). In a recent study¹⁰, we applied the Surreal-GAN model to a large and diverse population dataset ($N = 49,482$) with brain MRI data and identified 5 distinct patterns of age-related brain atrophy. Notably, one of these dimensions, referred to as R2, showed a pattern reminiscent of AD-related medial temporal lobe atrophy, underscoring the overlap between normal aging and pathological brain changes. Finally, the six brain MAEs may also capture morphological changes in the central nervous system beyond the brain, such as alterations in the spinal cord or peripheral neural pathways⁸³. These regions may show degeneration or structural adaptations linked to neurodegenerative diseases or systemic conditions affecting the central nervous system.

The three eye MAEs showed distinct morphological changes, with the most prominent macular thickness and optic disk thinning in Eye 2 (Fig. 1b), corroborated by the strongest genetic overlaps between Eye 2 and eye BAG (Fig. 4b). A pattern of macula thickness thinning and optic disc thinning is often associated with a variety of eye diseases, typically involving degenerative processes or damage to the retina and optic nerve, such as age-related macular degeneration⁸⁴. Eye 1 and Eye 3’s morphological patterns varied. For instance, Eye 1 showed a reduced macular thickness, whereas Eye 3 showed macular thickening (Fig. 1b). Both Eye 1 and Eye 3 were associated with different forms of glaucoma (Fig. 2b; ICD codes H400 and H401)⁸⁵, which typically manifests with retinal nerve fiber layer thinning; however, patients with certain eye

diseases showed increased macular thickness. Diseases like diabetic macular edema⁸⁶ can cause a thickening of the macula due to fluid accumulation, inflammation or abnormal blood vessel growth. This can be supported by the association between Eye 3 and non-insulin-dependent diabetes mellitus in our PWAS analyses (Fig. 2b; ICD code E119). Another unique feature of Eye 3 is the positive association of the left vertical cup-to-disc ratio (VcdrL: https://labs-laboratory.com/medicine/vertical_cup_to_disc_ratio_vcdr_left_f27857_0_0). Previous studies have found this association, most notably in glaucoma, where progressive damage to the optic nerve leads to an expansion of the optic cup relative to the optic disc. This indicates a loss of retinal ganglion cells and optic nerve fibers, resulting in the typical ‘cupping’ phenomenon seen in glaucoma⁸⁷.

The two heart MAEs also showed distinct morphological changes. Overall, Heart 1 was characterized by increased wall thickness of the LV (for example, WT_global: https://labs-laboratory.com/medicine/lv_mean_myocardial_wall_thickness_global_f24140_2_0), whereas Heart 2 showed increased volume of the LA and the stroke volume of the LA, and decreased ejection fraction volume of the LA, showing an opposite pattern to Heart 1. Many heart diseases, such as hypertension and aortic stenosis, cause the heart muscle, particularly the LV, to thicken (that is, LV hypertrophy) as it works harder to pump blood against increased resistance⁸⁸. The opposite direction of associations between Heart 1 and Heart 2 with metrics linked to the LA and RA, normally an indirect marker for the overall function and structure of the LV, may indicate distinct pathological factors related to the two dimensions. For example, a decreased ejection fraction is indicative of impaired left ventricular systolic function and is a hallmark of several heart conditions, including heart failure and myocardial infarction⁸⁹.

Our AI models analyzed the heterogeneous morphological changes of pan-disease affecting the 3 organs, identifying potentially distinct pathological and etiological processes associated with the 11 MAEs. This enabled a digitized, dimensional system to prioritize individuals with specific morphological changes.

Opposite to Brain 5, Brain 1–3 serves as a risk dimension for AD progression, mortality, antipsychotic medications and solanezumab

Brain 3 is characterized as a risk dimension associated with AD progression (MCI to AD), mortality and antipsychotic medication use. The global atrophy pattern of the brain is likely tied to neuroanatomical changes that predispose individuals to more severe cognitive decline⁹⁰, higher mortality risk and a greater need for antipsychotic interventions. Global cortical atrophy and hippocampus atrophy have been prominent biomarkers for MCI and AD. For example, ref. 90 used longitudinal data to show that hippocampal atrophy rates in individuals with MCI accelerate by 0.22% per year² on average. In our PWAS, the brain pattern of structural covariance (PSC) (‘PSCs of the brain’ in Methods; data-driven structural covariance network for C128_3: <https://www.cbica.upenn.edu/bridgeport/MUSE/Left%20Hippocampus>) spatially linked to the left hippocampus was significantly associated with Brain 3 ($\beta = -0.077, P = 1.89 \times 10^{-39}$). The high relevance of AD with Brain 3 was further strengthened by the link with the CSF t-tau_{18p} (Extended Data Fig. 1d). Another study⁹¹ revealed that decreased survival was linked to atrophy in the temporal and frontal lobes, and widening of the Sylvian fissure and several ventricular measurements. Finally, various psychiatric disorders show shared global atrophy patterns⁹², suggesting that patients predominantly characterized by Brain 3 may have a more favorable response in future clinical trials and drug development. Crucially, in the initial clinical trial⁴¹, the authors reported that no significant drug effect was achieved between the placebo and treatment groups for solanezumab. Our brain MAEs, particularly Brain 2, showed the effectiveness of AI-driven population stratification, dividing treatment groups into two distinct subpopulations with potentially divergent cognitive decline trajectories (Fig. 6m–o). This insight is

pivotal for future AD clinical trials, as these subgroups may represent different underlying disease mechanisms⁹³, underscoring the need for personalized treatment strategies.

In contrast, Brain 5, characterized by conserved brain volume, may indicate a protective dimension for these risks. Brain 5 showed an HR of 0.69 (95% CI = (0.62, 0.78)) for MCI–AD progression, indicating lower conversion risks (Fig. 6e). However, such a protective association was not observed for the CN–MCI progression. Several factors may explain this pattern. First, our brain MAEs were modeled using Surreal-GAN based on ICD-10 codes derived from hospital inpatient records and other resources, which may reflect a later stage in the progression of brain pan-disease. Consequently, these brain MAEs are less sensitive to early neurobiological changes within the AD continuum. Second, various compensatory mechanisms might also be at play. In the initial stages of neurodegenerative diseases like AD, the brain may show compensatory responses, leading to increased volume due to factors such as edema or neuroinflammation. In individuals with MCI, this increased volume can obscure underlying atrophy. However, as the disease advances, these compensatory effects wane, and brain atrophy becomes more pronounced, resulting in negative correlations with cognitive decline⁹⁴. Similarly, the protective role of Brain 5 for AD was also supported by the positive association between Brain 5 and $A\beta_{1-42}$ (Extended Data Fig. 1d), further corroborating a protective or compensatory response in the face of emerging pathology for Brain 5.

Their underlying genetic architectures can also further elucidate the contrast profiles between Brain 3 and Brain 5, showing stark differences in purifying selection signatures and pyrogenicity (Fig. 4c,d). The stronger negative purifying selection signature observed in Brain 5 compared with Brain 3, along with Brain 5's stronger polygenicity, can be attributed to several factors related to evolutionary dynamics, genetic architecture and the functional significance of the associated traits. First, Brain 5 may be associated with traits under strong evolutionary pressure to maintain function, resulting in more pronounced negative purifying selection. This type of selection removes deleterious alleles from the population, thus preserving critical functions (for example, conserved brain volume). In contrast, Brain 3 may be less functionally constrained, allowing for a higher tolerance of genetic variation. The negative selection signature is common in complex human traits, as evidenced in a study⁹⁵ on SBayesS. In contrast, the increased polygenic nature in Brain 5 may also indicate a higher genetic load⁹⁶, where multiple alleles contribute cumulatively to brain function. This complexity can lead to a more robust system that is still subject to the constraints of purifying selection, ensuring that only advantageous variants are retained. To summarize, the distinct evolutionary pressures and genetic architectures of Brain 5 and Brain 3 may also influence their susceptibility to neurodegenerative diseases. The stronger purifying selection in Brain 5 could indicate a protective mechanism that mitigates risks associated with pathological conditions, while the increased polygenicity could make Brain 5 more adaptable to environmental or genetic changes over time.

Brain 1 identifies the *FLRT2* gene as a new druggable target for migraine treatment

We identified a multilayer causal pathway prioritizing the *FLRT2* gene as a new druggable target for migraine treatment (Fig. 5e). Migraine is a common brain disorder with a large genetic component; the *FLRT2* gene is not considered to be associated with migraines⁹⁷, although it does have implications in postnatal central nervous system development⁹⁸, ischemic stroke⁹⁹ and bipolar disorder¹⁰⁰.

By contrast, our findings show that *FLRT2* does influence migraine disorders through its effects on brain morphology (Brain 1), specifically through the atrophy in the temporal and frontal lobes and the inferior cerebellum. This has strong clinical implications. In particular, this causal association suggests that individuals carrying specific variants

of the *FLRT2* gene (for example, these single SNPs in Extended Data Fig. 4b) may be at a higher risk for developing migraines, indicating a potential biomarker for early identification and risk assessment. Furthermore, the role of *FLRT2* in neuronal development points to its potential as a therapeutic target; interventions aimed at modulating *FLRT2* pathways may offer new treatment options. The connection between structural brain changes and migraine pathophysiology highlights the importance of understanding how genetic factors contribute to the development of migraines. Integrating genetic and proteomic information with neuroimaging data could refine diagnostic criteria and therapeutic strategies, paving the way for personalized medicine approaches in migraine management. This comprehensive approach emphasizes the important role of multi-omics data in driving new drug and therapeutic discoveries. For instance, a recent study¹⁰¹ showed the use of spatial proteomics to uncover a new treatment for toxic epidermal necrolysis, illustrating how integrating multi-omics insights can open promising avenues for clinical translation.

Identifying the *cis*- and *trans*-pQTL, on top of the eQTL, for *FLRT2* provides direct evidence of genetic variation that modulates the levels or function of this protein, linking specific genetic loci to physiological changes in protein expression and, subsequently, to clinical outcomes¹⁰². Specifically, this suggests that genetic variations alter the risk of brain atrophy and migraine and affect how much or how efficiently the *FLRT2* protein is produced or functions in brain tissue. This enhances our understanding of the causal pathway from gene to disease, as it shows that genetic differences at the *FLRT2* locus lead to quantifiable changes in the protein that may drive or exacerbate the brain atrophy observed in Brain 1. This causal pathway also offers empirical support for the mediational model of the endophenotype hypothesis²⁸, highlighting Brain 1 as a promising biomarker for guiding drug development efforts to treat related disorders.

Eye 1 and Eye 3 show implications for a close eye–cancer relationship

Our results highlight crucial connections between different cancer types and Eye 1 and Eye 3. This highlights the systemic effects of cancer and can be used to leverage eye morphology as a potential biomarker for early cancer detection and monitoring.

The eye morphological changes in Eye 1 and Eye 3 have implications in cancer, suggesting that alterations in structures such as the macula or optic disc may reflect ocular health and serve as biomarkers for cancer. For example, Eye 1 and malignant neoplasm of the corpus uteri (ICD code C541) showed a positive association ($\beta = 0.059 \pm 0.0016$, $P = 7.61 \times 10^{-8}$; Fig. 3b). Our findings highlight potential drug repurposing opportunities for Eye 1 and Eye 3, particularly in the context of cancer therapies. The associations between these eye-derived morphological features and malignant neoplasms, supported by gene–drug–disease network analyses (Fig. 4e) and causal links to key proteins (Fig. 5d), suggest that eye endophenotypes might be early indicators of oncogenic processes. This relationship opens new avenues for exploring eye health as part of a multi-organ approach to detecting and managing cancer. The underlying hypothesis is that shared molecular and genetic pathways could be at play, influencing both eye morphology and cancer susceptibility, especially in aging. First, metastatic cancer, such as melanoma or breast cancer, can spread to the eye, affecting structures like the retina, choroid or optic nerve, leading to changes such as thickening, swelling or tissue atrophy^{103,104}. Paraneoplastic syndromes, particularly cancer-associated retinopathy¹⁰⁵, are another factor, where the immune system's response to systemic cancer attacks retinal cells, causing ocular changes. In addition, treatments for cancer, including chemotherapy and radiation, can result in complications such as macular edema, optic neuropathy and retinal degeneration, altering the eye's structural morphology¹⁰⁶. Moreover, genetic links are also emerging, where mutations in genes involved in both cancer and eye health, such as

those controlling retinal development, suggest a molecular connection between eye changes and cancer progression. Finally, these connections may be more likely correlational; potential mechanisms could involve paraneoplastic syndromes, which reflect remote effects of tumors on the eye, or shared microvascular and metabolic pathways that influence both ocular and cancer pathophysiology.

Future research should delve deeper into these connections, investigating how specific eye endophenotypes could be used in cancer risk stratification, monitoring disease progression, and potentially guiding therapeutic interventions, thereby broadening the scope of precision medicine in aging and oncology.

Heart 1 and Heart 2 are two monitorable dimensions for mortality and various cardiovascular conditions

We identified Heart 1 and Heart 2 as distinct dimensions associated with predicting mortality, multiple cardiovascular conditions and related medication use. These findings suggest that these dimensions could be instrumental in patient stratification, potentially guiding future drug development efforts to target specific cardiovascular conditions and optimize treatment strategies.

The two heart MAEs showed the highest reproducible patterns (Fig. 1e) compared with the other organs, offering strong evidence that two distinct dimensions exist in heart pan-disease. In particular, Heart 2 and Heart 1 showed higher HR estimates for predicting mortality than the other two organs. Cardiovascular diseases remain the leading cause of death globally¹⁰⁷. As a result, heart-related MAEs are more likely to be associated with higher HR for mortality and adverse events than those associated with neurodegenerative or ophthalmic diseases. Heart 1 and Heart 2 likely capture systemic cardiovascular changes affecting the entire body, including the brain and eyes. In contrast, the brain and eye MAEs may represent more localized damage that, although severe, may not have the same broad systemic effects as heart conditions. Furthermore, while the brain and eye MAEs are crucial for cognitive and sensory functions, cardiovascular conditions can lead to multi-organ failure¹⁰⁸ through mechanisms such as reduced blood flow, increased inflammation and oxygen deprivation. This widespread impact could result in more severe clinical outcomes, reflected in higher HRs for heart conditions. From a genetic standpoint, weaker purifying selection signatures of Heart 1 and Heart 2, especially compared with Eye 1 and Eye 3 (Fig. 4c), can result in higher genetic variability in heart MAEs. This could lead to more polygenic architectures where many genetic variants with small effects collectively contribute to the phenotypic presentation of heart diseases^{109–111} (Fig. 4d). The higher HRs observed for Heart 1 and Heart 2 compared with brain and eye MAEs might reflect this polygenic nature, and the complex interaction of environmental, lifestyle and genetic factors in heart disease development.

The distinct clinical implications of the two heart MAEs suggest differential risk profiles for cardiovascular health and drug response (Fig. 6). Heart 1, which is more strongly associated with hypertension, hypercholesterolemia and antihypertensive medications, aligns with traditional cardiovascular risk factors. This suggests that individuals dominated by the Heart 1 MAE may be more predisposed to metabolic and vascular abnormalities, likely benefiting from interventions targeting cholesterol levels and blood pressure management¹¹². In contrast, Heart 2, which is predictive of psychoactive substance use and the use of digoxin (critically not Heart 1) for heart failure treatment (incremental $R^2 = 30\%, P \leq 2.05 \times 10^{-19}, N = 4,811$; Fig. 6l and Supplementary Fig. 11) highlights a different risk dimension. The link with psychoactive substance use could reflect the broader role of lifestyle and substance exposure in cardiovascular health^{113,114}. Clinically, this distinction between the two heart MAEs provides insight into personalized therapeutic approaches, where Heart 1 patients may respond better to antihypertensive and lipid-lowering therapies, whereas Heart 2 patients might benefit from treatments addressing heart failure and

lifestyle factors contributing to substance abuse. This highlights the potential for stratifying cardiovascular patients based on their MAE profile for targeted interventions and precision medicine¹¹⁵.

No organ system is an island

In addition to introducing the concept of pan-disease to explore disease heterogeneity, our study enhances multi-organ research by incorporating advanced AI techniques to provide a dimensional framework for more precise patient stratification and management.

Previous multi-organ research initially focused on linking IDPs across multiple organ systems. For example, we introduced a new data-driven brain IDP–PSCs²³—and established a brain–eye–heart axis¹⁶. Reference 116 established a brain–heart–liver axis using MRI data from these organs using UKBB imaging data. Reference 117 also integrated genetics with 11 organ traits from abdominal MRI. Later studies focused on deriving individual-level imaging signatures across organ systems via AI. For instance, ref. 19 developed multi-organ BAGs from 9 organ systems, linking them to clinical traits, while ref. 17 expanded this by investigating the genetic architecture of these BAGs. More recently, multi-organ BAGs were also derived from proteomics data, further being linked to disease outcomes using UKBB data¹¹⁸. In addition, the brain–gut axis¹¹⁹ may be another data layer to human aging and disease, and future investigations, especially leveraging emerging microbiome data in the UKBB, could expand this work to incorporate gut-related mechanisms.

Our multi-organ MAEs offer a complementary and clinically focused advancement over BAGs^{13,14,17,18,20,22}. While BAGs summarize the deviation between biological and chronological age and are useful for capturing global aging processes, they are inherently broad, often reflecting the cumulative effects of diverse and overlapping biological pathways. In contrast, MAEs are designed to be disease-specific, data-driven imaging biomarkers that encapsulate organ-level morphological variations more directly tied to individual disease processes. Clinically, this distinction translates to greater specificity. MAEs are more interpretable in the context of particular diseases (for example, AD, cardiomyopathies or ocular degeneration), enabling more precise risk stratification and potentially informing targeted interventions. MAEs also improve cross-organ resolution by separately modeling each organ's structural alterations, rather than aggregating them into a single index as BAGs do. This organ-level granularity can reveal distinct morphometric signatures and interactions between organs that are missed by aging clocks. As such, we envision that aging clocks and disease-specific MAEs are integrated within a unified digital twin framework: BAGs provide a broad systemic health profile, while MAEs supply fine-grained, organ-targeted insights to support more personalized and effective clinical decision-making.

Limitations and outlook

Our study has several limitations. First, our analyses primarily focus on European populations, and we should carefully evaluate the generalizability of our GWAS findings to non-European groups. Future methodological advances are needed to extend the Surreal-GAN model to non-European populations to overcome this potential bias and ensure model fairness. Second, while we have evaluated the expression of the six brain MAEs in independent external datasets, further studies are needed to validate the heart and eye MAEs. We anticipate that future research will explore multi-organ, multi-omics approaches, providing more comprehensive models for studying human aging and disease. This direction promises to unlock deeper insights and refine our patient care and therapeutic development strategies across diverse health conditions. Future work could also focus on developing fully data-driven disease subtypes across multiple organ systems by leveraging shared populations with multi-organ data. This approach may uncover new, system-level disease mechanisms and enable more precise cross-organ phenotyping.

Methods

The MULTI consortium

The MULTI consortium is an ongoing initiative to integrate and consolidate multi-organ data, such as brain and heart MRI and eye OCT, with multi-omics data, including imaging, genetics and proteomics. Building on existing consortia and studies, such as those listed below, MULTI aims to curate and harmonize the data to model human aging and disease across the lifespan. In this study, in total, individual-level data for 129,340 participants were analyzed, including 81,831 for multi-organ imaging data (brain and heart MRI and eye OCT), 83,322 for genetic data (imputed genotype and whole genome sequencing (WGS)), and 53,940 for plasma proteomics data (Olink and SomaScan). GWAS summary statistics from FinnGen and PGC were downloaded and harmonized for our post-GWAS analyses. A subset of the population also had cognitive data and neuropathological biomarkers for AD, including $A\beta_{1-42}$ and tau_{181p} from CSF and plasma. RNA-seq and additional protein data were also curated and made available through the Human Protein Atlas (HPA) and STRING platforms. Refer to Supplementary Table 1 for comprehensive information, including the complete list of data analyzed and their respective sample characteristics. Participants provided written informed consent to the corresponding studies. The MULTI consortium is approved by the Institutional Review Board at Columbia University (AAAV6751).

UKBB. UKBB¹²⁰ is a population-based research initiative comprising around 500,000 individuals from the United Kingdom between 2006 and 2010. Ethical approval for the UKBB study has been secured, and information about the ethics committee can be found here: <https://www.ukbiobank.ac.uk/learn-more-about-uk-biobank/governance/ethics-advisory-committee>.

This study collectively analyzed multi-organ imaging data, including 42,660 brain T1-weighted MRI scans (referred to as the brain population), 35,576 heart MRI scans (representing the heart populations) and 40,063 eye OCT images (the eye populations) at baseline, under application numbers 35148 and 60698. The combined sample size across the three organ populations totaled 81,831. The T1-weighted MRI data underwent processing at the University of Pennsylvania for the brain PSCs, denoting data-driven structural network measurements via the MuSIC atlas and the iSTAGING consortium²³. To train the Surreal-GAN model, we used the scale ($C = 128$ for the 128 structural networks) brain PSCs, comparable to the number of heart and eye IDPs, detailed later. The 82 heart IDPs were downloaded directly from the UKBB website and derived from a previous study²⁴ (category ID 157). We included heart IDPs with more than 35,000 participants, resulting in 80 heart IDPs to train the Surreal-GAN model. The 84 eye IDPs, derived from OCT imaging, were directly downloaded from our previous studies^{25–27} via the UKBB Eye and Vision Consortium (category ID 100016; return ID 1875). Similarly, we constrained the eye IDPs with more than 20,000 participants, resulting in 64 eye IDPs in the Surreal-GAN model.

For the genetic data, we conducted a quality check on the imputed genotype data¹²⁰ for the entire UKBB population (approximately ~500,000 individuals). Subsequently, we merged the processed data with the brain, eye and heart population for all genetic analyses ($N = 81,831$). Refer to 'Genetic analyses' for details. Our primary focus was on populations of European ancestry, with non-European ancestry populations included in sensitivity check analyses. The preprocessing for the proteomics data is detailed later.

Finally, we also included the Olink proteomics data released by the UKBB Pharma Proteomics Project (UKB-PPP). The original data included 2,923 Olink plasma proteins for 53,016 participants. Details of the quality check procedure are presented in 'Proteomic analyses'. In total, multi-omics data from 125,406 UKBB participants were analyzed in this study after quality checks.

BLSA. The main goal of the BLSA is to understand the normal aging process. Tracking physiological and cognitive changes over time aims to identify risk factors for age-related diseases, study patterns of decline and discover predictors of healthy aging. BLSA^{39,40} brain MRI and proteomics data (<https://www.blسا.nih.gov/>) were used to replicate the brain ProWAS results from the UKBB study. After quality checks in this study, we included 1,114 brain MRI scans at baseline and measurements of 7,268 plasma proteins from 924 participants quantified with the SomaScan v.4.1 platform. Age (years), sex (male or female), race (white or non-white) and education level (years) were defined based on participant self-reports.

A4. The A4 study^{41,42} (<https://atri.usc.edu/study/a4-study/>) is a clinical trial study to test a specific way to prevent memory loss associated with AD (clinical trial number NCT02008357). The A4 study focused on symptom-free adults at higher risk for AD to assess whether an investigational drug (that is, solanezumab) could slow memory decline linked to amyloid plaques in the brain. It also examined whether solanezumab could delay AD progression, measuring related brain changes using imaging, blood biomarkers and baseline PET scans to assess amyloid levels. This study analyzed 1,055 participants at baseline with brain MRI scans to derive the 6 brain MAEs. Longitudinal outcomes from the clinical trial, with the PACC score as the primary measure over 312 weeks, were included. Specifically, there were 516 participants with 5,161 longitudinal PACC measures in the treatment group and 591 participants with 5,469 longitudinal PACC measures in the placebo group. The drug's effect between groups (for example, overexpressed versus placebo) was evaluated at week 240.

ADNI. ADNI (<https://adni.loni.usc.edu/>) includes patients from different stages of the disease progression: cognitively normal individuals (CN), those with MCI and those with AD. This allows researchers to compare brain structure and function changes across the AD continuum. We included baseline brain MRI data of 1,765 individuals, 9,752 longitudinal follow-up scans (>5 scans for longitudinal analyses used in this study) and 1,491 WGS data to generalize the GWAS signals from the UKBB data.

FinnGen. The FinnGen¹²¹ study is a large-scale genomics initiative that has analyzed over 500,000 Finnish biobank samples and correlated genetic variation with health data to understand disease mechanisms and predispositions. The project is a collaboration between research organizations and biobanks within Finland and international industry partners. For the benefit of research, FinnGen generously made their GWAS findings accessible to the wider scientific community (https://www.finngen.fi/en/access_results). This research used the publicly released GWAS summary statistics (version R9), which became available on May 11, 2022, after harmonization by the consortium. No individual data were used in this study.

FinnGen published the R9 version of GWAS summary statistics via REGENIE software (v.2.2.4)¹²², covering 2,272 DEs, including 2,269 binary traits and 3 quantitative traits. The GWAS model encompassed covariates like age, sex, the initial ten genetic principal components and the genotyping batch. Genotype imputation was referenced on the population-specific SISu v.4.0 panel. We included GWAS summary statistics for 521 FinnGen DEs in our analyses.

PGC. PGC¹²³ is an international collaboration of researchers studying the genetic basis of psychiatric disorders. PGC aims to identify and understand the genetic factors contributing to various psychiatric disorders, such as schizophrenia, bipolar disorder, major depressive disorder and others. The GWAS summary statistics were acquired from the PGC website (<https://pgc.unc.edu/for-researchers/download-results/>), underwent quality checks and were harmonized to ensure seamless integration into our analysis. No individual data were used from PGC. Each study detailed its specific GWAS models and methodologies, and

the consortium consolidated the release of GWAS summary statistics derived from individual studies. In this study, we included summary data for four brain diseases for which allele frequencies were present.

Multi-organ imaging features used to derive the MAEs via Surreal-GAN

PSCs of the brain. Our earlier work²³ applied the stochastic orthogonally-projective non-negative matrix factorization (sopNMF) method to a large-scale cohort of brain MRIs ($N=50,699$). This resulted in 2,003 multiscale brain PSCs, wherein the scale C ranged from 32 to 1,024, expanding exponentially by a factor of 2. To train the Surreal-GAN model, we used the 128 brain PSCs from the scale of $C=128$.

PSCs represent data-driven structural networks that encapsulate coordinated neuroanatomical changes in brain morphology stemming from a mixture of normal aging, pathology and unmodeled factors, such as environmental and genetic influences. Mathematically, the sopNMF algorithm is a deep learning-like stochastic approximation constructed and extended based on opNMF^{124,125}. Consider a dataset comprising n MR images, each containing d voxels. The imaging data are represented as a matrix X , where each column corresponds to a flattened image $X = [x_1, x_2, \dots, x_n]$, $X \in \mathbb{R}_{\geq 0}^{d \times n}$. The sopNMF algorithm factorizes X into two low-rank matrixes $W \in \mathbb{R}_{\geq 0}^{d \times r}$ and $H \in \mathbb{R}_{\geq 0}^{r \times n}$, subject to the constraints of (1) non-negativity, and (2) column-wise orthonormality. More mathematical details are presented in Supplementary Method 2 and the original refs. ^{23,124,125} (Supplementary Table 12).

IDPs of the heart. The 82 heart IDPs were directly downloaded from the UKBB website (category ID 157). Reference 24 used a deep learning-based pipeline for analyzing UKBB cardiac and aortic MR images, and derived a broad spectrum of structural and functional phenotypes for the heart and aorta. The study investigated the correlations of these heart IDPs with factors such as sex, age, critical cardiovascular risk elements and other non-imaging traits. For the 80 heart IDPs (after quality checks) included in our analyses, we further categorized them into 6 different IDP groups for visualization purposes, as shown in Supplementary Table 12.

IDPs of the eye. For the 88 eye IDPs, we used the derived OCT measurements from our previous studies^{25–27} (category ID 100079) and used the imaging quality scores (Field IDs 28552 and 28553) for quality check. We excluded 12,044 individuals whose scores were lower than 45 (category ID 100116).

OCT imaging is an advanced, non-invasive technology that generates three-dimensional images of the macula, crucial for detailed central vision. Abnormalities in macular thickness and morphology captured by OCT imaging are sensitive biomarkers of diabetic retinopathy, age-related macular degeneration, glaucoma and various neurodegenerative diseases^{126,127}. Our previous studies^{25–27} processed the OCT images to derive the 84 eye IDPs used in our analyses, and the results were subsequently returned to UKBB, making them accessible to the community. Studies^{26,25} conducted by members of the UKBB Eyes and Vision Consortium (<https://www.ukbiobankeyeconsortium.org.uk/>; category ID 100016; return ID 1875) analyzed OCT images from over 60,000 individuals in the UKBB. They derived variables related to the thickness of the retinal pigment epithelium (excluding outliers and individuals with diseases affecting macular thickness). A subsequent investigation²⁷ extracted optic nerve head morphology measures and performed a GWAS on these additional eye IDPs. For the 64 eye IDPs (after quality checks) included in our analyses, we further categorized them into 11 different IDP groups for visualization purposes (Supplementary Table 12).

Surreal-GAN methodological considerations

Reference and target population definition. We used a weakly supervised deep representation learning approach called Surreal-GAN¹⁰ to

derive the 11 MAEs. Unlike traditional unsupervised clustering methods, which directly analyze the patient population, weakly supervised techniques seek the ‘1-to- k mapping’ between the reference domain (CN) and the target domain (pan-disease PT)⁸. This approach effectively captures disease progression along the causal pathway and mitigates confounding factors (for example, age, sex or head size) unrelated to neurobiology and etiology.

In each organ-specific population, we defined the CN and PT populations for the Surreal-GAN model training using multiple resources from UKBB (Fig. 1a). For CN, we excluded participants with any ICD codes from hospital inpatient records (category ID 2002), any medical conditions recorded in their health and medical history (category identifier 100044) and certain mental health conditions (for example, category ID 100060). For PT for the brain pan-disease, we used the ICD-10 codes G (diseases of the nervous system) and F (mental and behavioral disorders) to define the brain pan-disease population. For PT for the eye pan-disease, we used the ICD-10 codes H0–H5 (diseases of the eye and adnexa) to define the eye pan-disease patient population. For PT for the heart pan-disease, we used the ICD-10 code I (diseases of the circulatory system) to define the heart pan-disease patient population.

After defining these populations, we merged them with the organ-specific imaging populations (Supplementary Table 1) to train the three Surreal-GAN models.

We used a grid search to select the optimal hyperparameters of the Surreal-GAN model. Specifically, k represents the number of pre-defined dimensions of pan-disease of each organ; λ represents the regularization term for controlling the orthogonality loss that boosts the separation of captured disease patterns in these dimensions; and γ represents the regularization term for controlling the change loss that encourages sparsity and distance of transformations.

Methodological advances in Surreal-GAN. The Surreal-GAN used in this study has substantial methodological improvements compared with its ‘beta’ version proposed in ref. 9. The original Surreal-GAN mode assumes that the k reproducibility (R) indices (that is, the MAEs here) are independent, which limits its ability to characterize morphological patterns driven by associated underlying pathologies. If we sample the latent variable z , indicating the transformation directions (that is, 1-to- k mapping), from a standard multivariate uniform distribution as in the original Surreal-GAN, the covariance of the derived R -indices will be the identity matrix, which leads to bias and decreased model performance when the ground-truth R -indices are correlated with each other. In a follow-up study¹⁰, we proposed a new version of Surreal-GAN to overcome this limitation, which constructed a parametrized latent distribution for z using a Gaussian copula, where the learnable parameters θ_z govern the correlations among the k dimensions. Supplementary Method 3 details the methodological considerations and advances for the Surreal-GAN model. Supplementary Fig. 14 shows the distribution of the 11 MAEs among different ethnic groups. Supplementary Fig. 15 shows the convergence of the 3 models.

Phenotypic analysis

PWAS. We performed different sets of primary PWAS that correlated the 11 MAEs with several sets of phenotypes to validate the derived MAEs: (1) the 9 multi-organ BAGs derived by our previous study¹⁷, (2) ICD-10-based DEs from UKBB, (3) CSF and plasma neuropathological biomarkers of AD from the ADNI and UKBB data, and (4) the 8 cognitive scores from UKBB.

We used a linear regression model for the multi-organ BAG PWAS using UKBB, with each MAE as the dependent variable and the BAG as the independent variable, adjusting for various covariates. For the DE PWAS, we used a logistic regression model, with the DE as the dependent variable and the MAE as an independent variable, adjusting for the same set of covariates. We included common covariates (for example, age and sex) and organ-specific covariates in these analyses.

We included covariates for the CSF or plasma neuropathological biomarker (for example, tau₁₈₁ and Aβ₁₋₄₂), PWAS and cognitive PWAS using data from UKBB and ADNI based on their availability in each dataset. For ADNI CSF PWAS, we included the AD diagnosis as an additional covariate in the linear regression model.

For the PWAS related to the brain MAEs in UKBB, we accounted for various covariates, including age (Field ID 21003), sex (Field ID 31), brain positioning in the scanner (lateral, transverse and longitudinal; Field IDs 25756–25758), head motion (Field ID 25741), intracranial volume, body weight (Field ID 21002), height (Field ID 50), waist circumference (Field ID 48), body mass index (BMI) (Field ID 23104), assessment center (Field ID 54), along with the first 40 genetic principal components. For the PWAS of the eye MAEs, we controlled for age (Field ID 21003 at the eye assessment session), sex (Field ID 31), body weight (Field ID 21002), height (Field ID 50), waist circumference (Field ID 48) and first 40 genetic principal components as covariates. For the PWAS related to the heart MAEs, we included covariates for age (Field ID 21003), sex (Field ID 31), body weight (Field ID 21002), assessment center (Field ID 54), height (Field ID 50), waist circumference (Field ID 48), smoking status (Field ID 20116), diastolic blood pressure (Field ID 4079), systolic blood pressure (Field ID 4080), assessment center (Field ID 54), BMI (Field ID 23104) and the first 40 genetic principal components.

Secondary PWAS. A secondary PWAS was conducted to link the 11 MAEs with the other 117 phenotypes accessible in our downloaded UKBB data. The same linear regression model mentioned earlier was used. We explicitly excluded the brain, eye and heart IDPs available at UKBB from this PWAS to prevent circular bias with our MAEs¹²⁸.

Proteomic analyses

We downloaded the original data (category code 1838), which was analyzed and made available to the community by the UKB-PPP¹²⁹. The initial quality check was detailed in the original work³¹; we performed additional quality check steps as below. We focused our analysis on the first instance of the proteomics data (instance = 0). Subsequently, we merged the Olink files containing coding information, batch numbers, assay details and limit of detection (LOD) data (category ID 1839) to match the ID of the proteomics dataset. We eliminated Normalized Protein eXpression (NPX) values below the protein-specific LOD. Furthermore, we restricted our analysis to proteins with sample sizes exceeding 10,000. We used the quality-checked proteomic data for three sets of analyses in this study: (1) ProWAS, (2) ProGWAS, and (3) Mendelian randomization (see ‘Genetic analyses’).

ProWAS. We performed ProWAS by linking the 11 MAEs to 2,923 unique plasma proteins from 53,016 participants (10,018 < N < 39,489 per protein after quality check) using the Olink platform.

For the brain ProWAS, we accounted for various covariates, including age (Field ID 21003), sex (Field ID 31), brain positioning in the scanner (lateral, transverse and longitudinal; Field IDs 25756–25758), head motion (Field ID 25741), intracranial volume, body weight (Field ID 21002), height (Field ID 50), waist circumference (Field ID 48), BMI (Field ID 23104), assessment center (Field ID 54), protein batch number (category ID 1839), LOD (category ID 1839) and first 40 genetic principal components. For the eye ProWAS, we controlled for age (Field ID 21003 for eye assessment instance), sex (Field ID 31), body weight (Field ID 21002 for eye assessment), height (Field ID 50 for eye assessment), waist circumference (Field ID 48 for eye assessment), protein batch number (category ID 1839), LOD (category ID 1839) and first 40 genetic principal components as covariates. For the heart ProWAS, we included covariates for age (Field ID 21003), sex (Field ID 31), body weight (Field ID 21002), height (Field ID 50), waist circumference (Field ID 48), smoking status (Field ID 20116), diastolic blood pressure (Field ID 4079), systolic blood pressure (Field ID 4080), assessment center (Field ID 54), BMI (Field ID 23104), protein batch number

(category ID 1839), LOD (category ID 1839) and the first 40 genetic principal components. Multiple comparisons were performed using Bonferroni corrections based on the number of proteins and MAEs. We also used the time interval as an alternative covariate in the model for image data from organs that were not collected at the same visit as the proteomics data. The ProWAS signals using UKBB Olink data were then compared with SomaScan data collected from BLSA.

Tissue- or organ-specific map of the expression of the human proteome. We annotated the tissue- or organ-specific expression patterns of significant proteins using the HPA (<https://www.proteinatlas.org/>)¹³⁰ platform (v.23). HPA curated the RNA and protein data from multiple sources, including the GTEx¹³¹ and FANTOM5¹³² datasets, to comprehensively assess tissue and/or single-cell (81 cell types from 31 datasets) expression profiles for a full set of human proteins. The protein data encompasses 15,303 genes for which antibodies are available. The RNA expression data are obtained from deep RNA-seq, including at single-cell resolutions, across different tissue types. The methodology for determining the expression of the protein is detailed in the original publication¹³⁰. In addition, HPA also performed cross-species analysis for the brain RNA expression using resources from different sources, such as the HPA pig brain and mouse RNA-seq data, GTEx human brain RNA-seq data and FANTOM5 human brain cap analysis of gene expression (CAGE) data. Importantly, proteins are often simultaneously overexpressed in various tissues or organs (that is, lack of organ specificity). Our main objective was to determine if the tested protein showed overexpression in the brain, eye and heart. If it was not overexpressed in any of these three organs, we highlighted its expression in other tissues with the highest evidence of overexpression.

ProGWAS. We also performed large-scale ProGWAS to link the 2,923 proteins to common SNPs. Refer to the section ‘GWAS’ for genetic quality check pipelines and the GWAS model used. This analysis was guided by a previous study⁷² and was meant to use the derived GWAS summary data in our multilayer Mendelian randomization analysis (see the section ‘PRS calculation’). To validate the ProGWAS results in our study, we demonstrated this by comparing our results using FLRT2 protein with those of ref. 72 (Supplementary Note 7 and Supplementary Fig. 9), showing a high degree of consistency.

PPI network analysis. Using OmicVerse¹³³ and the STRING database¹³⁴, we performed protein–protein function and interaction inference, including direct physical binding and indirect interactions such as shared biological pathways or cellular processes. STRING¹³⁵ (v.12.0) provides streamlined access to a comprehensive, quality-controlled database of protein–protein associations across various organisms (*Homo sapiens* in our analyses). Functional enrichments in the identified PPI network were performed regarding gene sets defined from different resources, including GO terms, the KEGG pathway and so on.

Genetic analyses

We used the imputed genotype data for all genetic analyses. Our quality check pipeline resulted in 33,570 participants for the brain population, 30,260 for the heart population and 36,659 for the eye population with European ancestry in UKBB (6,477,810 SNPs passing quality checks). In addition, ADNI WGS data resulted in 1,555 participants for the brain GWAS, with 24,194,338 SNPs passing quality checks (Supplementary Note 4 and Supplementary Fig. 13). We summarize our genetic quality check steps. First, we skipped the step for family relationship inference¹³⁶ because the linear mixed model via fastGWA¹³⁷ inherently addresses population stratification, encompassing additional cryptic population stratification factors. We then removed duplicated variants from all 22 autosomal chromosomes. Individuals whose genetically identified sex did not match their self-acknowledged sex were removed.

Other exclusion criteria were as follows: (1) individuals with more than 3% of missing genotypes, (2) variants with minor allele frequency (dosage mode) of less than 1%, (3) variants with larger than 3% missing genotyping rate, and (4) variants that failed the Hardy–Weinberg test at 1×10^{-10} . To further adjust for population stratification¹³⁸, we derived the first 40 genetic principal components using the FlashPCA software¹³⁹. Details of the genetic quality check protocol are described elsewhere^{17,20,23,33,93}.

GWAS. We applied a linear mixed model regression to the European ancestry populations using fastGWA¹³⁷ implemented in GCTA⁵⁶. For each GWAS, we corrected for common covariates (for example, age and sex) and organ-specific covariates (for example, MRI scanner positions for the brain).

Brain MAE GWAS. The brain MAE GWAS controlled for confounding factors, including age (Field ID 21003), age², sex (Field ID 31), age × sex interaction, age² × sex interaction, the first 40 genetic principal components, total intracranial volume, the scanner position in lateral, transverse and longitudinal directions (Field IDs 25756–25758), assessment center (Field ID 54) and BMI (Field ID 23104), guided by previous brain imaging GWASs¹⁴⁰.

Heart MAE GWAS. The model included age (Field ID 21003), age², sex (Field ID 31), age × sex interaction, age² × sex interaction, the first 40 genetic principal components, body weight (Field ID 21002), height (Field ID 50), waist circumference (Field ID 48), BMI (Field ID 23104), smoking status (Field ID 20116), assessment center (Field ID 54), heart rate (Field ID 12673), diastolic blood pressure (Field ID 12675), systolic blood pressure (Field ID 12674), peripheral pulse pressure (Field ID 12676), central pulse pressure (Field ID 12678), body surface area (Field ID 22427) and average heart rate (Field ID 22426) as covariates.

Eye MAE GWAS. The model included age (Field ID 21003), age², sex (Field ID 31), age × sex interaction, age² × sex interaction, the first 40 genetic principal components, body weight (Field ID 21002), height (Field ID 50), assessment center (Field ID 54) and waist circumference (Field ID 48) as covariates. For the abovementioned 3 GWASs, we used a stringent genome-wide *P* value threshold ($5 \times 10^{-8}/11$) using Bonferroni correction based on the number of total MAEs ($N=11$) to ensure stringent statistical rigor.

We scrutinized the robustness of our MAE GWASs through several sensitivity analyses. These checks included: (1) estimation of LDSC intercept, (2) a split-sample GWAS that randomly divided the entire heart population into two groups with no significant differences in sex and age, (3) sex-stratified GWAS conducted separately for males and females, and (4) a non-European GWAS to gauge the generalizability of GWAS signals identified in populations of European ancestry. We performed one additional sensitivity check for the brain MAE GWAS by generalizing the results to the WGS data from ADNI.

ProGWAS. Our ProGWAS followed the protocol of a recent study⁷² investigating plasma proteins' associations with genetics and health-related traits. We controlled the following covariates in our fastGWA model: age (Field ID 21003), age², sex (Field ID 31), age × sex interaction, age² × sex interaction, the first 40 genetic principal components, body weight (Field ID 21002), height (Field ID 50), assessment center (Field ID 54), waist circumference (Field ID 48), diastolic blood pressure (Field ID 12675) and systolic blood pressure (Field ID 12674). To identify the pQTLs in our ProGWAS, we pinpointed independent signals as defined in FUMA (refer to the section 'Annotation of genomic loci'). In line with previous research³¹, we defined *cis*-pQTLs for genomic loci where the top lead SNPs are located within 1 Mb of the gene encoding the corresponding protein. Conversely, loci beyond this range were classified as *trans*-pQTLs (for example, Fig. 5e).

Annotation of genomic loci. For the MAE GWASs, genomic loci were annotated using FUMA¹⁴¹. For genomic loci annotation, FUMA initially identified lead SNPs (correlation $r^2 \leq 0.1$, distance < 250 kilobases) and assigned them to non-overlapping genomic loci. The lead SNP with the lowest *P* value (that is, the top lead SNP) represented the genomic locus. Further details on the definitions of top lead SNP, lead SNP, independent significant SNP and candidate SNP can be found in Supplementary Method 1. For visualization purposes in Fig. 4, we have mapped the top lead SNP of each locus to the cytogenetic regions based on the GRCh37 cytoband.

PheWAS. We used the GWAS Atlas⁵⁵ platform to conduct an online PheWAS look-up analysis for the top lead SNP within each genomic locus; LD was fully considered. To facilitate this, we developed an 'in-house web crawler' designed to automate searches on the PheWAS webpage: <https://atlas.ctglab.nl/PheWAS>. The search threshold was set at a *P* value of 5×10^{-8} . The GWAS Atlas PheWAS categorized these traits into broad domains or categories that primarily affect respective organ systems. This PheWAS was conducted on September 16, 2023.

(c) SNP-based heritability. We calculated h^2_{SNP} using the GCTA software, which uses raw individual genotype data to generate a genetic relationship matrix, addressing the 'missing heritability' issue⁵⁶. From our experience, individual-level data approaches (for example, GCTA) generally obtained higher h^2_{SNP} estimates than summary-level methods (for example, LDSC), a trend observed in our previous findings¹⁷ and those of other research groups¹⁴⁰. Bonferroni correction based on the number of MAEs was applied to denote statistical significance.

(d) Selection signature and polygenicity estimate. We then used SBayesS⁵⁸ to estimate two additional genetic parameters that unveil the genetic architecture of the MAEs. SBayesS is designed to estimate key parameters related to the genetic architecture of complex traits. It uses a Bayesian mixed linear model⁹⁵ and requires only GWAS summary statistics for SNPs and LD information from a reference sample to perform these analyses. These parameters include polygenicity (π), and the relationship between minor allele frequency and effect size (S), that is, the selection signature. We used the software's precomputed sparse LD correlation matrix derived from the European ancestry by ref. 58, and ran the *gctb* command⁹⁵ using the argument *--sbayes S*. All other arguments were set by default.

(e) Gene–drug–disease network. We defined a gene–drug–disease network by examining the enrichment of the gene set linked to the 11 MAEs within specific drug categories from the DrugBank database⁶¹ using the GREP software¹⁴². First, we defined the MAE-specific gene set by three different gene mapping approaches: (1) physical position, (2) eQTL and (3) chromatin interactions (default parameters in FUMA). We then used these gene sets as input for GREP and conducted Fisher's exact tests to determine whether these gene sets were enriched in gene sets defined by drugs within clinical indication categories for specific diseases or conditions (based on the ICD code).

(f) Cell- and tissue-specific partitioned heritability estimate. We investigated different tissue types contributing to the heritability of the MAEs. To achieve this, the partitioned heritability analysis through stratified LD score regression assesses the extent of heritability enrichment attributed to predefined and annotated genome regions and categories⁶⁷. This analysis considers 3 sets of analyses considering different tissue types: (1) 3 cell types from ref. 143, (2) 498 multitissue chromatin-based annotations from peaks from 6 epigenetic marks using data from ROADMAP¹⁴⁴ and ENTEX¹⁴⁵, and (3) 205 multitissue gene expression data estimates using data from GTEx v.8 (ref. 146) and the 'Franke lab' dataset. Detailed methodologies for the stratified LD score regression are outlined in the original work⁶⁷. LD scores and allele

frequencies for European ancestry were acquired from a predefined version based on data from the 1000 Genomes Project.

(g) Genetic correlation. We estimated the g_c between each MAE pair using the LDSC software. Precomputed LD scores from the 1000 Genomes of European ancestry were used, maintaining default settings for other parameters in LDSC. It is worth noting that LDSC corrects for sample overlap, ensuring an unbiased genetic correlation estimate¹⁴⁷. Statistical significance was determined using Bonferroni correction. Three sets of analyses were performed: (1) pairwise MAEs, (2) the 11 MAEs versus the 9 multi-organ BAGs, and (3) the 11 MAEs versus the 521 FinnGen DEs and 4 PGC DEs.

(h) Two-sample bidirectional Mendelian randomization. We hypothesized that proteins and MAEs, acting as intermediate phenotypes (that is, the endophenotype hypothesis¹⁴⁸; refer to Supplementary Fig. 8 for a schematic illustration of our hypothesis), reside along the causal pathway from underlying genetics to chronic DEs. We constructed a multilayer causal network using multi-omics data (for example, imaging, genetics and proteomics).

To this end, we constructed 12 bidirectional causal networks: (1) Brain2Protein, (2) Protein2Brain, (3) Eye2Protein, (4) Protein2Eye, (5) Heart2Protein, (6) Protein2Heart, (7) Brain2DE, (8) DE2Brain, (9) Eye2DE, (10) DE2Eye, (11) Heart2DE, and (12) DE2Heart. These networks used summary statistics from our MAE GWAS analyses in the UKBB, the FinnGen¹²¹ and the PGC¹²³ study for the 11 MAEs and 525 DEs. For example, the Brain2DE causal network used the 11 MAEs from UKBB as exposure variables and the 525 DEs from FinnGen and PGC as outcome variables. The systematic quality-checking procedures to ensure unbiased exposure and outcome variables and IVs selection are detailed later.

We used a two-sample Mendelian randomization approach implemented in the TwoSampleMR package⁷¹ to infer the causal relationships within these networks. We used five distinct Mendelian randomization methods, presenting the results of the inverse-variance-weighted method in the main text and the outcomes of the other four methods (Egger, weighted median, simple mode and weighted mode estimators) in the Supplementary Information. The Strengthening the Reporting of Observational Studies in Epidemiology using Mendelian Randomization Statement¹⁴⁹ guided our analyses to increase transparency and reproducibility, encompassing the selection of exposure and outcome variables, reporting statistics and implementing sensitivity checks to identify potential violations of underlying assumptions. First, we performed an unbiased quality check on the GWAS summary statistics. Notably, the absence of population overlapping bias¹⁵⁰ was confirmed, given that FinnGen and UKBB participants largely represent populations of European ancestry without explicit overlap. PGC GWAS summary data were ensured to exclude UKBB participants. For networks between the proteins and MAEs from UKBB, we reran the ProGWAS and ensured no overlapping populations. Furthermore, all consortia's GWAS summary statistics were based on or lifted to GRCh37. Subsequently, we selected the effective exposure variables by assessing the statistical power of the exposure GWAS summary statistics in terms of IVs, ensuring that the number of IVs exceeded eight before harmonizing the data. Crucially, the function *clump_data* was applied to the exposure GWAS data, considering LD. The function *harmonise_data* was then used to harmonize the GWAS summary statistics of the exposure and outcome variables. This yielded fewer IVs than the original included MAEs, DEs or proteins. Bonferroni correction was applied to all tested traits based on the number of effective DEs, MAEs, proteins or diseases, whichever was larger.

Finally, we conducted multiple sensitivity analyses. First, we conducted a heterogeneity test to scrutinize potential violations of the IV's assumptions. To assess horizontal pleiotropy, which indicates the IV's exclusivity assumption¹⁵¹, we used a funnel plot, single-SNP Mendelian

randomization methods and the Egger estimator. Furthermore, we performed a leave-one-out analysis, systematically excluding one instrument (SNP or IV) at a time, to gauge the sensitivity of the results to individual SNPs.

(i) PRS calculation. The PRS was computed using split-sample sensitivity GWASs for the 11 MAE GWASs. The PRS weights were established using the split 1 discovery GWAS data as the base (training) set, and the split 2 replication GWAS summary statistics as the target (testing) data. Both base and target data underwent rigorous quality control procedures involving several steps: (1) excluding duplicated and ambiguous SNPs in the base data, (2) excluding high heterozygosity samples in the target data, and (3) eliminating duplicated, mismatching and ambiguous SNPs in the target data.

After completing the quality control procedures, PRS for the split 2 group was calculated using the polygenic risk score–continuous shrinkage (PRS-CS)¹⁵² method. PRS-CS applies a continuous shrinkage prior, which adjusts the SNP effect sizes based on their LD structure. SNPs with weaker evidence are 'shrunk' toward zero, while those with stronger evidence retain larger effect sizes. This avoids overfitting and improves prediction performance; no clumping was performed because the method takes LD into account. The shrinkage parameter was not set, and the algorithm learned it via a fully Bayesian approach.

Prediction and association analyses for the risk of DEs, AD progression, mortality, history of medication use and preclinical AD drug effects

We investigated the clinical promise of the proposed MAEs in 4 sets of prediction analyses: (1) survival analysis for the risk of DEs based on the ICD-10 code, ensuring each DE had at least 20 patients in each organ-specific population; (2) survival analysis for predicting the progression of AD progression (CN to MCI to AD); (3) survival analysis for predicting the risk of mortality; and (4) logistic regression to quantify the additional power (that is, incremental R^2).

Survival analysis for the incidence of DEs. Using UKBB ICD-based DEs, we used a Cox proportional hazard model while adjusting for covariates (that is, age and sex) to test the associations. The covariates were included as additional right-side variables in the model. The HR ($\exp(\beta_R)$ for the regression coefficient for that predictor R in the Cox model) was calculated and reported as the effect size measure that indicates the influence of each MAE on the risk of DEs. To train the model, the 'time' variable was determined by calculating the difference between the date of the first inpatient diagnosis (Field ID 41280) for a specific DE for cases (or the censoring date for non-cases) and the date attending the assessment center (Field ID 53). We excluded the participants whose time variable were negative (that is, diagnosed with the disease before entering the study). After entering the study, participants who received an ICD-based disease diagnosis were classified as cases.

Survival analysis for AD progression. Using 9,752 longitudinal brain MRI scans from ADNI (547 CN, 875 MCI and 343 AD at baseline) and the same Cox model, we evaluated the risk of AD progression for the 6 brain MAEs. Further, to quantitatively assess prognostic performances with the six brain MAEs as features, we progressively added the most predictive brain MAE, on top of age and sex, to the Cox model to understand its optimal performance. The concordance index was used to quantify the performance of risk prediction in a 100-repetition and 20% holdout cross-validation. For the progression of MCI to AD, the time variable was determined by calculating the difference between the age at AD diagnosis during follow-up for cases (or the censoring age for non-cases) and the age at baseline. Participants who received an AD diagnosis during the follow-up period were classified as cases. For the cumulative analyses, 5-fold cross-validation was run 100× to derive the concordance index on validation sets.

Survival analysis for mortality risk. Using the same Cox model and UKBB data, we also predicted the mortality risk of the 11 MAEs. To train the model, the time variable was determined by calculating the difference between the date of death (Field ID 40000) for cases (or the censoring date for non-cases) and the date attending the assessment center (Field ID 53). Participants who passed away after enrolling in the study were classified as cases.

Logistic regression for the pseudo incremental R^2 . We evaluated the predictive power of 11 MAEs on medication status at two levels of analysis, defining medication status. First, using a logistic regression model and UKBB data, we associated the medication status for four drug categories: (1) antipsychotic medications (Field ID 20466), (2) blood pressure medications (Field ID 6177 for males and 6153 for females), (3) cholesterol-lowering medication (Field ID 6177 for males and 6153 for females) and insulin (Field ID 6177 for males and 6153 for females). For participants not on blood pressure, cholesterol-lowering and insulin medications, we defined non-cases (CN) as individuals who had never taken the following additional drug: hormone replacement therapy. In addition, we excluded participants who responded with ‘none of the above’ or ‘prefer not to answer’ during the touchscreen questionnaire. We selected participants who reported taking any of these medications for each drug case during any study session. Second, to further validate the predictive capacity of the 11 MAEs for drug status, we investigated their association with 164 individual medications selected from UKBB (Field ID 20003) based on a minimum of 1,000 cases. The non-cases (CN) comprised individuals with no recorded history of exposure to the 6,745 available drugs.

To derive the incremental R^2 , we built a null and an alternative logistic regression using the statsmodels package. The null model predicted medication status based on age and sex as the features, while the alternative model included each MAE as an additional feature. The difference between the R^2 pseudo values for the alternative and null models reflected the incremental R^2 explained by the MAE. Bonferroni correction was performed based on the number of MAEs for each drug.

Natural cubic splines for modeling drug effects on the underexpressed, overexpressed patient groups in Brain 1–3 and the placebo group. In our survival analysis of MCI to AD progression, we observed a significantly higher risk in Brain 1–3. Therefore, we used clinical trial data from the A4 study⁴¹ to investigate whether our proposed brain MAE could serve as a tool for population selection in future AD clinical trials. The original trial did not show cognitive decline slowing compared with the placebo over 240 weeks, with the treatment group even showing a slight worsening in the PACC score. We hypothesized that heterogeneity exists in drug responses within the treatment group. To test this, we conducted three comparisons using natural cubic spline modeling: (1) underexpressed (for example, <Brain 1 median) versus overexpressed (for example, >Brain 1 median), to assess differential drug effects; (2) underexpressed versus placebo, to evaluate whether patients with lower brain MAE expression responded better (that is, beneficial effect) to the drug than the placebo group; and (3) overexpressed versus placebo, to determine if patients with higher brain MAE expression showed worsened cognition (that is, detrimental effect) compared with placebo (also stratified by the brain MAE for fair comparison).

From a statistical perspective, this is to model repeated measures (that is, PACC as the primary trial outcome for global cognition) as a continuous outcome in a mixed-effect model. We used the same method proposed by the original study¹⁵³, in which the authors proposed a constrained longitudinal data analysis with natural cubic splines that treated time as continuous and used test version effects to model the mean over time for PACC. Fixed effects included the following terms: (1) spline basis expansion terms (two terms), (2) interaction of the spline basis expansion terms with treatment (two terms), (3) the

version of the PACC test implemented, (4) baseline age, (5) education, (6) APOE4 carrier status (yes or no), and (7) baseline florbetapir cortical SUVr value (that is, standardized uptake value ratio). Following the guidance of the original method, several variance–covariance structures were sequentially assumed until the model converged with the heterogeneous Toeplitz. At week 240, we compared the mean PACC values between each pair of the two groups.

Reporting summary

Further information on research design is available in the Nature Portfolio Reporting Summary linked to this article.

Data availability

The GWAS summary statistics and pretrained AI models from this study are publicly accessible via the MEDICINE Knowledge Portal (<https://labs-laboratory.com/medicine/>) and Synapse (<https://www.synapse.org/Synapse:syn64923248/wiki/630992> (ref. 154)). Our study used data generated by the TCGA Research Network (<https://www.cancer.gov/tcga>), the HPA (<https://www.proteinatlas.org>) and the STRING database (<https://string-db.org/>). The two platforms curated and consolidated publicly available (single-cell) RNA-seq and protein data, including the GTEx project (<https://gtexportal.org/home/>). Genomic loci annotation used data from FUMA (<https://fuma.ctglab.nl/>). PheWAS used data from the GWAS Atlas platform (<https://atlas.ctglab.nl/PheWAS>). GWAS summary data for the DEs were downloaded from the official websites of FinnGen (R9: https://www.finngen.fi/en/access_results) and PGC (<https://pgc.unc.edu/researchers/download-results/>). Individual data from UKBB can be requested with proper registration at <https://www.ukbiobank.ac.uk/>. Data from ADNI can be requested with proper registration at <https://adni.loni.usc.edu/>. The gene–drug–disease network used data from the DrugBank database (v.5.1.9; <https://go.drugbank.com/>). The analysis for partitioned heritability estimates used data from ROADMAP (https://egg2.wustl.edu/roadmap/web_portal/) and ENTEX (<https://www.encodeproject.org/>). Due to privacy considerations, allele frequency information is available from the corresponding author upon request for research purposes only, with responses typically provided within 1 week. All main figures, extended data figures and the supplementary files are available on Zenodo at <https://zenodo.org/records/17156245> (ref. 155).

Code availability

The software and resources used in this study are all publicly available. For disease heterogeneity analysis, Surreal-GAN (v.0.1.1): <https://github.com/zhijian-yang/SurrealGAN>. For RAVENS map extraction, MUSE (v.3.1.0): <https://github.com/CBICA/MUSE>. For Brain PSC extraction, SOPNMF (v.0.0.4): <https://github.com/anbai106/SOPNMF>. For Heart IDP extraction, ukbb_cardiac (git commit 2b6d637): https://github.com/baiwenjia/ukbb_cardiac. For gene mapping and genomic locus annotation, FUMA (v.1.5.0): <https://fuma.ctglab.nl/>. For heritability estimates and fastGWA, GCTA (v1.94.1): <https://yanglab.westlake.edu.cn/software/gcta/#Overview>. For genetic correlation, LDSC (git commit aa33296): <https://github.com/bulik/ldsc>. For Mendelian randomization, TwoSampleMR (v.0.5.6): <https://mrcieu.github.io/TwoSampleMR/index.html>. For PRS calculation, PRS-CS (release date August 10, 2023): <https://github.com/getian107/PRScs>. For the three key parameter estimates, SBayesS (v.2.0.5 beta): <https://cnsgenomics.com/software/gctb/#Overview>. For survival analysis, Lifelines (v.0.27.): <https://lifelines.readthedocs.io/en/latest/>. For medication prediction, BWAS, PWAS and ProWAS, Statsmodels (0.13.2): <https://www.statsmodels.org/stable/index.html>. For PPI, OmicVerse (v.1.6.7): <https://omicverse.readthedocs.io/en/latest/>.

References

1. Hodson, R. Precision medicine. *Nature* **537**, S49–S49 (2016).

2. Yang, Z. et al. A deep learning framework identifies dimensional representations of Alzheimer's disease from brain structure. *Nat. Commun.* **12**, 7065 (2021).
3. Young, A. L. et al. Uncovering the heterogeneity and temporal complexity of neurodegenerative diseases with subtype and stage inference. *Nat. Commun.* **9**, 4273 (2018).
4. Gandal, M. J. et al. Shared molecular neuropathology across major psychiatric disorders parallels polygenic overlap. *Science* **359**, 693–697 (2018).
5. Anttila, V. Analysis of shared heritability in common disorders of the brain. *Science* **360**, eaap8757 (2018).
6. Lalousis, P. A. et al. Neurobiologically based stratification of recent-onset depression and psychosis: identification of two distinct transdiagnostic phenotypes. *Biol. Psychiatry* **92**, 552–562 (2022).
7. Siugzdaite, R., Bathelt, J., Holmes, J. & Astle, D. E. Transdiagnostic brain mapping in developmental disorders. *Curr. Biol.* **30**, 1245–1257.e4 (2020).
8. Wen, J. et al. Dimensional neuroimaging endophenotypes: neurobiological representations of disease heterogeneity through machine learning. *Biol. Psychiatry* **96**, 564–584 (2024).
9. Yang, Z., Wen, J. & Davatzikos, C. Surreal-GAN: semi-supervised representation learning via GAN for uncovering heterogeneous disease-related imaging patterns. In *Proc. Ninth International Conference on Learning Representations (ICLR)* <https://openreview.net/pdf?id=nf3AOWZsXS5> (2022).
10. Yang, Z. et al. Brain aging patterns in a large and diverse cohort of 49,482 individuals. *Nat. Med.* <https://doi.org/10.1038/s41591-024-03144-x> (2024).
11. Wen, J. et al. Neuroimaging endophenotypes reveal underlying mechanisms and genetic factors contributing to progression and development of four brain disorders. *Nat. Biomed. Eng.* <https://doi.org/10.1038/s41551-025-01412-w> (2025).
12. D'Angelo, E. & Jirsa, V. The quest for multiscale brain modeling. *Trends Neurosci.* **45**, 777–790 (2022).
13. The MULTI Consortium et al. Multi-organ metabolome biological age implicates cardiometabolic conditions and mortality risk. *Nat. Commun.* **16**, 4871 (2025).
14. The MULTI Consortium et al. MRI-based multi-organ clocks for healthy aging and disease assessment. *Nat. Med.* <https://doi.org/10.1038/s41591-025-03999-8> (2025).
15. Wen, J. Towards a multi-organ, multi-omics medical digital twin. *Nat. Biomed. Eng.* <https://doi.org/10.1038/s41551-025-01474-w> (2025).
16. The MULTI Consortium et al. Brain–heart–eye axis revealed by multi-organ imaging genetics and proteomics. *Nat. Bio. Med. Eng.* <https://doi.org/10.1038/s41551-025-01506-5> (2025).
17. Wen, J. et al. The genetic architecture of biological age in nine human organ systems. *Nat. Aging* <https://doi.org/10.1038/s43587-024-00662-8> (2024).
18. Wen, J. Refining the generation, interpretation, and application of multi-organ, multi-omics biological aging clocks. *Nat. Aging* <https://doi.org/10.1038/s43587-025-00928-9> (2025).
19. Tian, Y. E. et al. Heterogeneous aging across multiple organ systems and prediction of chronic disease and mortality. *Nat. Med.* <https://doi.org/10.1038/s41591-023-02296-6> (2023).
20. Wen, J. et al. The genetic architecture of multimodal human brain age. *Nat. Commun.* **15**, 2604 (2024).
21. Yang, Z. et al. Gene-SGAN: discovering disease subtypes with imaging and genetic signatures via multi-view weakly-supervised deep clustering. *Nat. Commun.* **15**, 354 (2024).
22. Wen, J. Multiorgan biological age shows that no organ system is an island. *Nat. Aging* <https://doi.org/10.1038/s43587-024-00690-4> (2024).
23. Wen, J. et al. Genomic loci influence patterns of structural covariance in the human brain. *Proc. Natl. Acad. Sci. USA* **120**, e2300842120 (2023).
24. Bai, W. et al. A population-based genome-wide association study of cardiac and aortic structure and function. *Nat. Med.* **26**, 1654–1662 (2020).
25. Patel, P. J. et al. Spectral-domain optical coherence tomography imaging in 67 321 adults: associations with macular thickness in the UK Biobank Study. *Ophthalmology* **123**, 829–840 (2016).
26. Ko, F. et al. Associations with retinal pigment epithelium thickness measures in a large cohort: results from the UK Biobank. *Ophthalmology* **124**, 105–117 (2017).
27. Han, X. et al. Genome-wide association analysis of 95 549 individuals identifies novel loci and genes influencing optic disc morphology. *Hum. Mol. Genet.* **28**, 3680–3690 (2019).
28. Kendler, K. & Neale, M. Endophenotype: a conceptual analysis. *Mol. Psychiatry* **15**, 789–797 (2010).
29. Boquet-Pujadas, A. et al. MUTATE: a human genetic atlas of multiorgan artificial intelligence endophenotypes using genome-wide association summary statistics. *Brief. Bioinform.* **26**, bbaf125 (2025).
30. Aaltonen, L. A. et al. Pan-cancer analysis of whole genomes. *Nature* **578**, 82–93 (2020).
31. Sun, B. B. et al. Plasma proteomic associations with genetics and health in the UK Biobank. *Nature* **622**, 329–338 (2023).
32. Vogel, J. W. et al. Four distinct trajectories of tau deposition identified in Alzheimer's disease. *Nat. Med.* **27**, 871–881 (2021).
33. Wen, J. et al. Characterizing heterogeneity in neuroimaging, cognition, clinical symptoms, and genetics among patients with late-life depression. *JAMA Psychiatry* <https://doi.org/10.1001/jamapsychiatry.2022.0020> (2022).
34. Jiang, Y. et al. Neurostructural subgroup in 4,291 individuals with schizophrenia identified using the subtype and stage inference algorithm. *Nat. Commun.* **15**, 5996 (2024).
35. Chand, G. B. et al. Two distinct neuroanatomical subtypes of schizophrenia revealed using machine learning. *Brain* **143**, 1027–1038 (2020).
36. De la Paz, M. A., Pericak-Vance, M. A., Haines, J. L. & Seddon, J. M. Phenotypic heterogeneity in families with age-related macular degeneration. *Am. J. Ophthalmol.* **124**, 331–343 (1997).
37. Ali, M. H. et al. Circular functional analysis of OCT data for precise identification of structural phenotypes in the eye. *Sci. Rep.* **11**, 23336 (2021).
38. Baptiste, D. et al. Heterogeneity in cardiovascular disease risk factor prevalence among white, African American, African immigrant, and Afro-Caribbean adults: insights from the 2010–2018 National Health Interview Survey. *J. Am. Heart Assoc.* **11**, e025235 (2022).
39. Duggan, M. R. et al. Proteomic analyses reveal plasma EFEMP1 and CXCL12 as biomarkers and determinants of neurodegeneration. *Alzheimers Dement.* <https://doi.org/10.1002/alz.14142> (2024).
40. Rossman, I. Normal human aging: The Baltimore Longitudinal Study of Aging. *JAMA* **255**, 960–960 (1986).
41. Sperling, R. A. et al. Trial of solanezumab in preclinical Alzheimer's disease. *N. Engl. J. Med.* **389**, 1096–1107 (2023).
42. Sperling, R. A. et al. Association of factors with elevated amyloid burden in clinically normal older individuals. *JAMA Neurol.* **77**, 735–745 (2020).
43. Petersen, R. C. et al. Alzheimer's Disease Neuroimaging Initiative (ADNI): clinical characterization. *Neurology* **74**, 201–209 (2010).
44. Tosun, D., Schuff, N., Shaw, L. M., Trojanowski, J. Q. & Weiner, M. W. Relationship between CSF biomarkers of Alzheimer's disease and rates of regional cortical thinning in ADNI data. *J. Alzheimers Dis.* **26**, 77–90 (2011).

45. Hahn, J. et al. Evolution of neuronal cell classes and types in the vertebrate retina. *Nature* **624**, 415–424 (2023).
46. Wang, J. et al. Role of oxidative stress in retinal disease and the early intervention strategies: a review. *Oxid. Med. Cell Longev.* **2022**, 7836828 (2022).
47. Diniz, C. R. A. F. & Crestani, A. P. The times they are a-changin': a proposal on how brain flexibility goes beyond the obvious to include the concepts of 'upward' and 'downward' to neuroplasticity. *Mol. Psychiatry* **28**, 977–992 (2023).
48. Mathys, H. et al. Single-cell multiregion dissection of Alzheimer's disease. *Nature* **632**, 858–868 (2024).
49. Beal, E. Cancer link to Alzheimer disease, but not vascular dementia. *Nat. Rev. Neurol.* **6**, 124 (2010).
50. Carr, S. et al. A burden of proof study on alcohol consumption and ischemic heart disease. *Nat. Commun.* **15**, 4082 (2024).
51. Gadd, D. A. et al. Blood protein assessment of leading incident diseases and mortality in the UK Biobank. *Nat. Aging* **4**, 939–948 (2024).
52. Carrasco-Zanini, J. et al. Proteomic signatures improve risk prediction for common and rare diseases. *Nat. Med* **30**, 2489–2498 (2024).
53. Wu, D. et al. The blood-brain barrier: structure, regulation and drug delivery. *Signal Transduct. Target Ther.* **8**, 217 (2023).
54. Eldjarn, G. H. et al. Large-scale plasma proteomics comparisons through genetics and disease associations. *Nature* <https://doi.org/10.1038/s41586-023-06563-x> (2023).
55. Watanabe, K. et al. A global overview of pleiotropy and genetic architecture in complex traits. *Nat. Genet.* **51**, 1339–1348 (2019).
56. Yang, J., Lee, S. H., Goddard, M. E. & Visscher, P. M. GCTA: a tool for genome-wide complex trait analysis. *Am. J. Hum. Genet.* **88**, 76–82 (2011).
57. Bulik-Sullivan, B. K. et al. LD score regression distinguishes confounding from polygenicity in genome-wide association studies. *Nat. Genet.* **47**, 291–295 (2015).
58. Zeng, J. et al. Widespread signatures of natural selection across human complex traits and functional genomic categories. *Nat. Commun.* **12**, 1164 (2021).
59. Park, J. et al. Integrated platform for multiscale molecular imaging and phenotyping of the human brain. *Science* **384**, eadh9979 (2024).
60. Gómez-Robles, A., Nicolaou, C., Smaers, J. B. & Sherwood, C. C. The evolution of human altriciality and brain development in comparative context. *Nat. Ecol. Evol.* **8**, 133–146 (2024).
61. Wishart, D. S. et al. DrugBank 5.0: a major update to the DrugBank database for 2018. *Nucleic Acids Res.* **46**, D1074–D1082 (2018).
62. Nelson, M. R. et al. The support of human genetic evidence for approved drug indications. *Nat. Genet.* **47**, 856–860 (2015).
63. Minikel, E. V., Painter, J. L., Dong, C. C. & Nelson, M. R. Refining the impact of genetic evidence on clinical success. *Nature* **629**, 624–629 (2024).
64. Mummery, C. J. et al. Tau-targeting antisense oligonucleotide MAPTRx in mild Alzheimer's disease: a phase 1b, randomized, placebo-controlled trial. *Nat. Med.* **29**, 1437–1447 (2023).
65. Gherghel, D., Hosking, S. L., Cunliffe, I. A. & Armstrong, R. A. First-line therapy with latanoprost 0.005% results in improved ocular circulation in newly diagnosed primary open-angle glaucoma patients: a prospective, 6-month, open-label study. *Eye* **22**, 363–369 (2008).
66. Callari, M. et al. Cancer-specific association between Tau (MAPT) and cellular pathways, clinical outcome, and drug response. *Sci. Data* **10**, 637 (2023).
67. Finucane, H. K. et al. Partitioning heritability by functional annotation using genome-wide association summary statistics. *Nat. Genet.* **47**, 1228–1235 (2015).
68. Cheverud, J. M. A comparison of genetic and phenotypic correlations. *Evolution* **42**, 958–968 (1988).
69. Zhu, X. et al. An approach to identify gene-environment interactions and reveal new biological insight in complex traits. *Nat. Commun.* **15**, 3385 (2024).
70. Xie, X., Sun, X., Wang, Y., Lehner, B. & Li, X. Dominance vs epistasis: the biophysical origins and plasticity of genetic interactions within and between alleles. *Nat. Commun.* **14**, 5551 (2023).
71. Hemani, G. et al. The MR-Base platform supports systematic causal inference across the human genome. *eLife* **7**, e34408 (2018).
72. Sun, B. B. et al. Plasma proteomic associations with genetics and health in the UK Biobank. *Nature* <https://doi.org/10.1038/s41586-023-06592-6> (2023).
73. Bonanno, L. et al. Brain morphologic abnormalities in migraine patients: an observational study. *J. Headache Pain* **21**, 39 (2020).
74. Kaag Rasmussen, M. et al. Trigeminal ganglion neurons are directly activated by influx of CSF solutes in a migraine model. *Science* **385**, 80–86 (2024).
75. Wood, H. Migraine—a risk factor for cardiovascular disease?. *Nat. Rev. Neurol.* **14**, 195–195 (2018).
76. Ferrari, M. D. et al. Migraine. *Nat. Rev. Dis. Prim.* **8**, 2 (2022).
77. Taylor, J. J. et al. A transdiagnostic network for psychiatric illness derived from atrophy and lesions. *Nat. Hum. Behav.* **7**, 420–429 (2023).
78. Ravikumar, S. et al. Postmortem imaging reveals patterns of medial temporal lobe vulnerability to tau pathology in Alzheimer's disease. *Nat. Commun.* **15**, 4803 (2024).
79. Halliday, G. Pathology and hippocampal atrophy in Alzheimer's disease. *Lancet Neurol.* **16**, 862–864 (2017).
80. Bonilha, L. et al. Neurocognitive deficits and prefrontal cortical atrophy in patients with schizophrenia. *Schizophr. Res* **101**, 142–151 (2008).
81. Hwang, G. et al. Assessment of neuroanatomical endophenotypes of autism spectrum disorder and association with characteristics of individuals with schizophrenia and the general population. *JAMA Psychiatry* <https://doi.org/10.1001/jamapsychiatry.2023.0409> (2023).
82. Fu, C. H. Y. et al. Neuroanatomical dimensions in medication-free individuals with major depressive disorder and treatment response to SSRI antidepressant medications or placebo. *Nat. Ment. Health* **2**, 164–176 (2024).
83. Shuman Paretsky, M. & Roman, G. C. Association of lower extremity peripheral nerve impairment and the risk of dementia. *Neurology* **98**, 741–742 (2022).
84. Ferrara, D. et al. Optical coherence tomography features preceding the onset of advanced age-related macular degeneration. *Invest. Ophthalmol. Vis. Sci.* **58**, 3519–3529 (2017).
85. Sathyam, P., Shilpa, S. & Anitha, A. Optical coherence tomography in glaucoma. *J. Curr. Glaucoma Pract.* **6**, 1–5 (2012).
86. Ferris, F. L. & Patz, A. Macular edema. A complication of diabetic retinopathy. *Surv. Ophthalmol.* **28**, 452–461 (1984).
87. Burgoyne, C. The morphological difference between glaucoma and other optic neuropathies. *J. Neuroophthalmol.* **35**, S8–S21 (2015).
88. Ruilope, L. M. & Schmieder, R. E. Left ventricular hypertrophy and clinical outcomes in hypertensive patients. *Am. J. Hypertens.* **21**, 500–508 (2008).
89. Minicucci, M. F., Azevedo, P. S., Polegato, B. F., Paiva, S. A. R. & Zornoff, L. A. M. Heart failure after myocardial infarction: clinical implications and treatment. *Clin. Cardiol.* **34**, 410–414 (2011).
90. Leung, K. K. et al. Cerebral atrophy in mild cognitive impairment and Alzheimer disease. *Neurology* **80**, 648–654 (2013).
91. Olesen, P. J. et al. A population-based study on the influence of brain atrophy on 20-year survival after age 85. *Neurology* **76**, 879 (2011).

92. Hanlon, F. M. et al. The clinical relevance of gray matter atrophy and microstructural brain changes across the psychosis continuum. *Schizophrenia Res.* **229**, 12–21 (2021).
93. Wen, J. et al. Genetic and clinical correlates of two neuroanatomical AI dimensions in the Alzheimer's disease continuum. *Transl. Psychiatry* **14**, 420 (2024).
94. Skouras, S. et al. Mechanisms of functional compensation, delineated by eigenvector centrality mapping, across the pathophysiological continuum of Alzheimer's disease. *NeuroImage Clin.* **22**, 101777 (2019).
95. Zeng, J. et al. Signatures of negative selection in the genetic architecture of human complex traits. *Nat. Genet.* **50**, 746–753 (2018).
96. Bertorelle, G. et al. Genetic load: genomic estimates and applications in non-model animals. *Nat. Rev. Genet.* **23**, 492–503 (2022).
97. de Boer, I., Terwindt, G. M. & van den Maagdenberg, A. M. J. M. Genetics of migraine aura: an update. *J. Headache Pain* **21**, 64 (2020).
98. Li, J. et al. Expression of FLRT2 in postnatal central nervous system development and after spinal cord injury. *Front. Mol. Neurosci.* **14**, 756264 (2021).
99. Peng, H. et al. Epigenome-wide association study identifies novel genes associated with ischemic stroke. *Clin. Epigenetics* **15**, 106 (2023).
100. Sklar, P. et al. Large-scale genome-wide association analysis of bipolar disorder identifies a new susceptibility locus near ODZ4. *Nat. Genet.* **43**, 977–983 (2011).
101. Nordmann, T. M. et al. Spatial proteomics identifies JAK1 as treatment for a lethal skin disease. *Nature* <https://doi.org/10.1038/s41586-024-08061-0> (2024).
102. Zhao, J. H. et al. Genetics of circulating inflammatory proteins identifies drivers of immune-mediated disease risk and therapeutic targets. *Nat. Immunol.* **24**, 1540–1551 (2023).
103. Kim, C. U. & Pearce, W. A. Metastatic breast carcinoma involving the optic disc. *Am. J. Ophthalmol. Case Rep.* **18**, 100698 (2020).
104. Fishman, M. L., Tomaszewski, M. M. & Kuwabara, T. Malignant melanoma of the skin metastatic to the eye: frequency in autopsy series. *Arch. Ophthalmol.* **94**, 1309–1311 (1976).
105. Goldstein, S. M. et al. Cancer-associated retinopathy. *Arch. Ophthalmol.* **117**, 1641–1645 (1999).
106. Nuzzi, R. et al. Ocular complications after radiation therapy: an observational study. *Clin. Ophthalmol.* **14**, 3153–3166 (2020).
107. Di Cesare, M. et al. The heart of the world. *Glob. Heart* **19**, 11 (2024).
108. Harjola, V.-P. et al. Organ dysfunction, injury and failure in acute heart failure: from pathophysiology to diagnosis and management. A review on behalf of the Acute Heart Failure Committee of the Heart Failure Association (HFA) of the European Society of Cardiology (ESC). *Eur. J. Heart Fail.* **19**, 821–836 (2017).
109. Levin, M. G. et al. Genome-wide association and multi-trait analyses characterize the common genetic architecture of heart failure. *Nat. Commun.* **13**, 6914 (2022).
110. Pirruccello, J. P. et al. Analysis of cardiac magnetic resonance imaging in 36,000 individuals yields genetic insights into dilated cardiomyopathy. *Nat. Commun.* **11**, 2254 (2020).
111. Spielmann, N. et al. Extensive identification of genes involved in congenital and structural heart disorders and cardiomyopathy. *Nat. Cardiovasc. Res.* **1**, 157–173 (2022).
112. Tanaka, A. & Node, K. Associations of metabolic disorders with hypertension and cardiovascular disease: recent findings and therapeutic perspectives. *Hypertens. Res.* <https://doi.org/10.1038/s41440-024-01737-0> (2024).
113. Mufarreh, A., Shah, A. J., Vaccarino, V. & Kulshreshtha, A. Trends in provision of medications and lifestyle counseling in ambulatory settings by gender and race for patients with atherosclerotic cardiovascular disease, 2006–2016. *JAMA Netw. Open* **6**, e2251156 (2023).
114. Lu, Q. et al. Association of lifestyle factors and antihypertensive medication use with risk of all-cause and cause-specific mortality among adults with hypertension in China. *JAMA Netw. Open* **5**, e2146118 (2022).
115. Thangaraj, P. M., Benson, S. H., Oikonomou, E. K., Asselbergs, F. W. & Khera, R. Cardiovascular care with digital twin technology in the era of generative artificial intelligence. *Eur. Heart J.* <https://doi.org/10.1093/eurheartj/ehae619> (2024).
116. McCracken, C. et al. Multi-organ imaging demonstrates the heart–brain–liver axis in UK Biobank participants. *Nat. Commun.* **13**, 7839 (2022).
117. Liu, Y. et al. Genetic architecture of 11 organ traits derived from abdominal MRI using deep learning. *Elife* **10**, e65554 (2021).
118. Oh, H. S.-H. et al. Organ aging signatures in the plasma proteome track health and disease. *Nature* **624**, 164–172 (2023).
119. Morais, L. H., Schreiber, H. L. & Mazmanian, S. K. The gut microbiota–brain axis in behaviour and brain disorders. *Nat. Rev. Microbiol.* **19**, 241–255 (2021).
120. Bycroft, C. et al. The UK Biobank resource with deep phenotyping and genomic data. *Nature* **562**, 203–209 (2018).
121. Kurki, M. I. et al. FinnGen provides genetic insights from a well-phenotyped isolated population. *Nature* **613**, 508–518 (2023).
122. Mbatchou, J. et al. Computationally efficient whole-genome regression for quantitative and binary traits. *Nat. Genet.* **53**, 1097–1103 (2021).
123. O'Donovan, M. C. What have we learned from the Psychiatric Genomics Consortium. *World Psychiatry* **14**, 291–293 (2015).
124. Sotiras, A., Resnick, S. M. & Davatzikos, C. Finding imaging patterns of structural covariance via non-negative matrix factorization. *NeuroImage* **108**, 1–16 (2015).
125. Yang, Z. & Oja, E. Linear and nonlinear projective nonnegative matrix factorization. *IEEE Trans. Neural Netw.* **21**, 734–749 (2010).
126. Stretton, B., Kovoor, J. G., Bacchi, S. & Chan, W. O. A common factor? Sleep, macular degeneration and neurodegenerative disease. *Eye* <https://doi.org/10.1038/s41433-023-02607-8> (2023).
127. Zhou, M., Li, D.-L., Kai, J.-Y., Zhang, X.-F. & Pan, C.-W. Sleep duration and the risk of major eye disorders: a systematic review and meta-analysis. *Eye* **37**, 2707–2715 (2023).
128. Kriegeskorte, N., Simmons, W. K., Bellgowan, P. S. F. & Baker, C. I. Circular analysis in systems neuroscience: the dangers of double dipping. *Nat. Neurosci.* **12**, 535–540 (2009).
129. Li, W. U. K. Biobank pharma proteomics resource. *Nat. Genet.* **55**, 1781 (2023).
130. Uhlen, M. et al. Tissue-based map of the human proteome. *Science* **347**, 1260419 (2015).
131. Ratnapriya, R. et al. Retinal transcriptome and eQTL analyses identify genes associated with age-related macular degeneration. *Nat. Genet.* **51**, 606–610 (2019).
132. Takahashi, H., Lassmann, T., Murata, M. & Carninci, P. 5' end-centered expression profiling using cap-analysis gene expression and next-generation sequencing. *Nat. Protoc.* **7**, 542–561 (2012).
133. Zeng, Z. et al. OmicVerse: a framework for bridging and deepening insights across bulk and single-cell sequencing. *Nat. Commun.* **15**, 5983 (2024).
134. Szklarczyk, D. et al. The STRING database in 2023: protein–protein association networks and functional enrichment analyses for any sequenced genome of interest. *Nucleic Acids Res.* **51**, D638–D646 (2023).
135. von Mering, C. et al. STRING: known and predicted protein–protein associations, integrated and transferred across organisms. *Nucleic Acids Res.* **33**, D433–D437 (2005).
136. Manichaikul, A. et al. Robust relationship inference in genome-wide association studies. *Bioinformatics* **26**, 2867–2873 (2010).

137. Jiang, L. et al. A resource-efficient tool for mixed model association analysis of large-scale data. *Nat. Genet.* **51**, 1749–1755 (2019).
138. Price, A. L., Zaitlen, N. A., Reich, D. & Patterson, N. New approaches to population stratification in genome-wide association studies. *Nat. Rev. Genet.* **11**, 459–463 (2010).
139. Abraham, G., Qiu, Y. & Inouye, M. FlashPCA2: principal component analysis of Biobank-scale genotype datasets. *Bioinformatics* **33**, 2776–2778 (2017).
140. Elliott, L. T. et al. Genome-wide association studies of brain imaging phenotypes in UK Biobank. *Nature* **562**, 210–216 (2018).
141. Watanabe, K., Taskesen, E., van Bochoven, A. & Posthuma, D. Functional mapping and annotation of genetic associations with FUMA. *Nat. Commun.* **8**, 1826 (2017).
142. Sakaue, S. & Okada, Y. GREP: genome for REPositioning drugs. *Bioinformatics* **35**, 3821–3823 (2019).
143. Cahoy, J. D. et al. A transcriptome database for astrocytes, neurons, and oligodendrocytes: a new resource for understanding brain development and function. *J. Neurosci.* **28**, 264–278 (2008).
144. Bernstein, B. E. et al. The NIH Roadmap Epigenomics Mapping Consortium. *Nat. Biotechnol.* **28**, 1045–1048 (2010).
145. Dunham, I. et al. An integrated encyclopedia of DNA elements in the human genome. *Nature* **489**, 57–74 (2012).
146. GTEx Consortium. The Genotype-Tissue Expression (GTEx) project. *Nat. Genet.* **45**, 580–585 (2013).
147. Bulik-Sullivan, B. et al. An atlas of genetic correlations across human diseases and traits. *Nat. Genet.* **47**, 1236–1241 (2015).
148. Gottesman, I. I. & Gould, T. D. The endophenotype concept in psychiatry: etymology and strategic intentions. *Am. J. Psychiatry* **160**, 636–645 (2003).
149. Skrivanova, V. W. et al. Strengthening the Reporting of Observational Studies in Epidemiology Using Mendelian Randomization: The STROBE-MR Statement. *JAMA* **326**, 1614–1621 (2021).
150. Sanderson, E. et al. Mendelian randomization. *Nat. Rev. Methods Prim.* **2**, 6 (2022).
151. Bowden, J. et al. A framework for the investigation of pleiotropy in two-sample summary data Mendelian randomization. *Stat. Med.* **36**, 1783–1802 (2017).
152. Ge, T., Chen, C.-Y., Ni, Y., Feng, Y.-C. A. & Smoller, J. W. Polygenic prediction via Bayesian regression and continuous shrinkage priors. *Nat. Commun.* **10**, 1776 (2019).
153. Donohue, M. C. et al. Natural cubic splines for the analysis of Alzheimer's clinical trials. *Pharm. Stat.* **22**, 508–519 (2023).
154. Wen, J. MEDICINE: AI-derived GWAS summary statistics sharing portal. *Synapse* <https://doi.org/10.7303/SYN64923248> (2025).
155. Wen, J. Pan-disease of the brain–eye–heart axis. *Zenodo* <https://doi.org/10.5281/zenodo.17156245> (2025).
156. Jumper, J. et al. Highly accurate protein structure prediction with AlphaFold. *Nature* **596**, 583–589 (2021).

Acknowledgements

This research is supported through funding from the National Institute on Aging (NIA)-supported MULTI Consortium (J.W.; grant number RF1AG092412). The MULTI consortium (J.W.; UKBB application number 647044) aims to integrate multi-organ imaging and multi-omics data to advance our understanding of human aging and disease mechanisms. This study used the UKBB resource under application numbers 647044 (J.W.), 35148 (C.D.; grant number RF1AG054409) and 60698 (A.Z.). M.R.D., C.M.J., and K.A.W. were supported in part by the NIA Intramural Research Program of the National Institutes of Health (NIH). We thank the UKBB team for their invaluable contribution to advancing clinical research in our field (<https://www.ukbiobank.ac.uk/>).

We also acknowledge the UKBB Eye and Vision Consortium (<https://www.ukbiobank.ac.uk/enable-your-research/approved-research/genetic-contribution-to-vision-loss-and-disability-the-uk-biobank-eye-vision-consortium>; return ID 1875) and UKB-PPP consortium (<https://registry.opendata.aws/ukbfff/>; category code 1838) for sharing returned data with the community. We thank the BLSA participants and staff for their participation and continued dedication. The BLSA protocol was approved by the Institutional Review Board of the National Institute of Environmental Health Science, NIH (O3AG0325). Part of the data used was obtained from the ADNI database. The investigators within ADNI contributed to the design and implementation of ADNI and/or provided data but did not participate in the analysis or writing of this report. A complete listing of ADNI investigators can be found at: http://adni.loni.usc.edu/wp-content/uploads/how_to_apply/ADNI_Acknowledgement_List.pdf. The A4 study was a secondary prevention trial in preclinical AD, aiming to slow cognitive decline associated with brain amyloid accumulation in clinically normal older individuals. The A4 study was funded by a public-private-philanthropic partnership, including funding from the NIH National Institute on Aging, Eli Lilly and Company, Alzheimer's Association, Accelerating Medicines Partnership, GHR Foundation, an anonymous foundation and additional private donors, with in-kind support from Avid Radiopharmaceuticals, Cogstate, Albert Einstein College of Medicine and the Foundation for Neurologic Diseases. The companion observational Longitudinal Evaluation of Amyloid Risk and Neurodegeneration (LEARN) study was funded by the Alzheimer's Association and GHR Foundation. The A4 and LEARN studies were led by R. Sperling at Brigham and Women's Hospital, Harvard Medical School, and P. Aisen at the Alzheimer's Therapeutic Research Institute (ATRI) at the University of Southern California. The A4 and LEARN studies were coordinated by ATRI at the University of Southern California, and the data are made available under the auspices of the Alzheimer's Clinical Trial Consortium through the Global Research and Imaging Platform (GRIP). The complete A4 study team list is available at: <https://www.actcinfo.org/a4-study-team-lists/>. We acknowledge the dedication of the study participants and their partners who made the A4 and LEARN studies possible. We acknowledge the participants and investigators of the FinnGen study and the PGC consortium, and we thank FinnGen (<https://www.finngen.fi/en>) and PGC (<https://pgc.unc.edu/>) for their generosity in sharing the GWAS summary statistics with the scientific community.

Author contributions

J.W. is the representative for the MULTI Consortium. J.W. has full access to all the study data and is responsible for its integrity and accuracy. Study concept and design: J.W. Drafting of the paper: J.W. Critical revision of the paper for important intellectual content: A.B.-P., F.A., Z.Y., Y.E.T., M.R.D., G.E., D.S., C.M.J., W.B., P.J.P., K.A.W., A.Z., C.D. and J.W. Statistical analysis: J.W. ran all main analyses; A.B.-P. and F.A. helped with the development of the MEDICINER portal; M.R.D. ran the ProWAS for the SomaScan proteomic data in the BLSA sample. Detailed contributions: J.W. leads the MULTI consortium; C.D. represents the iSTAGING consortium; G.E. and D.S. conducted the image-preprocessing pipelines for the brain MRI from the A4 study; W.B. derived the original heart IDPs; P.J.P. derived the original eye IDPs; K.A.W. represents the BLSA study; A.Z. and Y.E.T. derived the nine multi-organ BAGs; and Z.Y. developed the Surreal-GAN model.

Competing interests

The authors declare no competing interests.

Additional information

Extended data is available for this paper at <https://doi.org/10.1038/s44220-025-00560-x>.

Supplementary information The online version contains supplementary material available at <https://doi.org/10.1038/s44220-025-00560-x>.

Correspondence and requests for materials should be addressed to Junhao Wen.

Peer review information *Nature Mental Health* thanks Kanhao Zhao and the other, anonymous, reviewer(s) for their contribution to the peer review of this work.

Reprints and permissions information is available at www.nature.com/reprints.

Publisher's note Springer Nature remains neutral with regard to jurisdictional claims in published maps and institutional affiliations.

Open Access This article is licensed under a Creative Commons Attribution-NonCommercial-NoDerivatives 4.0 International License, which permits any non-commercial use, sharing, distribution and reproduction in any medium or format, as long as you give appropriate credit to the original author(s) and the source, provide a link to the Creative Commons licence, and indicate if you modified the licensed material. You do not have permission under this licence to share adapted material derived from this article or parts of it. The images or other third party material in this article are included in the article's Creative Commons licence, unless indicated otherwise in a credit line to the material. If material is not included in the article's Creative Commons licence and your intended use is not permitted by statutory regulation or exceeds the permitted use, you will need to obtain permission directly from the copyright holder. To view a copy of this licence, visit <http://creativecommons.org/licenses/by-nc-nd/4.0/>.

© The Author(s) 2026

¹Laboratory of AI and Biomedical Science (LABS), Columbia University, New York, NY, USA. ²GE Healthcare, Bellevue, WA, USA. ³Systems Lab, Department of Psychiatry, Melbourne Medical School, The University of Melbourne, Melbourne, Victoria, Australia. ⁴Laboratory of Behavioral Neuroscience, National Institute on Aging, National Institutes of Health, Baltimore, MD, USA. ⁵Artificial Intelligence in Biomedical Imaging Laboratory (AIBIL), Center for AI and Data Science for Integrated Diagnostics (AI2D), Perelman School of Medicine, University of Pennsylvania, Philadelphia, PA, USA. ⁶Department of Brain Sciences and Department of Computing, Imperial College London, London, UK. ⁷NIHR Biomedical Research Centre at Moorfields Eye Hospital NHS Foundation Trust and Institute of Ophthalmology, University College London, London, UK. ⁸Department of Radiology, Columbia University, New York, NY, USA. ⁹Department of Biomedical Engineering, Columbia University, New York, NY, USA. ¹⁰New York Genome Center (NYGC), New York, NY, USA. ¹⁴These authors contributed equally: Aleix Boquet-Pujadas, Filippos Anagnostakis. *A list of authors and their affiliations appears at the end of the paper.

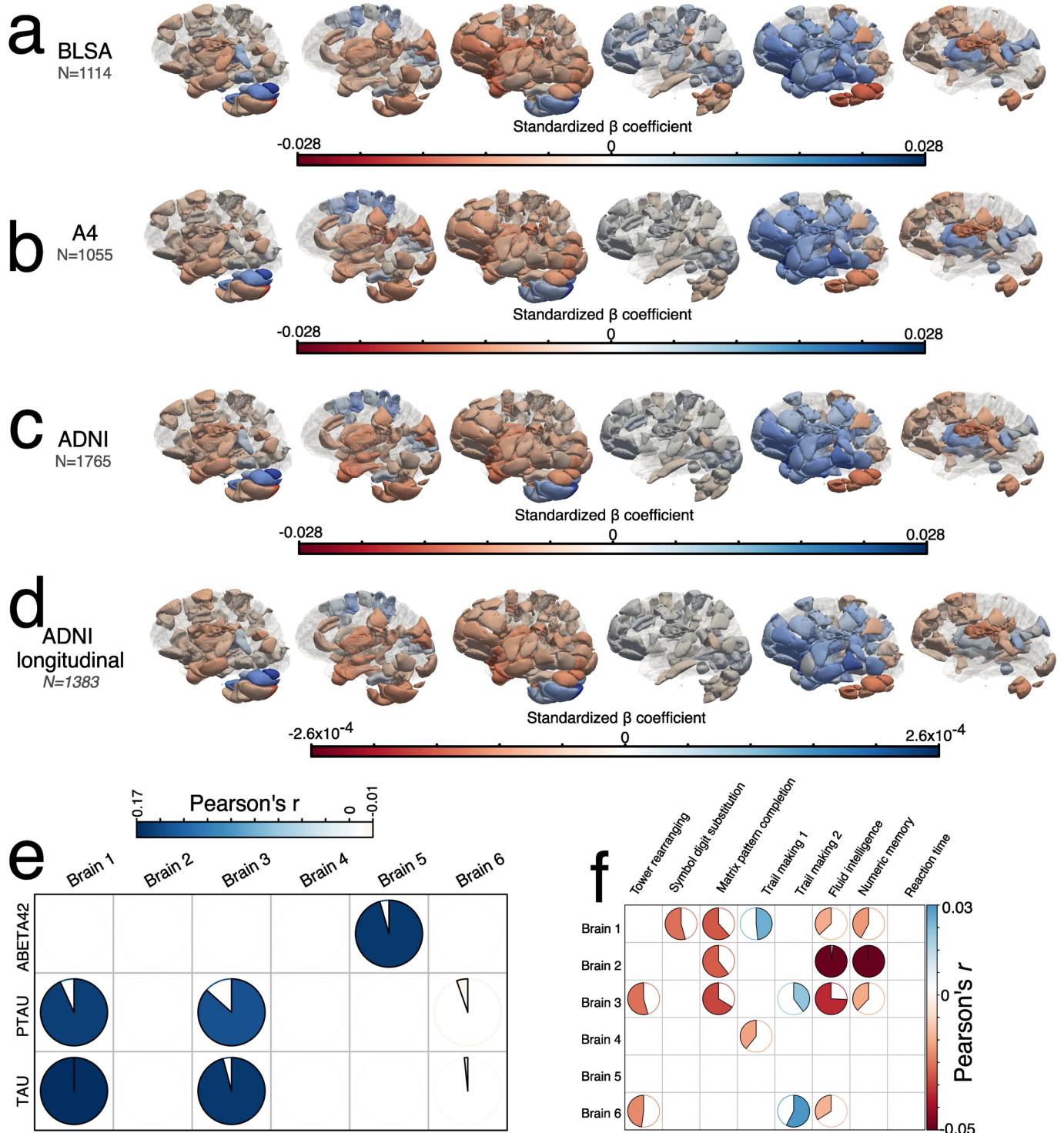
✉ e-mail: junhao.wen89@gmail.com

The MULTI Consortium

Junhao Wen^{1,8,9,10}, Christos Davatzikos⁵, Ye Ella Tian³, Wenjia Bai⁶, Michael S. Rafii¹¹, Paul Aisen¹¹, Keenan A. Walker⁴, Andrew Zalesky³, Luigi Ferrucci¹² & Jian Zeng¹³

¹Alzheimer's Therapeutic Research Institute, Keck School of Medicine of the University of Southern California, San Diego, CA, USA.

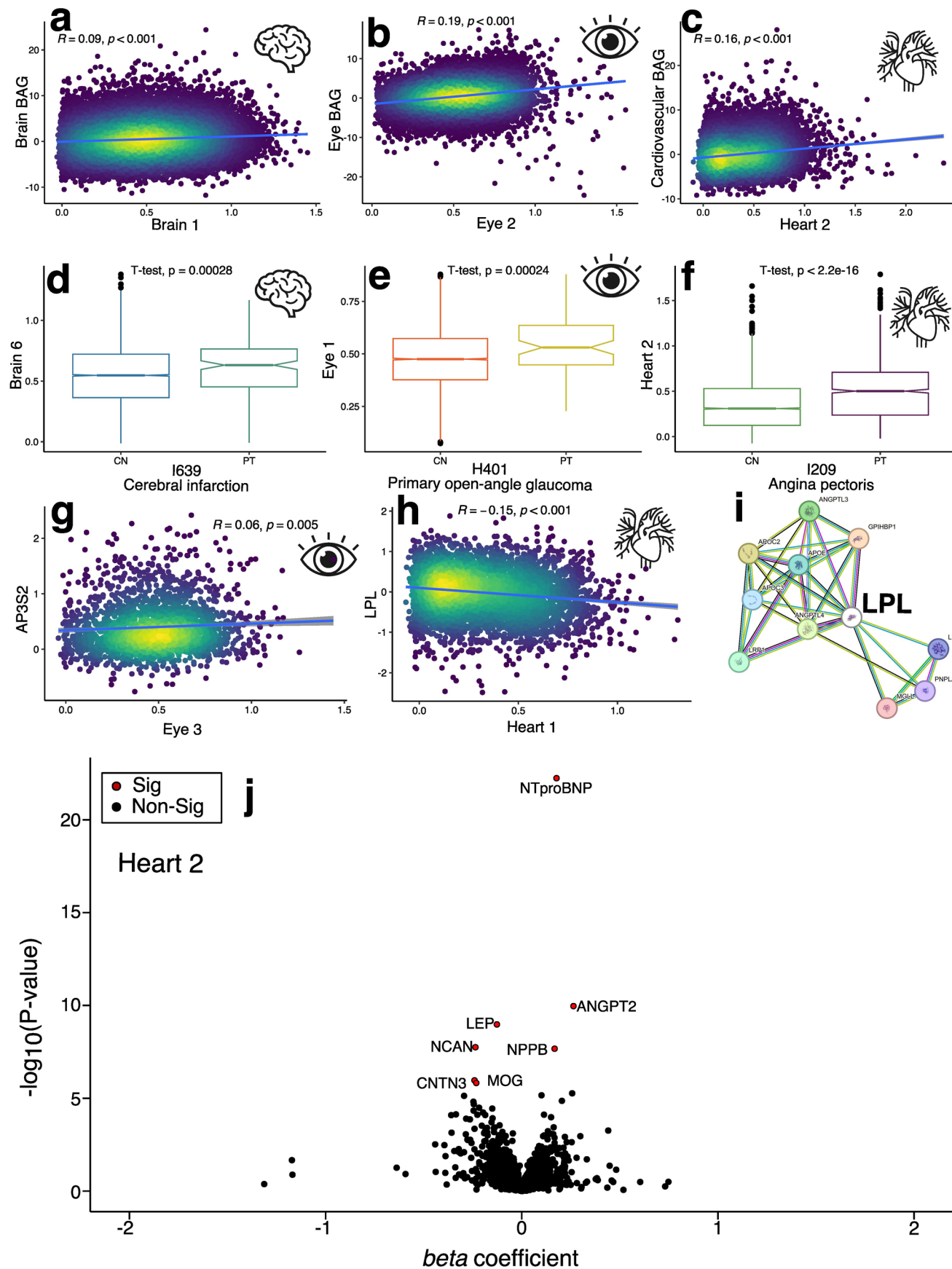
¹²National Institute on Aging, National Institutes of Health, Baltimore, MD, USA. ¹³The Institute for Molecular Bioscience, University of Queensland, Brisbane, Queensland, Australia.



Extended Data Fig. 1 | See next page for caption.

Extended Data Fig. 1 | Manifestation of the 6 brain MAEs in independent, harmonized datasets covering the AD continuum and their longitudinal follow-ups. **a**) The imaging patterns of the 6 brain MAEs manifest in an aging cohort (BLSA) using the baseline scans. The same brain regions that passed the Bonferroni correction in the training data are presented with the same effect size magnitude ($-0.028 < \text{standardized } \beta \text{ coefficient} < 0.028$). **b**) The imaging patterns of the 6 brain MAEs manifest in a preclinical AD cohort (A4) using the baseline scans. The same brain regions that passed the Bonferroni correction in the training data are presented with the same effect size magnitude ($-0.028 < \text{standardized } \beta \text{ coefficient} < 0.028$). **c**) The imaging patterns of the 6 brain MAEs manifest in an AD clinical cohort (ADNI) using the baseline scans. The same brain regions that passed the Bonferroni correction in the training data are presented with the same effect size magnitude ($-0.028 < \text{standardized } \beta \text{ coefficient} < 0.028$). **d**) The imaging patterns of the 6 brain MAEs manifest longitudinally in the ADNI data ($N = 1383$ at baseline

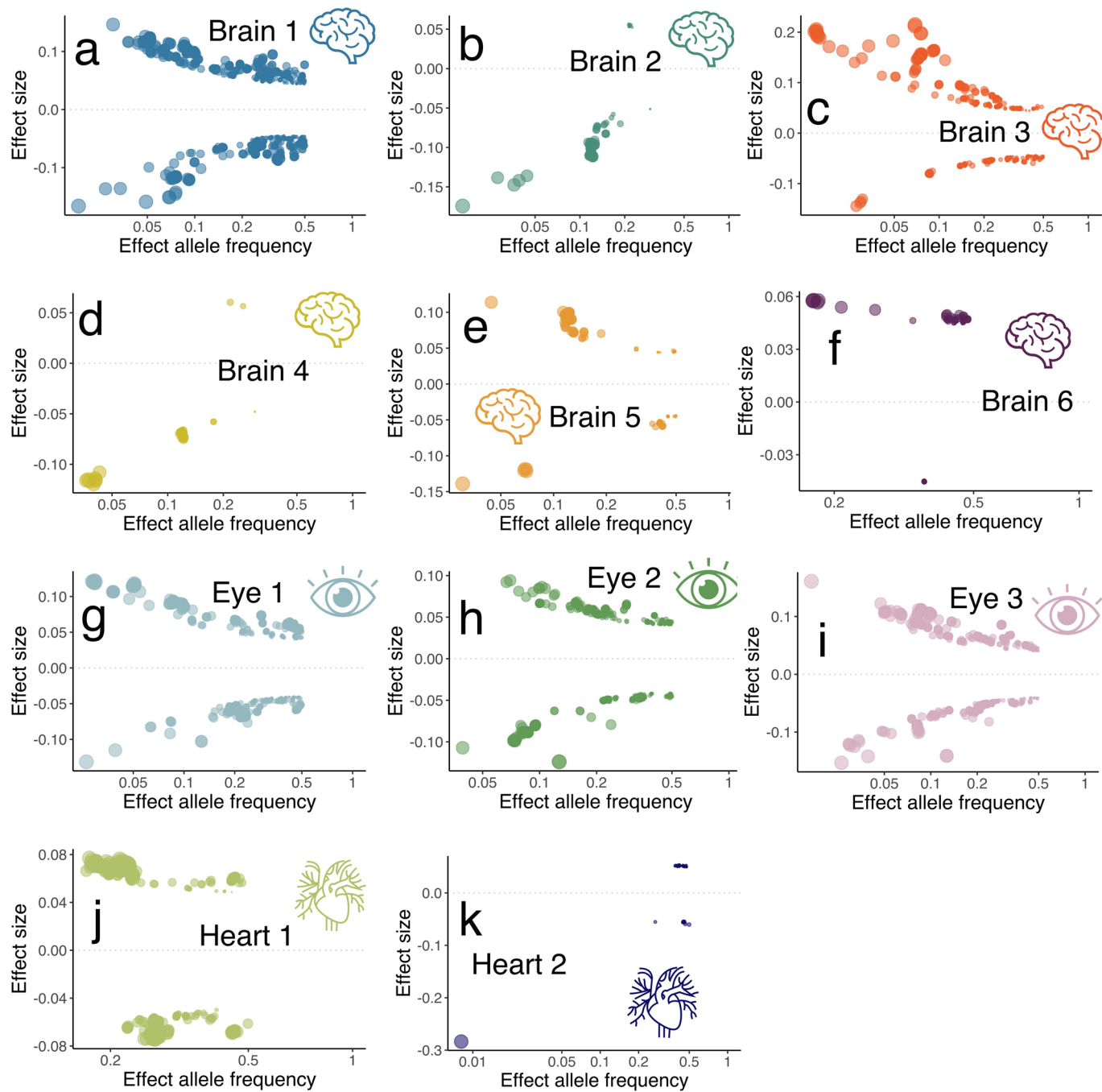
for at least 5 follow-up MRI scans). **e**) The ADNI data show the associations between the 6 brain MAEs and CSF levels of $\text{A}\beta_{1-42}$, tau_{ISIP} , and $\text{p-tau}_{\text{ISIP}}$. Statistical significance was assessed using a linear regression model that adjusted for covariates, with the Bonferroni correction applied to the two-sided P-value. Pearson's r was reported for the significant associations. **f**) The associations between the 6 brain MAEs and 8 cognitive scores in the UKBB data. Statistical significance was assessed using a linear regression model that adjusted for covariates, with the Bonferroni correction applied to the two-sided P-value. Pearson's r was reported for the significant associations. The scatter plot shows a linear regression line for visualization despite a weak linear effect. Supplementary File 4 and Supplementary Table 2–3 present the detailed results. Of note, although we applied statistical harmonization to brain MAE data from different studies and ensured the patterns were shown in these studies, potential uncontrolled domain shifts may still affect the generalizability of the model.



Extended Data Fig. 2 | See next page for caption.

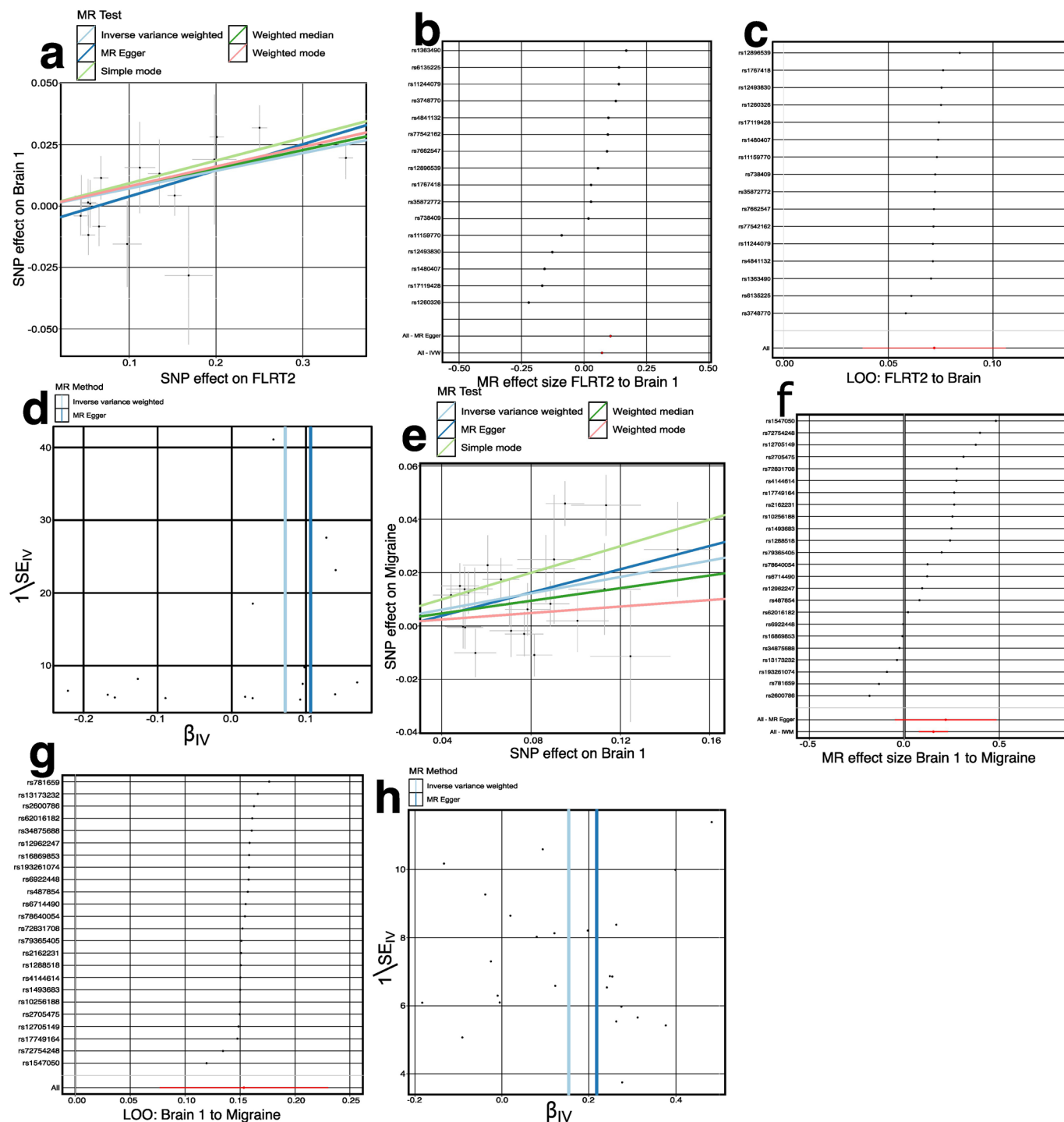
Extended Data Fig. 2 | Representative association results for our PWAS and ProWAS across the brain, eye, and heart pan-disease. **a**) The scatter plot between Brain 1 and brain BAG. **b**) The scatter plot between Eye 2 and eye BAG. **c**) The scatter plot between Heart 2 and cardiovascular BAG. The brightness of the dots reflects their density, and the plot includes Pearson's correlation coefficient (R) and the corresponding P-value, with a fitted linear regression line overlaid. Full sets of covariate-corrected statistics from a linear regression model are reported in the Supplementary Material. **d**) The box plot for Brain 6 between healthy controls (CN) and patients (PT) of cerebral infarction (ICD-10 code: I639). **e**) The box plot for Eye 1 between healthy controls (CN) and patients (PT)

of primary open-angle glaucoma (ICD-10 code: H401). **f**) The box plot for Heart 2 between healthy controls (CN) and patients (PT) of angina pectoris (ICD-10 code: I209). The mean value of the MAE and the P-value of the two-sample t-test are shown, along with outlier data points. **g**) The scatter plot between Eye 3 and the AP3S2 protein. **h**) The scatter plot between Heart 1 and the LPL protein. **i**) The protein-protein-interaction (PPI) network for the LPL protein is presented using the STRING database. **j**) The volcano plots for Heart 2 in our ProWAS analyses. Significant signals are annotated by red dots and protein symbols. The exact sample sizes of all analyses are presented in Supplementary File 6. For panels **g**, **h**, **j**, and **d-f**, P-values are two-sided.



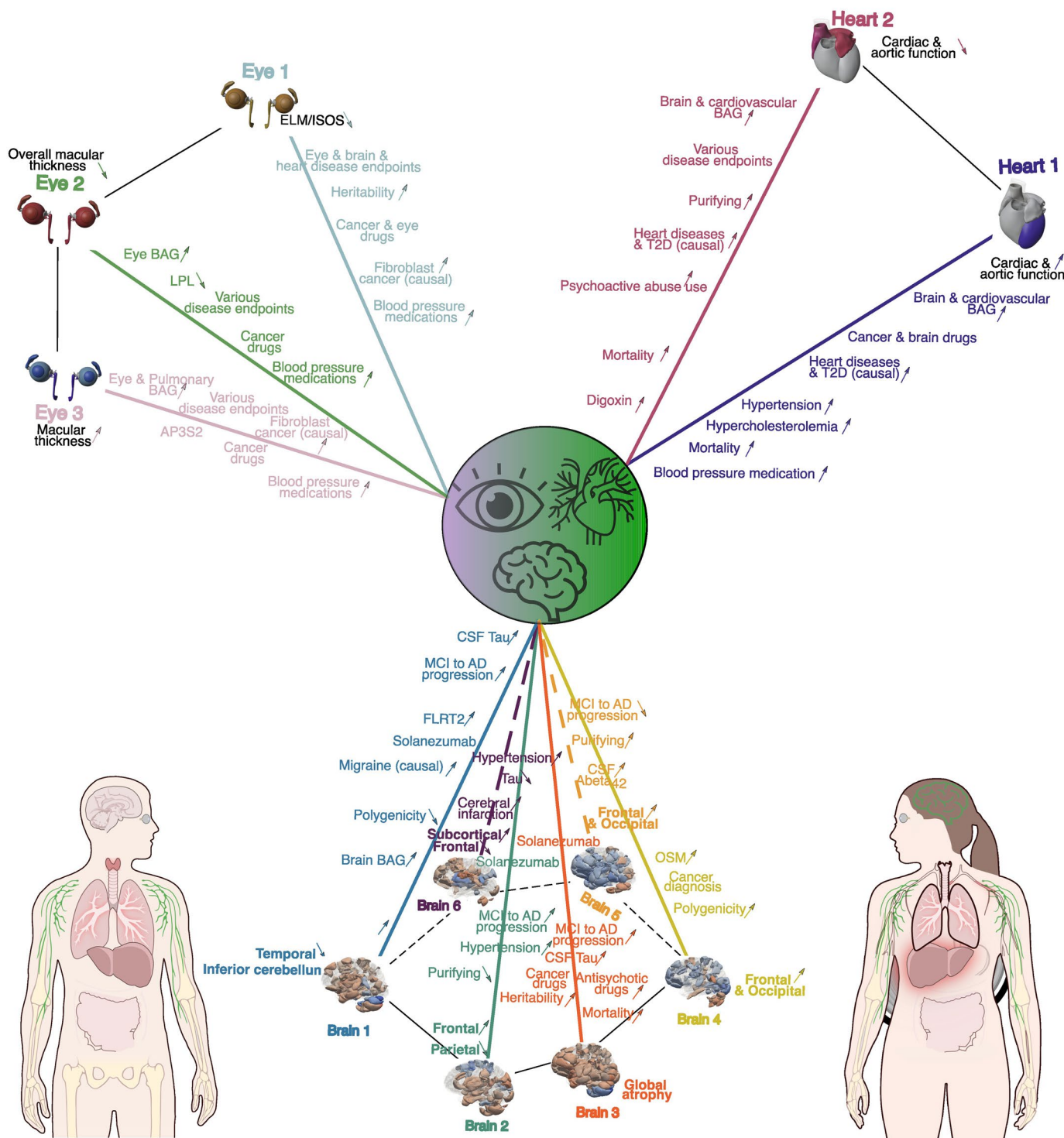
Extended Data Fig. 3 | Trumpet plots of the effect (alternative) allele frequency vs. the β coefficient of the 11 MAE GWASs (a-f for the brain; g-i for the eye, and j-k for the heart). The trumpet plots display the inverse relationship between the alternative (effect) allele frequency and the effect size (β coefficient) for

the 11 MAEs. For visualization purposes, we showed the SNPs that passed the genome-wide P-value threshold (LD was considered in all other analyses; two-sided P-value < 5×10⁻⁸). The dot size corresponds to the effect size, while the transparency of the dot is proportional to its statistical significance.



Extended Data Fig. 4 | Sensitivity check analyses for the causal pathway of “FLRT2 → Brain1 → migraine”. **a**) Scatter plot for the MR effect sizes of the SNP-FLRT2 association (x -axis, log OR) and the SNP-Brain1 associations (y -axis, log OR) with standard error bars. **b**) Forest plot for the single-SNP MR results. Each dot represents the MR effect (log (OR)), and the error bar displays the 95% CI for FLRT2 on Brain1 using only one SNP; the red line shows the MR effect using all SNPs together for IVW and MR Egger estimators. **c**) Leave-one-SNP-out analysis of FLRT2 on Brain1. Each dot represents the MR effect (log OR), and the error bar displays the 95% CI by excluding that SNP from the analysis. **d**) Funnel plot for the relationship between the causal effect of FLRT2 on Brain1. Each dot represents

the MR effect sizes estimated using each SNP as a separate instrument against the inverse of the standard error of the causal estimate. **e**) Scatter plot for the MR effect sizes of the SNP-Brain1 association (x -axis, log OR) and the SNP-migraine associations (y -axis, SD units) with standard error bars. **f**) Forest plot for the single-SNP MR results. **g**) Leave-one-SNP-out analysis of Brain1 on migraine. **h**) Funnel plot for the relationship between the causal effect of Brain1 on migraine. For panels **a** and **e**, each point shows an SNP's beta for the outcome and exposure, with error bars indicating the corresponding standard errors. For panels **b**, **c**, **f**, and **g**, each point denotes the estimated effect size, and the error bars show its standard error.



Extended Data Fig. 5 | A dimensional representation of the 11 Multi-organ AI Endophenotypes (MAEs) for pan-disease of the brain, eye, and heart.
We summarized the key characteristics of the 11 MAEs to understand the heterogeneity and commonalities across pan-disease manifestations in the brain, eye, and heart. Each MAE is represented by a distinct color, while the

black-italicized text describes the imaging patterns specific to each MAE. Directional arrows indicate trends in characteristics such as atrophy/enlarged volume or thinning/thickening. If no directional trend was observed (for example, in gene-drug-disease networks), arrows were omitted from the illustration.

Reporting Summary

Nature Portfolio wishes to improve the reproducibility of the work that we publish. This form provides structure for consistency and transparency in reporting. For further information on Nature Portfolio policies, see our [Editorial Policies](#) and the [Editorial Policy Checklist](#).

Statistics

For all statistical analyses, confirm that the following items are present in the figure legend, table legend, main text, or Methods section.

n/a Confirmed

- The exact sample size (n) for each experimental group/condition, given as a discrete number and unit of measurement
- A statement on whether measurements were taken from distinct samples or whether the same sample was measured repeatedly
- The statistical test(s) used AND whether they are one- or two-sided
Only common tests should be described solely by name; describe more complex techniques in the Methods section.
- A description of all covariates tested
- A description of any assumptions or corrections, such as tests of normality and adjustment for multiple comparisons
- A full description of the statistical parameters including central tendency (e.g. means) or other basic estimates (e.g. regression coefficient) AND variation (e.g. standard deviation) or associated estimates of uncertainty (e.g. confidence intervals)
- For null hypothesis testing, the test statistic (e.g. F , t , r) with confidence intervals, effect sizes, degrees of freedom and P value noted
Give P values as exact values whenever suitable.
- For Bayesian analysis, information on the choice of priors and Markov chain Monte Carlo settings
- For hierarchical and complex designs, identification of the appropriate level for tests and full reporting of outcomes
- Estimates of effect sizes (e.g. Cohen's d , Pearson's r), indicating how they were calculated

Our web collection on [statistics for biologists](#) contains articles on many of the points above.

Software and code

Policy information about [availability of computer code](#)

| | |
|-----------------|--|
| Data collection | No software was used for data collection |
| Data analysis | <p>The software and resources used in this study are all publicly available:</p> <ul style="list-style-type: none"> • Surreal-GAN (v0.1.1): https://github.com/zhijian-yang/SurrealGAN, Disease heterogeneity analysis; • MUSE (v3.1.0): https://github.com/CBICA/MUSE, RAVENS map extraction; • SOPNMF (v0.0.4): https://github.com/anbai106/SOPNMF, Brain PSC extraction; • ukbb_cardiac (git commit 2b6d637): https://github.com/baiwenjia/ukbb_cardiac, Heart IDP extraction; • FUMA (v1.5.0): https://fuma.ctglab.nl/, Gene mapping, genomic locus annotation; • GCTA (v1.94.1): https://yanglab.westlake.edu.cn/software/gcta/#Overview, Heritability estimates & fastGWA; • LDSC (git commit aa33296): https://github.com/bulik/ldsc, genetic correlation • TwoSampleMR (v0.5.6): https://mrcieu.github.io/TwoSampleMR/index.html, Mendelian randomization; • PRS-CS (release date: Aug 10, 2023): https://github.com/getian107/PRScs, PRS calculation; • SBayesS (v.2.0.5 beta): https://cnsgenomics.com/software/gctb/#Overview, the three key parameter estimates; • Lifelines (v0.27.): https://lifelines.readthedocs.io/en/latest/, Survival analysis; • Statsmodels (0.13.2): https://www.statsmodels.org/stable/index.html, Medication prediction, BWAS, PWAS, and ProWAS; • OmicVerse (v1.6.7): https://omicverse.readthedocs.io/en/latest/; Protein-protein interaction. |

For manuscripts utilizing custom algorithms or software that are central to the research but not yet described in published literature, software must be made available to editors and reviewers. We strongly encourage code deposition in a community repository (e.g. GitHub). See the Nature Portfolio [guidelines for submitting code & software](#) for further information.

Data

Policy information about [availability of data](#)

All manuscripts must include a [data availability statement](#). This statement should provide the following information, where applicable:

- Accession codes, unique identifiers, or web links for publicly available datasets
- A description of any restrictions on data availability
- For clinical datasets or third party data, please ensure that the statement adheres to our [policy](#)

The GWAS summary statistics and pre-trained AI models from this study are publicly accessible via the MEDICINE Knowledge Portal (<https://labs-laboratory.com/medicine/>) and Synapse (<https://www.synapse.org/Synapse:syn64923248/wiki/630992154>). Our study used data generated by the TCGA Research Network (<https://www.cancer.gov/tcga>), the Human Protein Atlas (HPA: <https://www.proteinatlas.org>), and the STRING data (<https://string-db.org/>). The two platforms curated and consolidated publicly available (single-cell) RNA-seq and protein data, including the GTEx project (<https://gtexportal.org/home/>). Genomic loci annotation used data from FUMA (<https://fuma.ctglab.nl/>). PheWAS used data from the GWAS Atlas platform (<https://atlas.ctglab.nl/PheWAS>). GWAS summary data for the DEs were downloaded from the official websites of FinnGen (R9: https://www.finngen.fi/en/access_results) and PGC (<https://pgc.unc.edu/for-researchers/download-results/>). Individual data from UKBB can be requested with proper registration at <https://www.ukbiobank.ac.uk/>. Data from ADNI can be requested with proper registration at <https://adni.loni.usc.edu/>. The gene-drug-disease network used data from the DrugBank database (v.5.1.9; <https://go.drugbank.com/>). The analysis for partitioned heritability estimates used data from ROADMAP (https://egg2.wustl.edu/roadmap/web_portal/) and ENTEEx (<https://www.encodeproject.org/>). Due to privacy considerations, allele frequency information is available from Dr. Wen (junhao.wen89@gmail.com) upon request for research purposes only, with responses typically provided within one week. All main figures, Extended Data Figures, and the Supplementary Files are available on Zenodo: <https://zenodo.org/records/17156245155>.

Research involving human participants, their data, or biological material

Policy information about studies with [human participants or human data](#). See also policy information about [sex, gender \(identity/presentation\), and sexual orientation](#) and [race, ethnicity and racism](#).

Reporting on sex and gender

We included sex as a covariate in all statistical models, and provided sex-specific analyses

Reporting on race, ethnicity, or other socially relevant groupings

Whenever appropriate, we report ethnic groups. All GWAS were conducted in people of European ancestry.

Population characteristics

Study population is detailed in Method 1 and Supplementary Table 1

Recruitment

All individual-level data were initially recruited by respective studies, underwent ethnic scrutinization. In addition, we performed standard quality check for all imaging, genetics, and proteomics to ensure the data quality.

Ethics oversight

Respective study committee oversees the ethics considerations of each study. The MULTI consortium is approved by the Institutional Review Board at Columbia University (AAAV6751).

Note that full information on the approval of the study protocol must also be provided in the manuscript.

Field-specific reporting

Please select the one below that is the best fit for your research. If you are not sure, read the appropriate sections before making your selection.

Life sciences Behavioural & social sciences Ecological, evolutionary & environmental sciences

For a reference copy of the document with all sections, see nature.com/documents/nr-reporting-summary-flat.pdf

Life sciences study design

All studies must disclose on these points even when the disclosure is negative.

Sample size

No statistical methods were used to determine the final sample size used. All data from all participants were subjected to a quality check procedure to exclude unqualified data. For example, we have an automated imaging quality check pipeline to rule out low quality imaging scans; we also detailed the quality check for genetic data to rule out low quality participants.

Data exclusions

All imaging and genetic were quality-checked to exclude data that did not qualify for this study.

Replication

We used external data, A4, ADNI, and BLSA, to generalize the 6 brain MAEs.

Randomization

No randomization was performed to allocate participants into different groups. We included a wide range of covariates that have been commonly used in previous large-scale GWASs.

Blinding

Blinding was not applicable to this study because it involved secondary analyses of pre-existing, de-identified population datasets (e.g., UK Biobank), where group allocation was not manipulated by the investigators.

Reporting for specific materials, systems and methods

We require information from authors about some types of materials, experimental systems and methods used in many studies. Here, indicate whether each material, system or method listed is relevant to your study. If you are not sure if a list item applies to your research, read the appropriate section before selecting a response.

Materials & experimental systems

| | |
|-------------------------------------|-------------------------------|
| n/a | Involved in the study |
| <input checked="" type="checkbox"/> | Antibodies |
| <input checked="" type="checkbox"/> | Eukaryotic cell lines |
| <input checked="" type="checkbox"/> | Palaeontology and archaeology |
| <input checked="" type="checkbox"/> | Animals and other organisms |
| <input checked="" type="checkbox"/> | Clinical data |
| <input checked="" type="checkbox"/> | Dual use research of concern |
| <input checked="" type="checkbox"/> | Plants |

Methods

| | |
|-------------------------------------|------------------------|
| n/a | Involved in the study |
| <input checked="" type="checkbox"/> | ChIP-seq |
| <input checked="" type="checkbox"/> | Flow cytometry |
| <input type="checkbox"/> | MRI-based neuroimaging |

Magnetic resonance imaging

Experimental design

Design type

NA

Design specifications

NA

Behavioral performance measures

NA

Acquisition

Imaging type(s)

Structural MRI (T1-weighted MRI)

Field strength

3.5T

Sequence & imaging parameters

This can be found at the UK Biobank website for detail. Same details can be found for BLSA, ADNI, and A4.

Area of acquisition

Brain

Diffusion MRI

Used

Not used

Preprocessing

Preprocessing software

All software used in this study is detailed in the Code Availability section.

Normalization

For brain MRI, we used a population-level template for the brain MRI for registration purposes.

Normalization template

For brain MRI, we used a population-level template for the brain MRI for registration purposes.

Noise and artifact removal

All data underwent standard quality check pipelines, such as for brain MRI for remove noise and artifact signals.

Volume censoring

NA

Statistical modeling & inference

Model type and settings

Multivariate analyses (machine learning and deep learning) for deriving the MAEs and univariate for GWAS (linear regression, and mixed effect model)

Effect(s) tested

Beta coefficient are reported for GWAS, Odds ratio is reported for Mendelian randomization.

Specify type of analysis:

Whole brain ROI-based Both

Anatomical location(s): Using the MUSE atlas ROIs.

Statistic type for inference

Specify voxel-wise or cluster-wise and report all relevant parameters for cluster-wise methods.

(See [Eklund et al. 2016](#))

Models & analysis

n/a Involved in the study

Functional and/or effective connectivity

Graph analysis

Multivariate modeling or predictive analysis

Multivariate modeling and predictive analysis

Neural network for GAN-based Surreal-GAN method.